

SECURITY INFORMATION

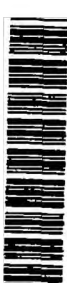
Copy
RM L52J23

232

NACA RM L52J23

TECH LIBRARY KAFB, NM

024442



NACA

RESEARCH MEMORANDUM

9176

AN INVESTIGATION OF THREE NACA 1-SERIES NOSE INLETS
AT SUBSONIC AND TRANSONIC SPEEDS

By Robert E. Pendley, Joseph R. Milillo,
and Frank F. Fleming

Langley Aeronautical Laboratory
Langley Field, Va.

**RECEIPT SIGNATURE
REQUIRED**

**NATIONAL ADVISORY COMMITTEE
FOR AERONAUTICS**

WASHINGTON
January 7, 1953

TECH LIBRARY KAFB, NM

1H

NACA RM L52J23

0144420



NATIONAL ADVISORY COMMITTEE FOR AERONAUTICS

RESEARCH MEMORANDUM

AN INVESTIGATION OF THREE NACA 1-SERIES NOSE INLETS

AT SUBSONIC AND TRANSONIC SPEEDS

By Robert E. Pendley, Joseph R. Milillo,
and Frank F. Fleming

SUMMARY

An investigation of three NACA 1-series nose inlets was conducted at subsonic and transonic speeds in the Langley 8-foot transonic tunnel. Drag, surface-pressure, and pressure-recovery measurements and schlieren photographs were obtained at zero angle of attack through a Mach number range extending from about 0.6 to 1.1, and for a mass-flow-ratio range extending from about 0.2 to the choking values. Additional pressure-recovery measurements were made at 4°, 7°, and 10° angle of attack.

The test results showed that throughout the Mach number range, large increases in additive drag which resulted from reduction of the mass-flow ratio were accompanied by only moderate increases in the external drag. The external drags of the three inlets at the choked condition were less than those of a well-shaped solid body at all Mach numbers except for the case of the two shorter inlets at the supersonic Mach numbers above about 1.05. The drag characteristics of the three inlets were not greatly different throughout the subsonic Mach number range, but an appreciable effect of inlet proportion on the drag at supersonic speeds was found. At zero angle of attack, there was little effect of diffuser geometry or Mach number on the pressure recovery when expressed as a function of the relative mass flow. High pressure recovery was measured in every case when the relative mass-flow ratio was less than about 0.95. The observed choking values of mass-flow ratio were within about 2 percent of the theoretical one-dimensional values. Adverse effects of angle of attack on the pressure recovery and on the choking values of mass-flow ratio were indicated.

INTRODUCTION

The nose air inlet continues to be of interest to the airplane designer because it can be designed to provide low drag and high

pressure recovery at subsonic and the lower supersonic speeds and because information obtained for it generally can be applied in the design of the other types of inlets.

Nose-inlet-design information for the subcritical speed range (no local sonic velocities) was obtained in the investigations reported in references 1 and 2 for NACA 1-series nose inlets with and without central bodies. Several investigations of the performance of these inlets at supercritical Mach numbers extending up to about 0.94 and at the low supersonic Mach number of 1.2 followed (refs. 3 to 5). This later work showed that large differences in the Mach number of the start of the transonic drag rise and in the magnitude of the transonic drag rise resulted with changes in the nose-inlet proportions. The more favorable drag characteristics were observed for the inlets of greater length or diameter ratio, with length ratio being the more significant variable. An investigation throughout the transonic range of the drag characteristics of nose inlets of length ratio greater than those of the inlets previously studied therefore became desirable. In addition, information concerning the transonic pressure-recovery characteristics of nose inlets operating at high angles of attack and with entry Mach numbers near unity also was needed. A research program was therefore undertaken in the Langley 8-foot transonic tunnel in order to study the transonic drag and pressure-recovery characteristics of a group of NACA 1-series nose inlets which includes several of relatively large length and diameter ratio.

After the present program had started, results became available (refs. 6 and 7) which indicated that the minimum external drag of a ducted body incorporating an NACA 1-series nose inlet of high length ratio was reduced at Mach numbers above about 1.15 by a combination of reducing the curvature of the external-inlet profile and a sharpening of the inlet lips. The drags of the modified inlet bodies, however, were higher than that of the NACA 1-series inlet bodies below this Mach number and were affected somewhat more adversely in all speed ranges by changes in flow angle at the inlet lip such as would be caused by changes in inlet mass-flow ratio or perhaps angle of attack. Thus, the NACA 1-series nose inlets still appeared to be of direct interest for transonic airplanes and for airplanes required to operate efficiently in climbing or maneuvering flight at low supersonic speeds (perhaps up to a Mach number of 1.4). The program was therefore continued essentially as originally planned except for the incorporation of some additional studies of the effects of inlet profile.

The purpose of this paper is to present the findings of the first phase of the program in which three inlets were investigated. Drag and surface-pressure measurements were made at zero angle of attack through a Mach number range extending from about 0.6 to 1.1. Pressure-recovery

CONFIDENTIAL

NACA RM L52J23

3

measurements were made at 0° , 4° , 7° , and 10° angle of attack. The mass-flow-ratio range extended from about 0.2 to the choking value.

SYMBOLS

A	stream tube or duct area
A_{sonic}	stream tube area for sonic velocity
B	base area, $\frac{\pi}{4}(2.10)^2$, sq in.
C_D	drag coefficient, $Drag/q_0 F$
C_{D_a}	additive-drag coefficient
C_{D_e}	external-drag coefficient, $C_{D_t} + C_{F_n}$
C_{D_p}	pressure-drag coefficient
C_{D_t}	total drag coefficient, $\frac{G_a}{q_0 F} + P_B \frac{B}{F}$
C_{F_n}	net thrust coefficient, $\frac{1}{q_0 F} [m(v_3 - v_0) + (p_3 - p_0)A_3]$; (internal drag when negative)
d	diameter
D	maximum body diameter
F	maximum body cross-sectional area, $\frac{\pi}{4}(D)^2$
G_a	axial force indicated by strain gage
H	total pressure
\bar{H}	average total pressure
m	internal-mass-flow rate

$$\frac{m}{m_0} \quad \text{mass-flow ratio, } \frac{m}{\rho_0 V_0 A_1} = \frac{A_0}{A_1}$$

M Mach number

p static pressure

$$P \quad \text{static-pressure coefficient, } \frac{p - p_0}{q_0}$$

$$q \quad \text{dynamic pressure, } \frac{1}{2} \rho V^2$$

r radius

r_a radius of circular arc connecting two straight sections of nose inlet diffuser

r_i radius of inlet at leading edge

v velocity

x axial distance, positive downstream

x' semiaxes of the ellipse of internal lip contour
 y'

X inlet length, distance from nose to maximum-diameter station

y_x' NACA l-series ordinate at x' station

α angle of attack

ρ air density

θ_a angle of straight section of diffuser wall measured from diffuser axis

Subscripts:

0 free-stream station

1 minimum-area station just inside inlet lip

2 pressure-recovery measuring station

3 duct-exit station

NACA RM L52J23

5

- 4 station in jet where pressure is at free-stream value
- B sting fairing base
- K stagnation point at inlet lip
- l local
- sonic conditions corresponding to local Mach number of 1

APPARATUS AND TESTS

Tunnel. - The investigation was conducted in the Langley 8-foot transonic tunnel which has a 1/9 open slotted test section. A complete description of the geometry and aerodynamic properties of this test section can be found in reference 8.

Models. - The three nose inlets utilized for this investigation were 8 inches in diameter and had NACA 1-series outer profiles. Figure 1(a) is a sketch of the nose-inlet and central-fairing configurations. The nondimensional coordinates for the outer profile appear in reference 1. The coordinates for the internal-lip shapes appear in table I, and the duct-area variations from the inlet to the maximum-diameter station are given in figure 1(b).

The internal-lip shape specified for NACA 1-series nose inlets in reference 1 consists of a circular arc, the radius of which is a function of the inlet-diameter ratio. Test data which are reported in reference 1 showed that this radius is too small and that its use resulted in large negative pressure peaks near the inlet leading edge. A revision to this circular inner-lip contour was investigated in reference 1 and other revisions aimed toward improving the internal-flow characteristics at high mass-flow ratios and angles of attack were investigated in references 2 and 9. It was concluded that further revisions would be desirable, and a new elliptical inner-lip fairing was therefore utilized for the inlets of this investigation, with the choice of proportions fixed by consideration of the results of the prior work of references 2 and 9. These proportions are given as a function of the external-inlet proportions by the following arbitrary equations:

$$x' = X \left(0.052 - 0.01128 \frac{X}{D} \right)$$

and

$$y' = y_x' \left(0.65 - 2.96 \frac{y_x'}{D} \right)$$

The terms of these equations are explained in figure 2 and in the list of symbols.

The nose inlets (fig. 3) were of spun-aluminum construction and were designed to be easily interchangeable on a common afterbody, which was also used in the tests of reference 10. Each nose inlet was provided with a row of surface pressure orifices which extended the entire length of the inlet along the center line of the upper surface. Surface pressure orifices were also installed on both the upper and lower inner lips of the inlets.

For the tests, the nose inlets were mounted on a ducted afterbody which was sting-supported in the tunnel test section. The afterbody was of spun-aluminum construction and was originally designed for a total (closed) afterbody length-to-maximum-diameter ratio of 7. The body was then cut off at a point 3 maximum diameters from the rear to provide an exit for the internal flow. A single row of external pressure orifices was placed on the upper surface and aligned with those of the inlets. The coordinates for the afterbody may be found in reference 10.

Instrumentation.— The afterbody assembly was attached to the sting through a flexure-type three-component strain-gage balance. (See fig. 4.) An aluminum fairing surrounded the strain-gage internal assembly and sting back to the exit, with care being taken that clearance was maintained between the internal assembly and the fairing at all points to the rear of the strain-gage beams. Thus, all forces on the nose inlet and afterbody, both internal and external, could be measured by the strain-gage balance.

The mass-flow rate through the system was varied by a throttle consisting of eight radial shutters, driven by a remotely controlled electric motor.

The pressure recovery was surveyed near the maximum-diameter station by rakes consisting of total- and static-pressure tubes placed at six angular locations around the annular duct. The static-pressure tubes were offset 0.3 inch from the plane of the total-pressure tubes. The internal flow was also surveyed at the exit annulus by a cruciform rake of total- and static-pressure tubes which was mounted on the sting.

NACA RM L52J23

7

The pressure leads from the nose-inlet surface pressure orifices, afterbody orifices, and pressure-recovery rakes were ducted from the outside shell of the model through hollow struts to the internal assembly and thence through the sting. The tubing and electrical leads were so tightly packed in the sting that no appreciable amount of leakage flow through the sting was expected. The afterbody is shown partly assembled in figure 5.

Tests. - Drag data were obtained at zero angle of attack through a Mach number range extending from about 0.6 to 1.11. Pressure-recovery measurements were made for the same Mach number range at zero angle of attack for all three inlets; and at the additional angles of attack of 4° , 7° , and 10° for the NACA 1-40-200 and 1-40-400 nose inlets. The procedure during tests consisted of holding the angle of attack and stream Mach number constant and recording data at various mass-flow ratios.

At zero angle of attack, drag data from the strain gage were manually recorded and all pressure readings were recorded photographically from a multitude manometer board.

No force data were recorded at angles of attack other than zero because of erratic interference between the pressure leads and the sting in the region where the pressure leads entered the sting from the pressure-tube struts. At zero angle of attack, this interference was present but calibrations of the drag beam showed that the interference was consistent and it was therefore accounted for in the final calibration.

The angle of attack of the model was set and checked during runs by means of a cathetometer. Free-stream temperature was recorded and maintained sufficiently high to avoid condensation effects in the tunnel test section. The Reynolds number variation with the Mach number of the tests is shown in reference 10, and it ranged from approximately 2.3×10^6 to 2.7×10^6 , based on the maximum diameter.

METHODS

External drag. - Since no standard terminology has been adopted by researchers in the discussion of ducted-body force components such as thrust, internal drag, and external drag, the terminology used in this paper will be explained in this section.

Fundamentally, the force of primary interest in a ducted-body jet-engine configuration is the accelerating force acting on the configuration. This force is the summation of the dragwise components of all

CONFIDENTIAL

forces acting on the configuration and is equal to the product of the mass of the configuration and its acceleration. This force might be called the net propulsive force, a quantity which is of necessarily greater interest than a thrust computed from engine-alone data, since the designer is always obliged to enclose the engine within a faired surface. Accordingly, the method of presenting the measurements of the investigation reported in this paper is based on the idea that the body drag quantities to be presented must be those to which an engine thrust known to the designer can be added to obtain the net propulsive force acting on the body-engine combination.

The axial force indicated by the strain-gage balance, when corrected for the force $(p - p_0)B$, is the summation of the dragwise viscous and gage-pressure forces acting externally and on the internal duct surfaces of the model. This force $[G_a + (p - p_0)B]$ called D_t in this paper is identical with the net propulsive force defined above. Accordingly, a definition of the ducted-body drag D_e is required such that

$$D_e - F_n = D_t \quad (1)$$

The definition of D_e is thus determined by the definition of the thrust or internal drag F_n . The usual expression for the thrust of a turbojet is

$$F_n = m(v_3 - v_0) + (p_3 - p_0)A_3 \quad (2)$$

and this quantity, with a reversal of sign, will be defined herein as internal drag. The physical meaning of this definition of the external drag can be shown as follows: Consider a ducted body of revolution at zero angle of attack (fig. 6). The net propulsive force or total drag D_t acting on the body is

$$D_t = F_e + F_i \quad (3)$$

where F_e is the summation of the dragwise components of all pressure and viscous forces acting on the external surfaces from stations K to 3, and F_i is the same summation of the forces acting on the internal surfaces. Therefore,

$$F_e + F_i = D_e - F_n$$

CONFIDENTIAL

H

NACA RM L52J23

9

and, substituting for F_n from (2) yields

$$D_e = F_e + F_i + m(V_3 - V_0) + (p_3 - p_0)A_3 \quad (4)$$

The momentum equation from stations 0 to 3 is written as follows:

$$p_0A_0 + D_a - F_i - p_3A_3 = m(V_3 - V_0) \quad (5)$$

where D_a is the force acting on the streamline OA (fig. 6). Substituting F_i from equation (5) into equation (4) gives

$$D_e = F_e + D_a + p_0(A_0 - A_3) \quad (6)$$

Let

$$f_e = \int_{r_K}^{r_3} (p - p_0)2\pi r dr + v_e$$

and

$$d_a = \int_{r_0}^{r_K} (p - p_0)2\pi r dr$$

where v_e is the resultant viscous force acting on the external surface. Viscous forces on the entering stream tube are neglected. Then, from equation (6),

$$D_e = f_e + d_a$$

The external drag as defined in this paper is therefore the summation of the gage-pressure forces acting on the entering stream tube and the gage pressure and viscous forces acting on the external surface. The former quantity d_a has been called the "additive" or "pre-entry" drag. The aerodynamic merit (in the propulsive respect) of ducted-body configurations

is directly evaluated when D_e for the configurations considered is algebraically added to the engine thrust $m(V_3 - V_0) + (p_3 - p_0)A_3$.

The external-drag data presented in this paper were calculated as follows:

$$C_{D_e} = \frac{G_a}{q_0 F} + P_B \frac{B}{F} - \frac{1}{q_0 F} \int_{exit} \left[\rho_3 V_3 (V_0 - V_3) - (p_3 - p_0) \right] dA_3$$

The integration of the exit data was performed numerically.

Additive drag. - In the absence of a static- and total-pressure survey across the inlet at station K (fig. 6), the additive drag cannot be calculated directly for an inlet with a rounded lip. Furthermore, a survey of this kind is impractical because of the variation of the stagnation-point position with mass flow. The additive drag was calculated in this investigation by measuring the static pressure at the middle of the cylindrical section (point B, fig. 6), by assuming the flow one-dimensional at station 1, and by graphically integrating the pressure distribution along the surface AB. The momentum equation written between stations 0 and 1 yields the force acting along the fluid surface OAB, and the additive drag (which acts on OA) is thus known since the force acting on AB is known.

Pressure drag. - The pressure-drag coefficient of any specified region of the body surface was obtained by graphically integrating the measured pressure distributions acting on the region considered:

$$\int P d\left(\frac{r}{R}\right)^2$$

and, in the calculation of the forebody and total pressure-drag coefficients, the additive-drag coefficient was added to the above integral.

Mass flow. - The surface pressure measured at the cylindrical section of the duct just inside the inlet lip (minimum area region) was used to calculate the mass-flow ratio at zero angle of attack. The pressures measured at the upper and lower lip were averaged, and the mass-flow ratio was calculated by assuming free-stream total pressure and one-dimensional flow at the minimum area. At the angles of attack of 4° , 7° , and 10° , one-dimensional flow at the minimum area could not be assumed, and the mass-flow ratio was obtained from numerical integration of the exit-rake data.

NACA RM L52J23

11

PRECISION OF MEASUREMENTS

Mach number.- The maximum random error in Mach number caused by inaccuracies in pressure measurements is estimated to be no greater than ± 0.003 . In calculating the Mach number at the tunnel wall, the local value of total pressure was assumed equal to the free-stream value. The error thus introduced is negligible at the lower supersonic Mach numbers and did not exceed $+0.002$ at the highest test Mach number.

Because of the length of the NACA 1-40-400 inlet, the inlet forebody projected into a region over which the tunnel-empty Mach number distribution (ref. 8) indicated an appreciable gradient at the highest test Mach numbers. From the location of the inlet lips to the location of the maximum body diameter, this tunnel-empty gradient in Mach number amounted to a Mach number change of 0.022 at $M_\infty = 1.13$ (which is slightly greater than the highest test Mach number of the present tests), and this change diminished to a negligible amount at $M_\infty = 1.05$.

The NACA 1-40-200 and 1-50-200 inlets were located in the test-section region where the tunnel-empty Mach number distribution indicated a much smaller Mach number increment (0.006) at $M_\infty = 1.13$.

External-drag coefficient.- An examination of the scatter of the data indicated that the random error in the external-drag coefficient was less than approximately ± 0.01 . Systematic errors are estimated at less than ± 0.005 .

Pressure-drag coefficient.- The errors in the pressure-drag coefficients are difficult to assess. The accuracy of these coefficients was essentially determined by the accuracy of the forebody pressure-drag coefficients, which was affected by the assumption of one-dimensional flow at the inlet (minimum-area) station, by the limited number of pressure orifices at the inlet lip, and by the uncertainties associated with fairing curves through the scattered pressure-coefficient data points. The possible error in forebody pressure-drag coefficient was greatest at the lowest mass-flow ratios, where the probable maximum error is estimated as approximately ± 0.015 . At high mass-flow ratios, the probable error is estimated at approximately ± 0.01 . The change in pressure-drag coefficient resulting from changes in Mach number are believed to be indicated more reliably than the absolute values.

Mass-flow ratio.- The computation of mass-flow ratio was least accurate at the lowest mass-flow ratio and at the lowest Mach number where the error was estimated to be ± 0.06 . At the high mass-flow ratios, the error is less than ± 0.03 .

Pressure recovery. - The maximum error in total-pressure ratio is approximately ± 0.001 . The pressure recovery was weighted according to area:

$$\frac{\bar{H}}{H_0} = \frac{1}{A_2} \int \frac{H_2}{H_0} dA$$

The total-pressure ratio as obtained by this integration was less than that obtained by

$$\frac{\bar{H}}{H_0} = \frac{1}{m} \int \frac{H_2}{H_0} dm$$

for several trial cases of the largest total-pressure gradients by 0.02. The largest gradients existed for the choking condition, and, for unchoked conditions at zero angle of attack, the difference in the two methods of integration was negligible (about 0.001).

RESULTS AND DISCUSSION

Tunnel boundary interference. - Tests of reference 10 showed that in the Langley 8-foot transonic tunnel, there was no important tunnel boundary interference at subsonic Mach numbers on a 66-inch-long body of maximum diameter equal to that of the inlets of the present investigation. A qualitative indication of the magnitude of the difference in the subsonic tunnel interference acting on the three inlets tested and the solid body of reference 10 is provided by tunnel-wall Mach number distributions. These distributions are presented in figure 7 for the three inlets for the choked condition. The distributions for other mass-flow ratios are not shown since the effect of mass-flow ratio on the distributions was negligible except at the higher supersonic Mach numbers, where, as will be discussed later, longitudinal shifts in the position of the reflected bow shock were induced by changes in the mass-flow ratio. A comparison of the distributions of figure 7 with those of reference 10 shows that the magnitudes of the model-induced disturbances at the wall are, for the inlet configurations, equal to or less than those of the solid body at Mach numbers of about 0.95 and below. At a Mach number of about 1.0, the disturbances of the shorter inlets at the tunnel wall are slightly greater than those of the solid body. It therefore seems reasonable to assume that there was no large subsonic tunnel interference acting on the inlets.

As discussed in reference 10, and as shown by the surface pressure distributions of figures 8, 9, and 10, reflected compression and expansion waves may be expected to introduce appreciable interference in the

NACA RM L52J23

13

drag measurements at supersonic speeds, and the discussion of these measurements which follows below will be supplemented with a discussion of the phenomena in that region of the model surface which is unaffected by boundary interference. This region is that forward of the model surface under the influence of the reflected bow shock. All drag data which are presented in the figures for supersonic Mach numbers are faired with dashed curves where boundary interference is possible. The presentation of interference-subject drag data in the figures is considered desirable since the interference is not expected to affect to an important degree the variation of drag coefficient with mass-flow ratio and further, the interference is not expected to preclude a qualitative indication of the effects of inlet proportions on the forebody pressure drag.

Surface pressure distribution. - The effects of mass-flow ratio on the surface pressure distribution in the region of the inlet lip are shown in figures 11, 12, and 13. Although surface irregularities which were caused by the method of model construction and manufacture resulted in considerable raggedness in the distributions, it is possible to observe the important characteristics. The curves in figures 11, 12, and 13 were faired consistently with the fairings of the plots which were integrated in the calculation of the pressure drag. Samples of these plots are shown in figure 14.

For all three inlets, the effects of mass-flow ratio on the external pressures were confined essentially to the region close to the inlet lip. Poor agreement is shown between the internal pressure coefficients at the minimum-area station and the critical pressure coefficient at inlet-choked conditions. This disagreement is primarily the result of the non-one-dimensionality of the flow at this station. Also, the pressure coefficient at the minimum area is very sensitive to changes in the mass-flow ratio near the choking value, since

$$\frac{dP_1}{d\left(\frac{m}{m_0}\right)} \rightarrow \infty \text{ as } M_1 \rightarrow 1.0$$

Pressure distributions over the inlet-afterbody combinations are shown in figures 8, 9, and 10 for the extreme test values of mass-flow ratio. Although the inlet area of the NACA 1-50-200 inlet is more than 60 percent greater than that of the NACA 1-40-200, the difference in the external curvature of the two inlets was not large enough to produce important differences in the level of the induced velocities. The pressure distribution of the NACA 1-40-400 nose inlet and afterbody indicate that low and roughly constant values of induced velocities

existed over almost all of the external surface at the higher mass-flow ratios. The irregularities in the data points which were caused by surface irregularities appear to have been amplified by an increase of the Mach number up to $M_0 \approx 1.0$. At the Mach number of approximately 1.11, the interference of the tunnel-boundary reflected bow shock can be seen in figures 8, 9, and 10 acting on the body surface in the region of x/D of about 2 to 3. There was considerable influence of the mass-flow ratio on the position of the reflected shock. As shown by the schlieren photographs in figure 15(a), the bow shock moved closer to the inlet and became more curved as the mass-flow ratio was increased. (The grid spacing shown in the photographs is 0.4 inch.) As a result, the point at which the reflected bow shock struck the model moved rearward with increasing mass-flow ratio.

The pressure distributions of the NACA 1-40-200 and 1-50-200 nose inlets indicate the formation of a region of supersonic velocities over much of the forebody when the Mach number exceeded 0.9 (figs. 8 and 9). At the lower mass-flow ratios, sharply localized regions of supersonic flow existed at the inlet lip at lower Mach numbers. At $M_0 \approx 0.95$, the extensive region of supersonic flow was probably terminated by a weak normal shock in the vicinity of the maximum-diameter station, with subsonic flow extending downstream from this point. This shock moved rearward with increasing Mach number, and was in the schlieren field of view at $M_0 \approx 1.0$ (fig. 15(b)). At this Mach number, the flow accelerated to supersonic velocities behind the shock (figs. 8(d) and 9(e)), and was once more compressed to subsonic velocities through a second normal shock near the jet (fig. 15(c)). At $M_0 \approx 1.022$, (fig. 9(f)), the first shock moved farther downstream, and, although the pressure distribution indicates the presence of the second shock, it is not visible in the schlieren photograph (fig. 15(c)). The failure of this shock to appear in the photograph may have been caused by improper adjustment of the knife edge for this photograph. The first shock had apparently moved farther downstream at a Mach number of 1.05 (figs. 8(e), 9(g), and 15(c)) and was then the only normal shock on the body. This shock then moved downstream from the jet at a Mach number of about 1.08, with supersonic flow thus acting over the entire external surface downstream from the lip stagnation region.

The pressure distributions for the NACA 1-40-400 nose inlet (fig. 10) do not indicate the presence of the first of the two normal shocks discussed before because of the very low induced velocities of this profile.

Figure 15(d) indicates that there was no significant effect of mass-flow ratio on the shock configuration near the jet.

External drag.- An almost linear increase in external-drag coefficient resulted for all three inlets as the mass-flow ratio was reduced from the choking value (figs. 16, 17, and 18). The slope of these curves

NACA RM L52J23

15

was increased with increasing Mach number. There appear to be no important differences in the effects of mass-flow ratio on the drag of each of the inlets.

The variation of the forebody and afterbody pressure-drag coefficients with mass-flow ratio is shown in figure 19 for the highest test Mach number. The forebody pressure-drag data are essentially free of tunnel interference at this Mach number, since the bow shock reflection occurred on the afterbody (see figs. 8 and 9). Both the forebody and afterbody pressure-drag coefficients were increased by reduction of the mass-flow ratio, with the increase of the forebody drag accounting for most of the increase observed in the external drag (figs. 16, 17, and 18).

As the mass-flow ratio of a nose inlet is reduced from the choking value, the additive drag increases largely because of the decrease in area of the entering stream tube. At the same time, the local angle of the flow at the inlet lip is increased, resulting in the formation of a region of low pressures on the external surface of the inlet lip. The formation of this region largely compensates for the increase in the additive drag, as is shown by the comparison of the additive drag and the external-drag increment due to the reduction of the mass-flow ratio from the choking value (figs. 20, 21, and 22). These figures show that throughout the Mach number range, large increases in the additive drag were accompanied by only moderate increases in the external drag.

The effect of Mach number on the sum of the forebody and afterbody pressure-drag coefficient and on the external-drag coefficient measured by the force balance is shown in figure 23 for the inlet-choked condition. The difference between the two curves is the skin friction contribution to the drag.

The external-drag curves of figure 23 and the drag curve for the well-shaped solid body of reference 10 are compared in figure 24. The drag coefficients of the ducted bodies were less than those of the solid body at all Mach numbers except in the case of the two shorter inlets at the supersonic Mach numbers above about 1.05. The drag of the shorter inlets would logically be expected to be lower than that of the solid body at subsonic Mach numbers because of the smaller amount of wetted surface area. The reason for the lower subsonic drag of the NACA 1-40-400 inlet is explained by the fact that the afterbody pressure drags of the inlet bodies were less than those of the solid bodies (compare fig. 26 with fig. 17 of ref. 10). The pressure distributions of figures 8, 9, and 10, when compared with those of reference 10, indicate that the absence of exiting flow from the base of the solid body resulted in lower pressures acting over the external surface near the model base.

The subsonic drag rise, as observed between Mach numbers of about 0.9 and 1.0, was similar for the solid body and the NACA 1-40-400 inlet; a slightly larger rise is indicated for the two shorter inlets. The curves for the three inlets are not greatly different throughout the subsonic Mach number range. For subsonic applications, therefore, the zero angle-of-attack data of figure 24 indicate that the choice of the inlet profile, within the range of inlet proportions investigated, need be governed only by internal ducting and structural considerations. For blunter proportions, however, local regions of supersonic flow and strong normal shocks may be induced at subsonic Mach numbers, as was shown by the tests of reference 3. Two of the inlets of these tests were of relatively blunt proportions: the NACA 1-65-050 and 1-50-100 nose inlets, and severe subsonic drag rises were indicated for these shapes. The NACA 1-40-200 nose inlet was also studied in reference 3. No subsonic drag rise was found for this inlet except for a small increase at the highest test Mach number (0.924). It was thought that this last test point indicated an incipient sharp drag rise, but figure 24 shows that this is not the case.

An appreciable effect of inlet proportion on the drag at supersonic Mach numbers is indicated in figure 24. The drag of the NACA 1-40-400 inlet at the highest test Mach number (about 1.11) was less than that of the other inlets, and the drag of the solid body was intermediate between those of the inlets. The drag data at this Mach number are subject to tunnel boundary interference, however, and it is necessary to corroborate these drag relationships by reference to the pressure drag.

A comparison of the forebody pressure-drag coefficients is presented in the upper part of figure 25. The forebody pressure drag of a body (additive drag plus the drag on the external forebody surface) is of much significance since this quantity plus the skin friction on the external surface constitutes a large part of the total external drag, and since its transonic rise contributes a large amount to the total transonic drag rise. At the inlet-choked condition for $M_0 \approx 1.11$, the tunnel-reflected bow shock affected the pressures on the NACA 1-40-200 and 1-50-200 inlets downstream of the maximum-diameter station (figs. 8 and 9), and the forebody pressure drag for this condition is therefore equivalent to the free-flight value. The reflected shock struck the NACA 1-40-400 inlet ahead of the maximum-diameter station (fig. 10), but the effect on the forebody pressure-drag coefficient was small (+0.005) because of the small change in body radius in the region affected. The flagged symbols for the NACA 1-40-400 inlet in figure 25 were corrected for the effect of the bow-shock reflection by fairing the pressure diagram as indicated by the dashed curve in figure 14.

As stated previously in the discussion of the precision of the measurements, changes in the forebody pressure-drag coefficient resulting

3H

NACA RM L52J23

17

from changes in the Mach number are believed to be indicated more reliably than the absolute drag-coefficient values. The transonic rise in the forebody pressure-drag coefficients are therefore shown in the lower part of figure 25 as measured from $M_\infty \approx 0.90$. The drag-rise relationships of the inlets and the solid body are described by this figure in a manner consistent with that of the external-drag data (fig. 24).

The Mach number effect on the forebody and afterbody pressure-drag coefficients is shown in figure 26. The forebody and afterbody pressure-drag coefficients appear to begin to rise at the same Mach number with the forebody drag increase accounting for the largest part of the drag rise. The data point from reference 4 ($\frac{m}{m_\infty} = 0.95$) indicates for the NACA 1-40-200 nose inlet, a rising trend in the forebody pressure-drag coefficient continuing up to a Mach number of at least 1.2. Since this data point and the data point of the present tests for $M_\infty = 1.105$ are free of tunnel interference, and since it is clear that the forebody pressure drag should be too high at Mach numbers near 1.07 because of the influence of the relatively strong bow-shock reflection on the forebody (see fig. 8), the interference-free forebody-drag curve might conceivably be approximated by the solid curve shown in the supersonic Mach number range. Similar approximations are sketched for the NACA 1-50-200 and 1-40-400 inlets in figure 26.

Pressure recovery. - The three inlets investigated had almost the same pressure-recovery characteristics at zero angle of attack (fig. 27). When plotted as a function of the relative mass-flow ratio (fig. 28), little effect of Mach number or diffuser geometry on the pressure recovery is shown. High pressure recovery was measured in every case when the relative mass-flow ratio was less than about 0.95. Above this value, sonic inlet Mach number was approached and attained as the inlet choked and yielded characteristically low pressure recovery. The observed choking mass-flow ratios were within about 2 percent of the theoretical one-dimensional values.

Adverse effects of angle of attack on the pressure recovery are shown in figures 29 and 30. The maximum (choking) values of mass-flow ratio, and the values of total-pressure ratio throughout most of the mass-flow range diminished with increasing angle of attack. At the higher mass-flow ratios, decrements of about 0.05 in total-pressure ratio resulted when the angle of attack was increased to 10° . The pressure recovery of the NACA 1-40-400 inlet diffuser was less sensitive to angle of attack than that of the NACA 1-40-200.

Sample total-pressure-ratio distributions are presented in figures 31 and 32 for each of the six diffuser rakes. The radial locations of the inner and outer duct surfaces are indicated at the top of the figures;

and the level of the static pressure is shown for each case. At zero angle of attack, the total pressure distribution was almost uniform around the annulus throughout the Mach number range, and at mass-flow ratios below the choking value. Uneven flow at the diffuser rakes was observed for the choking case, as is illustrated by figure 32(d).

The effect of angle of attack on the total-pressure distribution is illustrated by data for an angle of attack of 10° , which show that the flow tends to separate in the lower part of the duct. The NACA 1-40-200 inlet suffered the worst in this respect, inasmuch as the total pressure differential between the top and bottom of the duct was greater for comparable cases (figs. 31(c) and 32(e)), perhaps as a result of the greater angle of the diffuser walls of the NACA 1-40-200 inlet. Improvement of the pressure recovery of these inlets at angle of attack will probably require a thicker lip at the bottom of the inlet, or the recovery might perhaps be aided by skewing the inlet plane.

CONCLUSIONS

The following conclusions were drawn from a study of the aerodynamic characteristics of three NACA 1-series nose inlets for a Mach number range extending from about 0.6 to 1.1.

1. Throughout the test Mach number range, large increases in the additive drag which resulted from reduction of the mass-flow ratio were accompanied by only moderate and approximately linear increases in the external drag.
2. The external-drag coefficients of the three inlets at the choked condition were less than those of a well-shaped solid body at all Mach numbers except for the case of the two shorter inlets at the supersonic Mach numbers above about 1.05.
3. The external-drag characteristics of the inlets were not greatly different throughout the subsonic Mach number range.
4. An appreciable effect of inlet proportion on the drag at supersonic speeds was indicated.
5. At zero angle of attack, there was little effect of Mach number or diffuser geometry on the pressure recovery when expressed as a function of the relative mass flow. High pressure recovery (H/H_0 greater than 0.95) was measured in every case when the relative mass-flow ratio was less than about 0.95.

NACA RM L52J23

[REDACTED] 19

6. The observed choking values of mass-flow ratio were within about 2 percent of the theoretical one-dimensional values.

7. Adverse effects of angle of attack on the pressure recovery were found. The maximum (choking) values of mass-flow ratio were reduced and a loss of about 0.05 in total-pressure ratio resulted when the angle of attack was increased to 10° at the higher mass-flow ratios.

Langley Aeronautical Laboratory,
National Advisory Committee for Aeronautics,
Langley Field, Va.

[REDACTED]

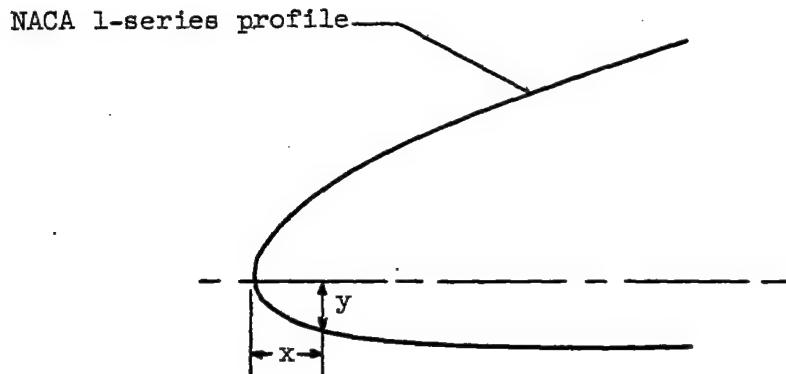
REFERENCES

1. Baals, Donald D., Smith, Norman F., and Wright, John B.: The Development and Application of High-Critical-Speed Nose Inlets. NACA Rep. 920, 1948. (Supersedes NACA ACR L5F30a.)
2. Nichols, Mark R., and Keith, Arvid L., Jr.: Investigation of a Systematic Group of NACA 1-Series Cowlings With and Without Spinners. NACA Rep. 950, 1949. (Supersedes NACA RM L8A15.)
3. Pendley, Robert E., and Smith, Norman F.: An Investigation of the Characteristics of Three NACA 1-Series Nose Inlets at Subcritical and Supercritical Mach Numbers. NACA RM L8L06, 1949.
4. Pendley, Robert E., and Robinson, Harold L.: An Investigation of Several NACA 1-Series Nose Inlets With and Without Protruding Central Bodies at High-Subsonic Mach Numbers and at a Mach Number of 1.2. NACA RM L9L23a, 1950.
5. Pendley, Robert E., Robinson, Harold L., and Williams, Claude V.: An Investigation of Three Transonic Fuselage Air Inlets at Mach Numbers From 0.4 to 0.94 and at a Mach Number of 1.19. NACA RM L50H24, 1950.
6. Sears, Richard I., and Merlet, C. F.: Flight Determination of Drag and Pressure Recovery of a Nose Inlet of Parabolic Profile at Mach Numbers From 0.8 to 1.7. NACA RM L51E02, 1951.
7. Nichols, Mark R., and Pendley, Robert E.: Performance of Air Inlets at Transonic and Low Supersonic Speeds. NACA RM L52A07, 1952.
8. Ritchie, Virgil S., and Pearson, Albin O.: Calibration of the Slotted Test Section of the Langley 8-Foot Transonic Tunnel and Preliminary Experimental Investigation of Boundary-Reflected Disturbances. NACA RM L51K14, 1952.
9. Nichols, Mark R., and Goral, Edwin B.: A Low-Speed Investigation of a Fuselage-Side Air Inlet for Use at Transonic Flight Speeds. NACA TN 2684, 1952.
10. Pendley, Robert E., and Bryan, Carroll R.: An Investigation of Some Factors Affecting the Drag of Relatively Large Nonlifting Bodies of Revolution in a Slotted Transonic Wind Tunnel. NACA RM L52H22, 1952.

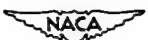
NACA RM L52J23

21

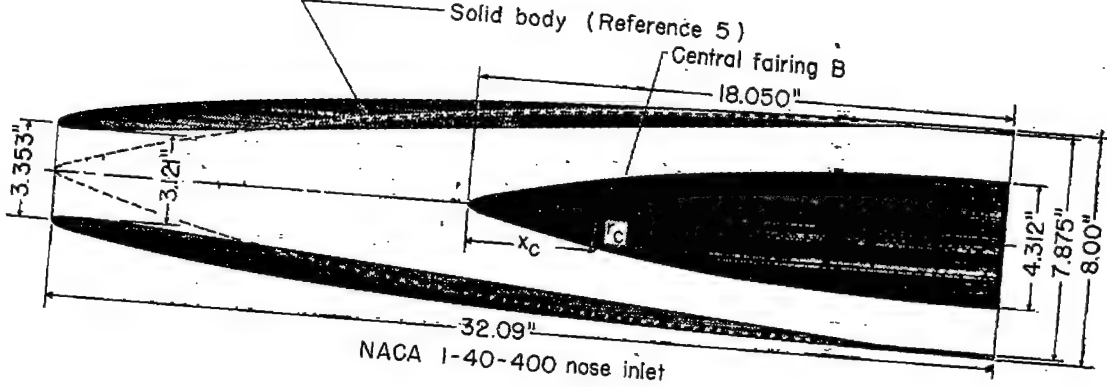
TABLE I
COORDINATES OF INLET LIP
[All coordinates in inches]



NACA 1-40-400 nose inlet		NACA 1-40-200 nose inlet		NACA 1-50-200 nose inlet	
x	y	x	y	x	y
0.000	0.000	0.000	0.000	0.000	0.000
.05	.074	.1	.129	.069	.100
.10	.098	.2	.171	.169	.145
.15	.110	.3	.195	.269	.170
.20	.116	.4	.207	.369	.182
.218	.116	.469	.209	.469	.186
1.047	.116	1.299	.209	1.493	.186
Inlet minimum area, sq in.					
7.475		6.559		10.693	



NACA RM 152J23



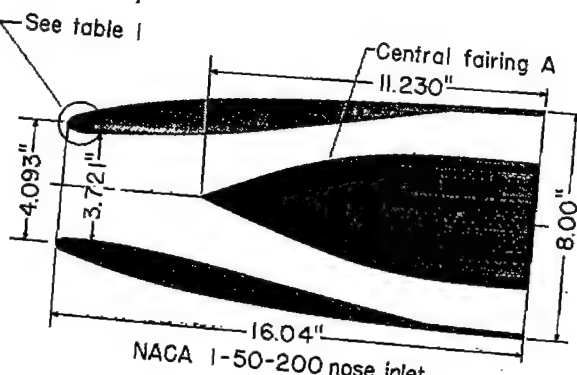
Central fairing coordinates

Central fairing A

x_c	r_c
0.00	0.00
.625	.301
1.625	.736
2.625	1.113
3.625	1.432
4.625	1.693
5.625	1.895
6.625	2.040
7.625	2.127
8.625	2.156
12.414	2.156

Central fairing B

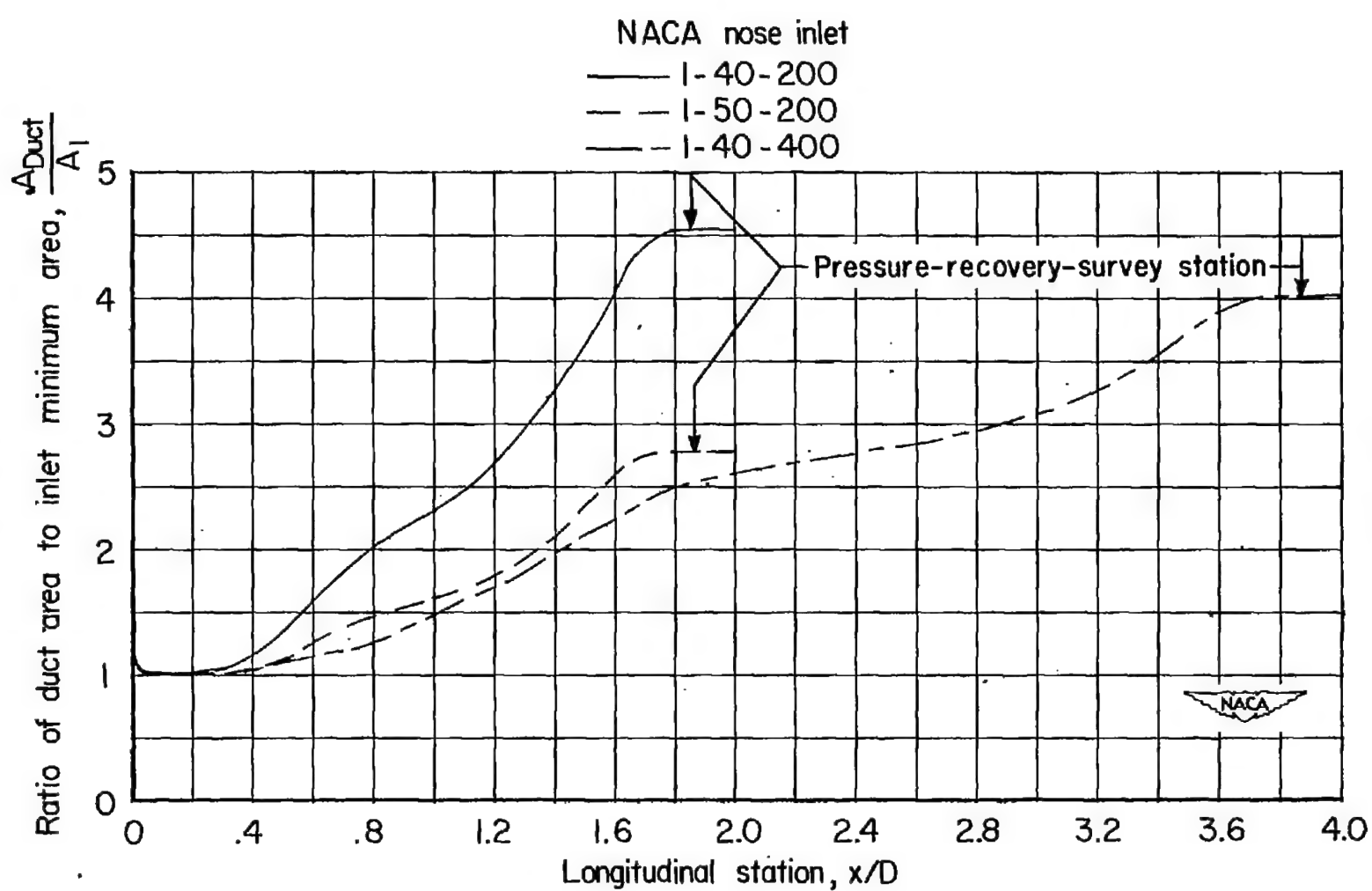
x_c	r_c
0.000	0.000
.040	.088
.065	.111
.090	.131
.190	.191
.690	.367
1.000	.450
3.000	.910
5.000	1.280
7.000	1.580
9.000	1.815
11.000	1.990
13.000	2.100
15.000	2.150
15.445	2.156
19.230	2.156



(a) Nose-inlet and central-fairing configurations.

Figure [redacted] Model dimensions.

NACA RM 15213



(b) Inlet-duct area variation.

Figure 1.- Concluded.

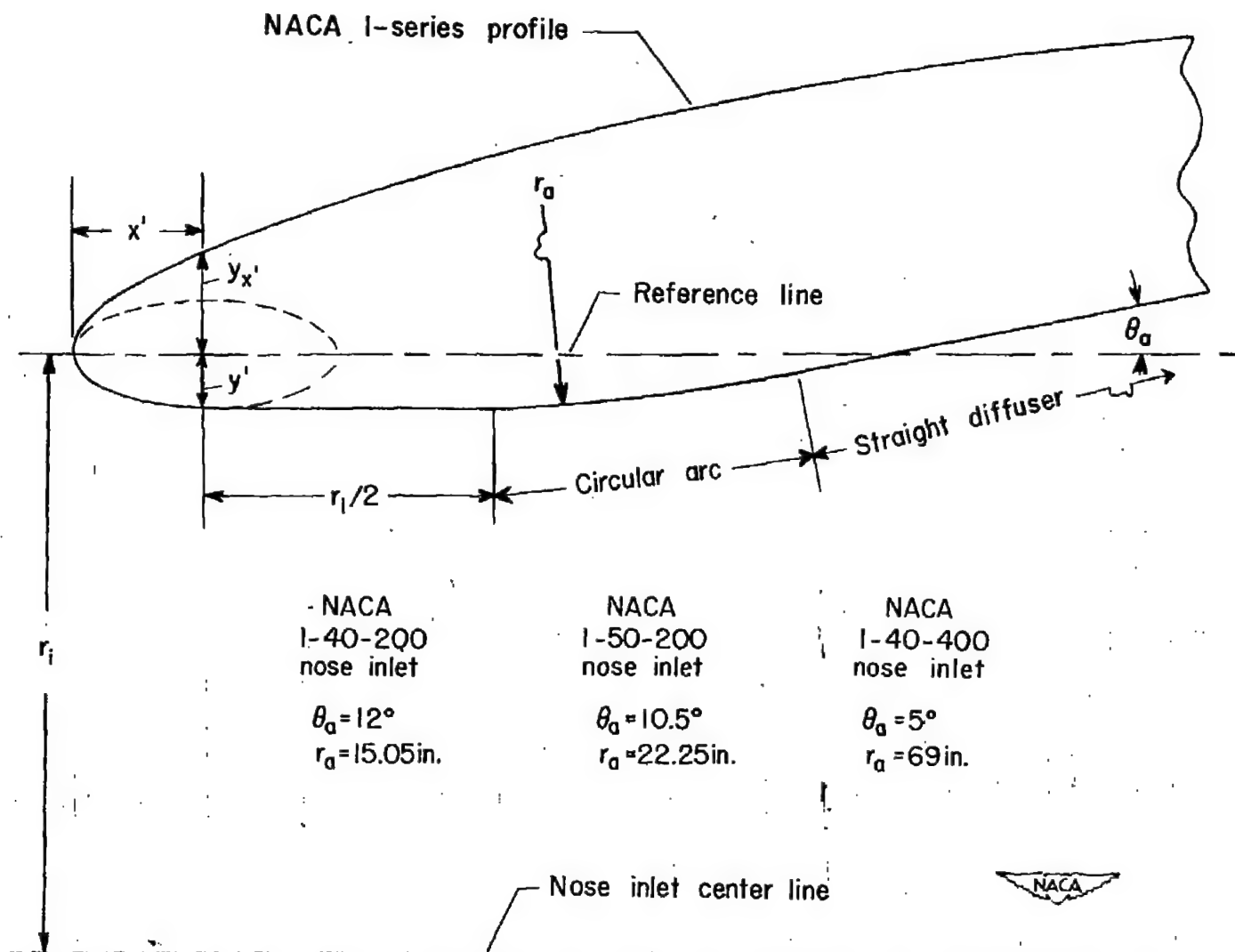


Figure 2.- Internal lip design.

4H

NACA RM 152J23

25



NACA 1-50-200
nose inlet

NACA 1-110-800
nose inlet

NACA 1-40-400
nose inlet



Figure 3.- Nose inlets investigated.

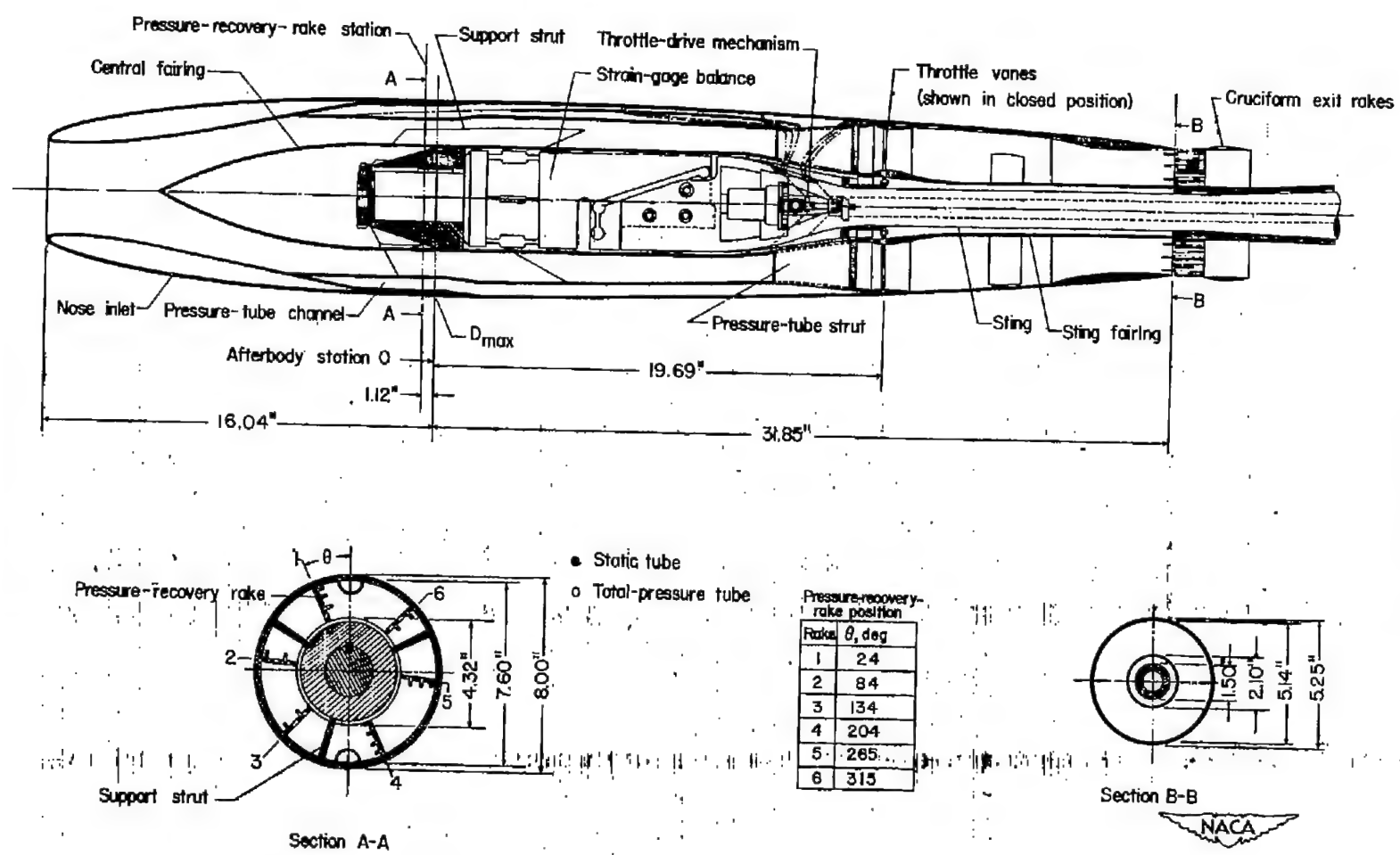
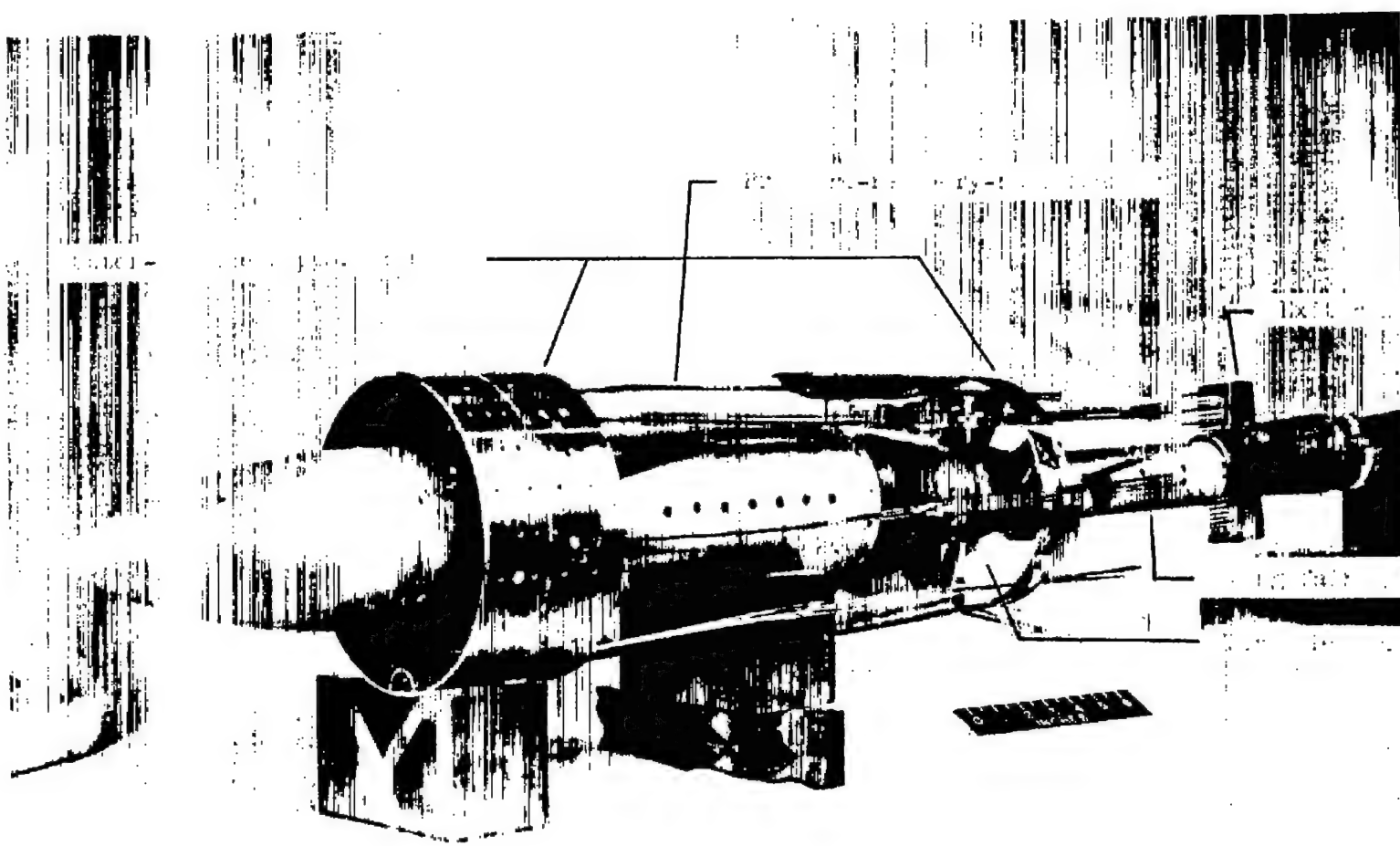


Figure 4.- Schematic drawing of nose-inlet fuselage assembly.

NACA RM 152J23



NACA

Figure 5.- Nose-inlet-fuselage model, partly assembled.

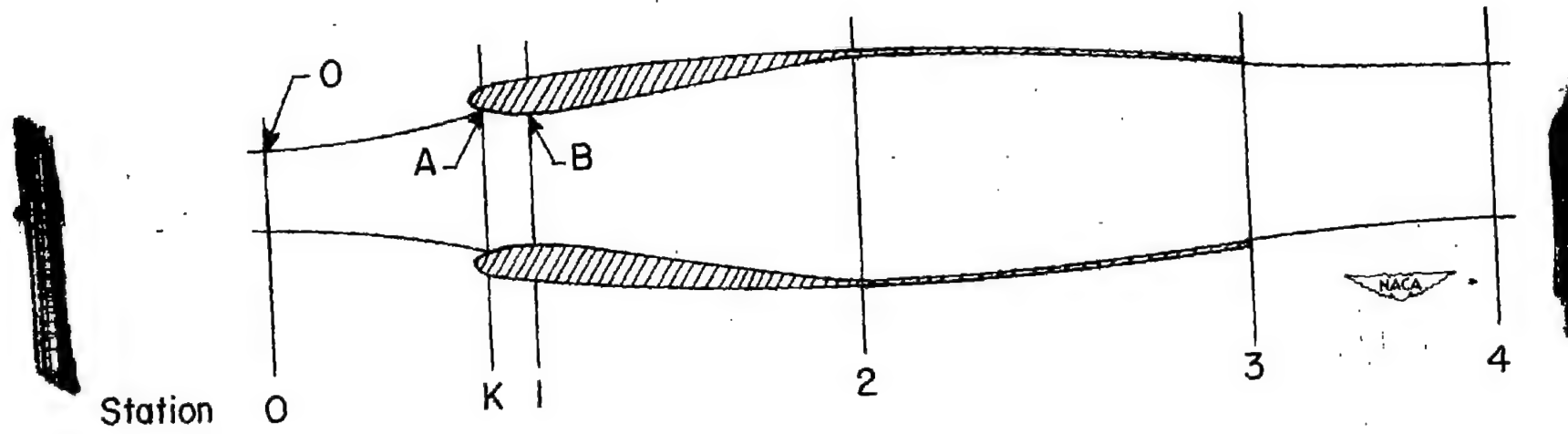
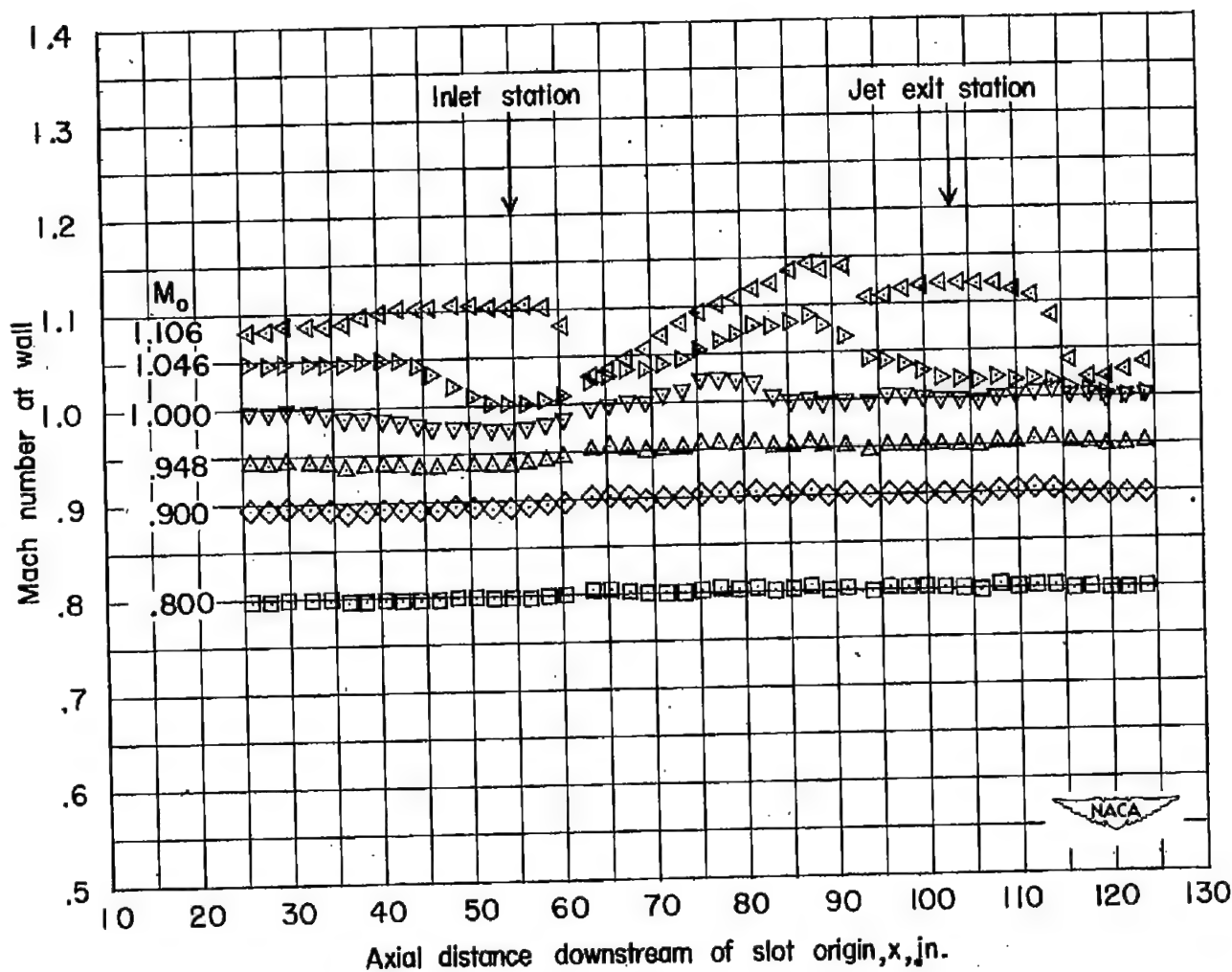


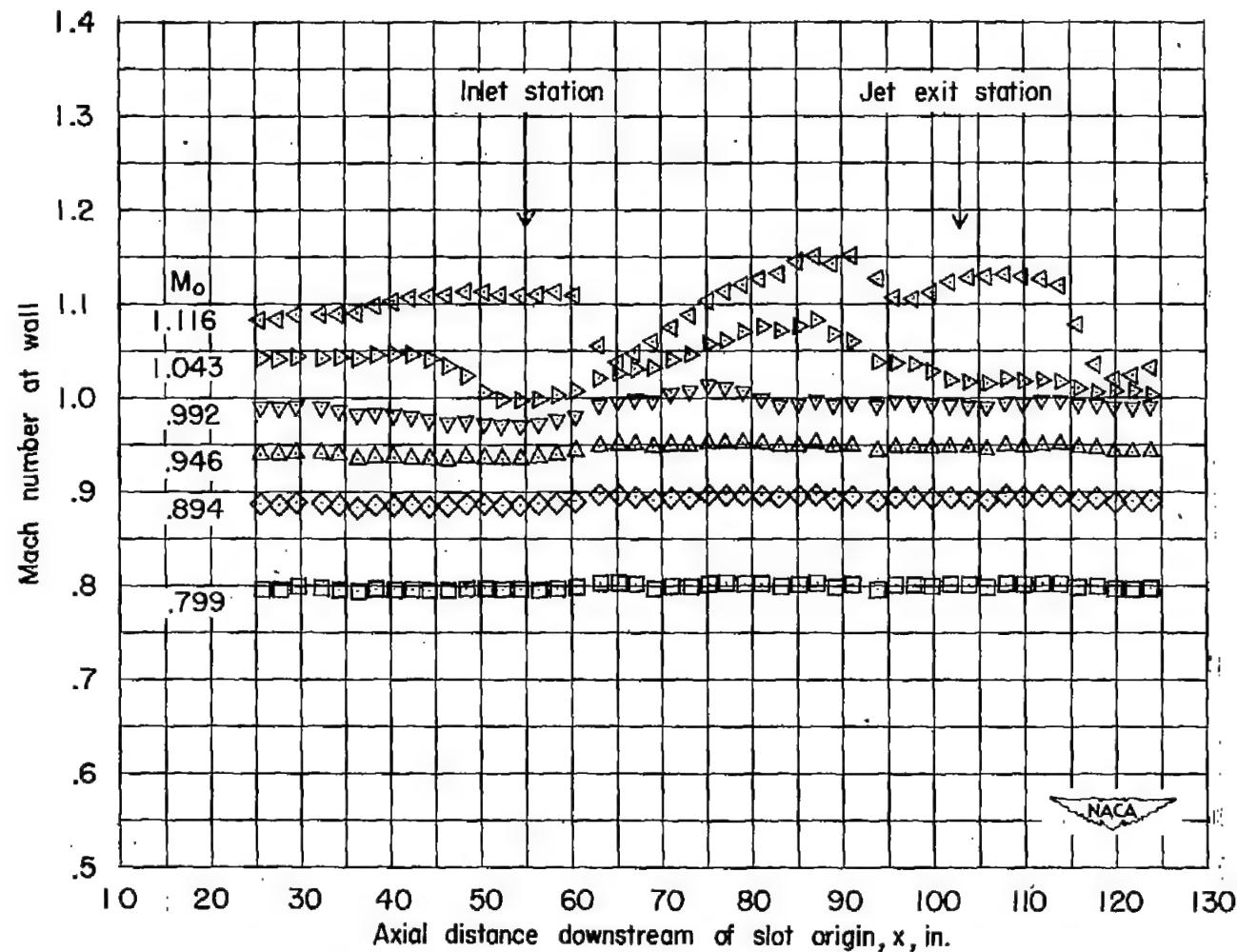
Figure 6.- Ducted-body stations.

NACA RM 152J23



(a) NACA 1-40-200 nose inlet.

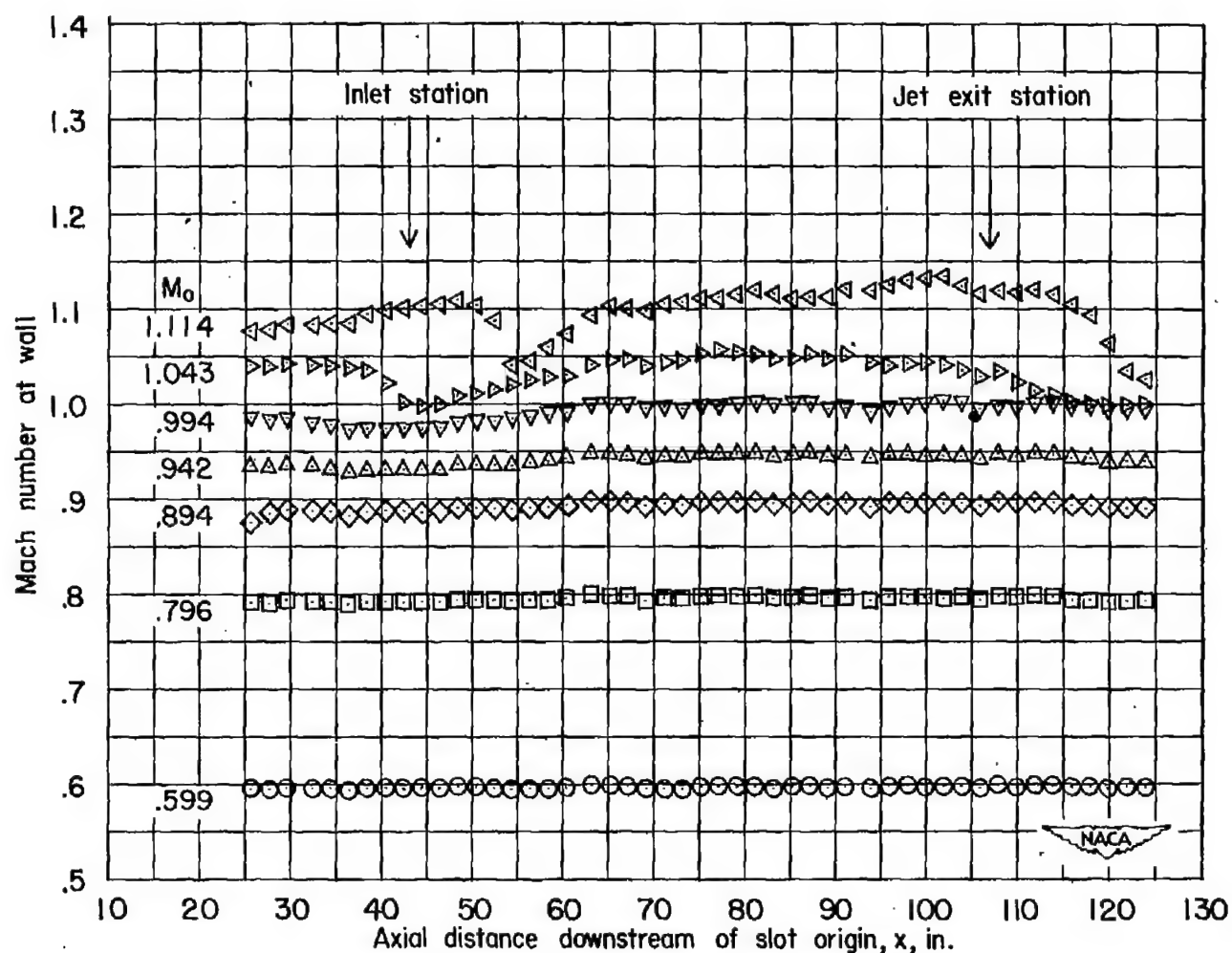
Figure 7.- Tunnel-wall Mach number distributions. Inlet choked; $\alpha = 0^\circ$.



(b) NACA 1-50-200 nose inlet.

Figure 7.- Continued.

NACA RM 152J23



(c) NACA 1-40-400 nose inlet.

Figure 7.- Concluded.

32

NACA RM L52J23

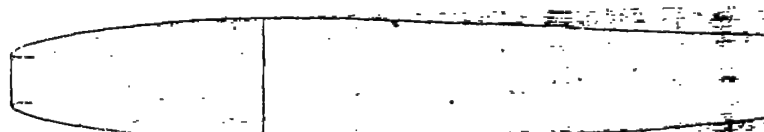
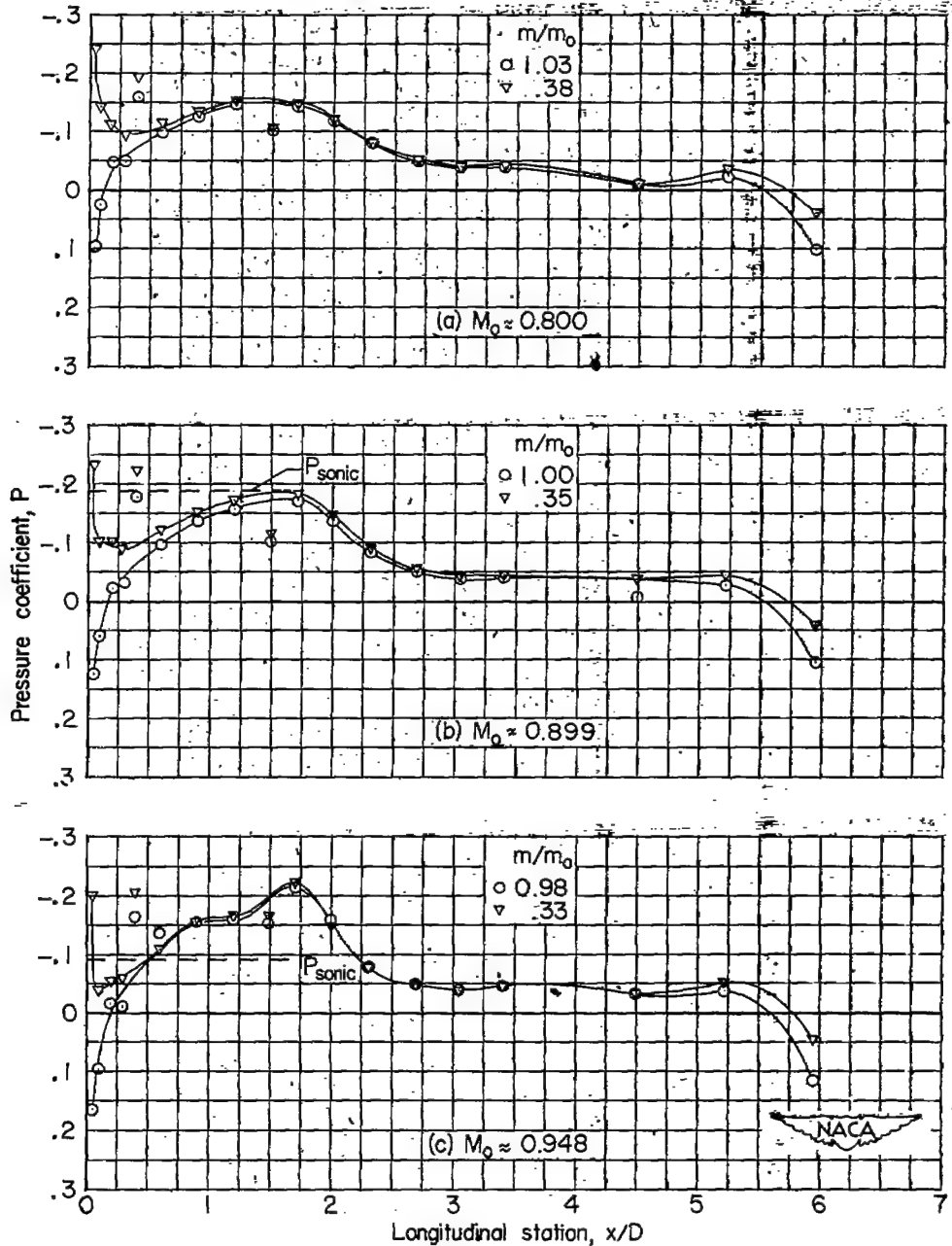


Figure 8.- Pressure distributions on external surface. NACA 1-40-200 nose inlet; $\alpha = 0^\circ$.

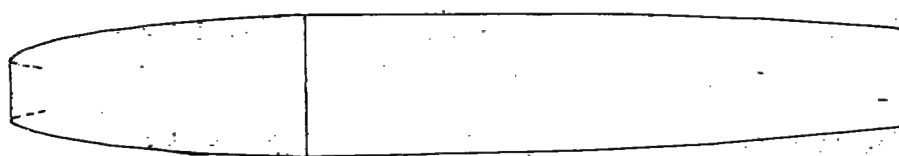
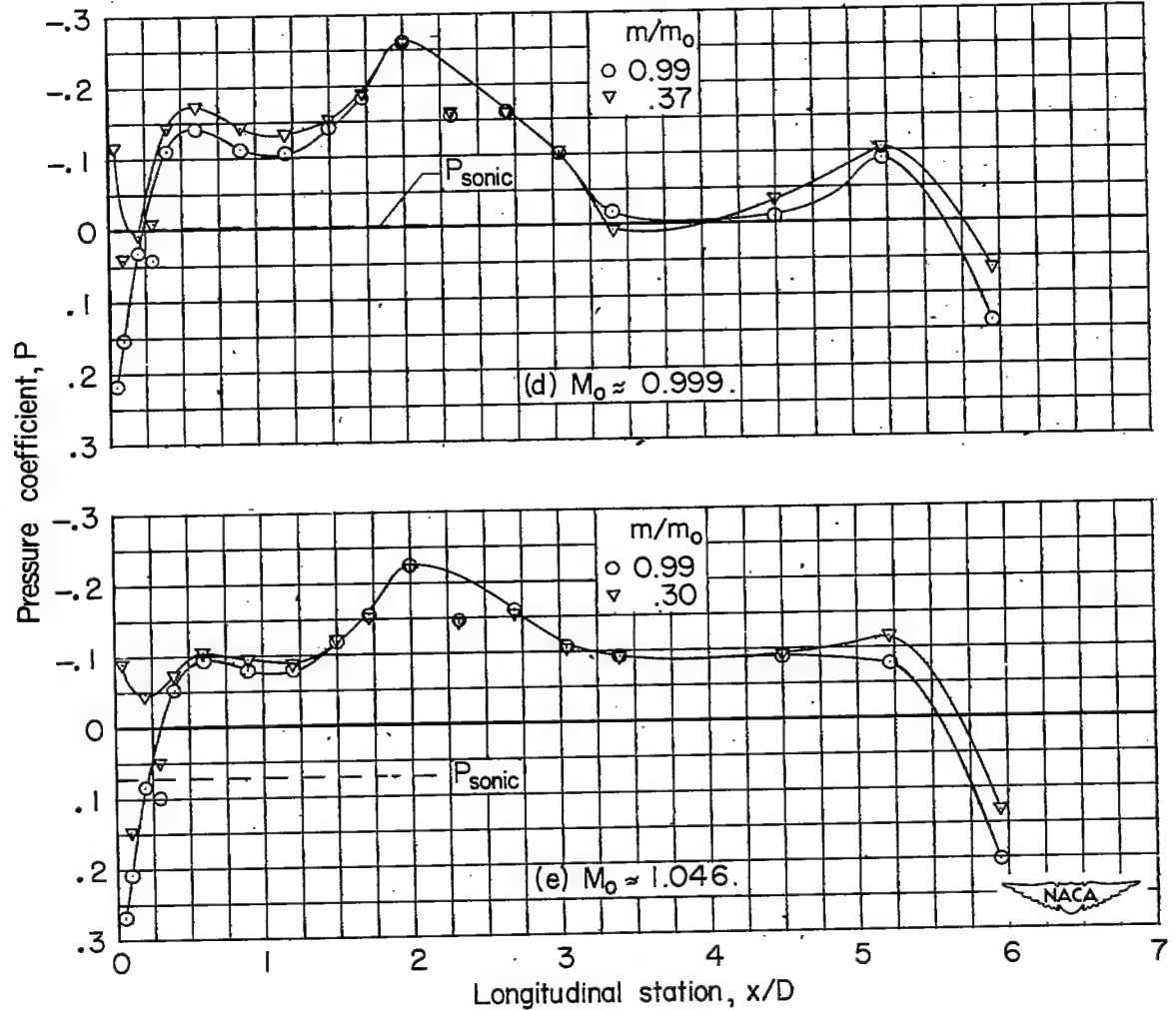


Figure 8.- NACA 1-40-200 nose inlet. Continued.

34

NACA RM L52J23

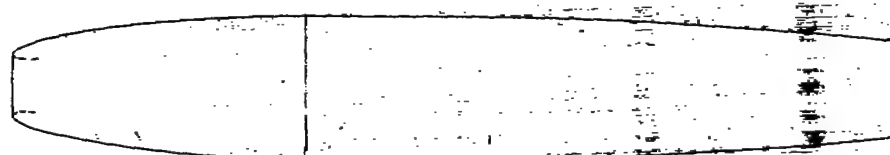
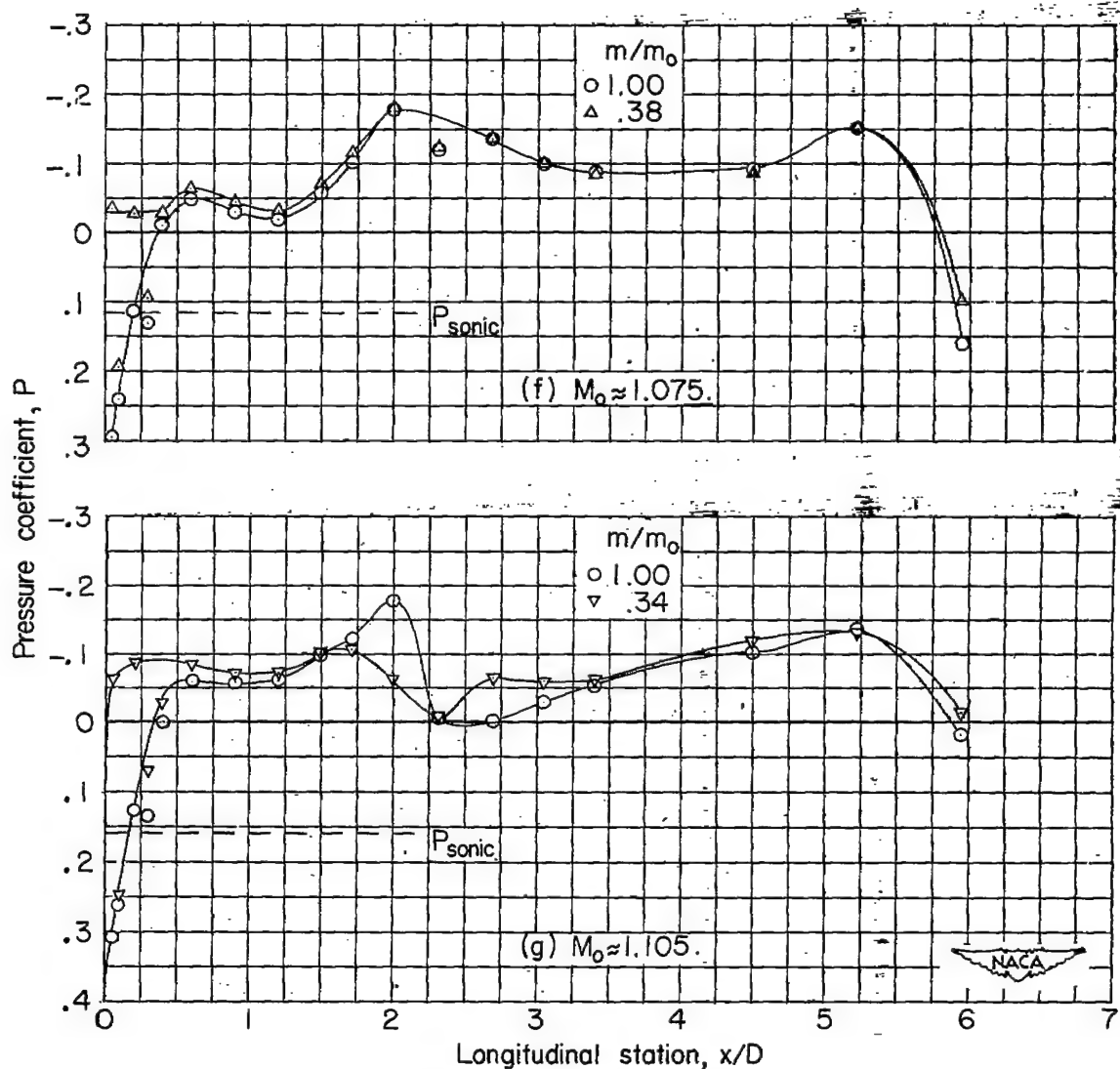


Figure 8.- NACA 1-40-200 nose inlet. Concluded.

NACA RM L52J23

35

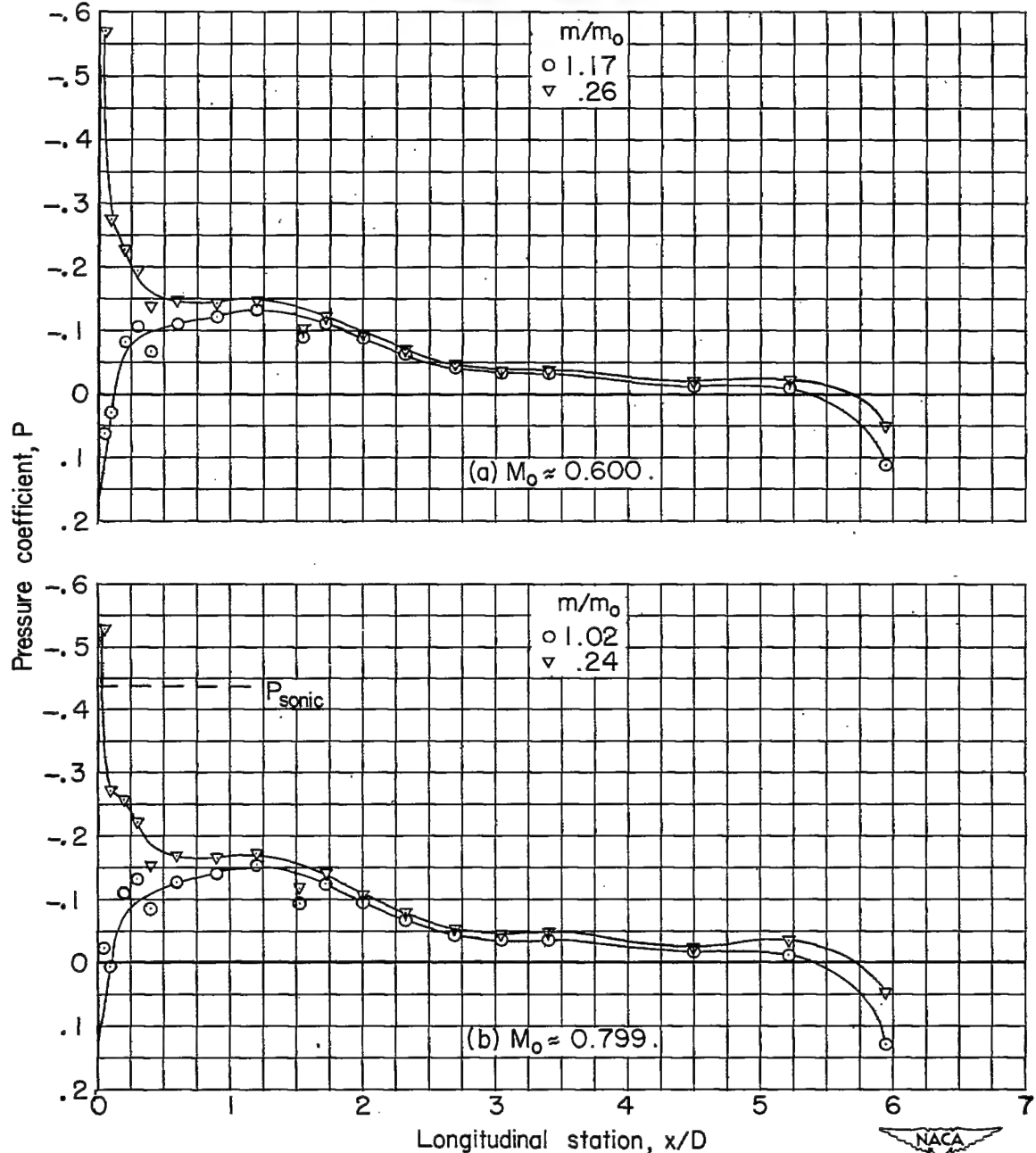
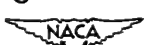
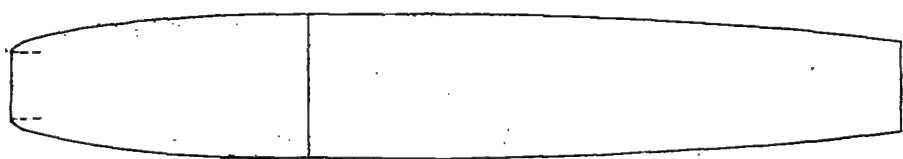
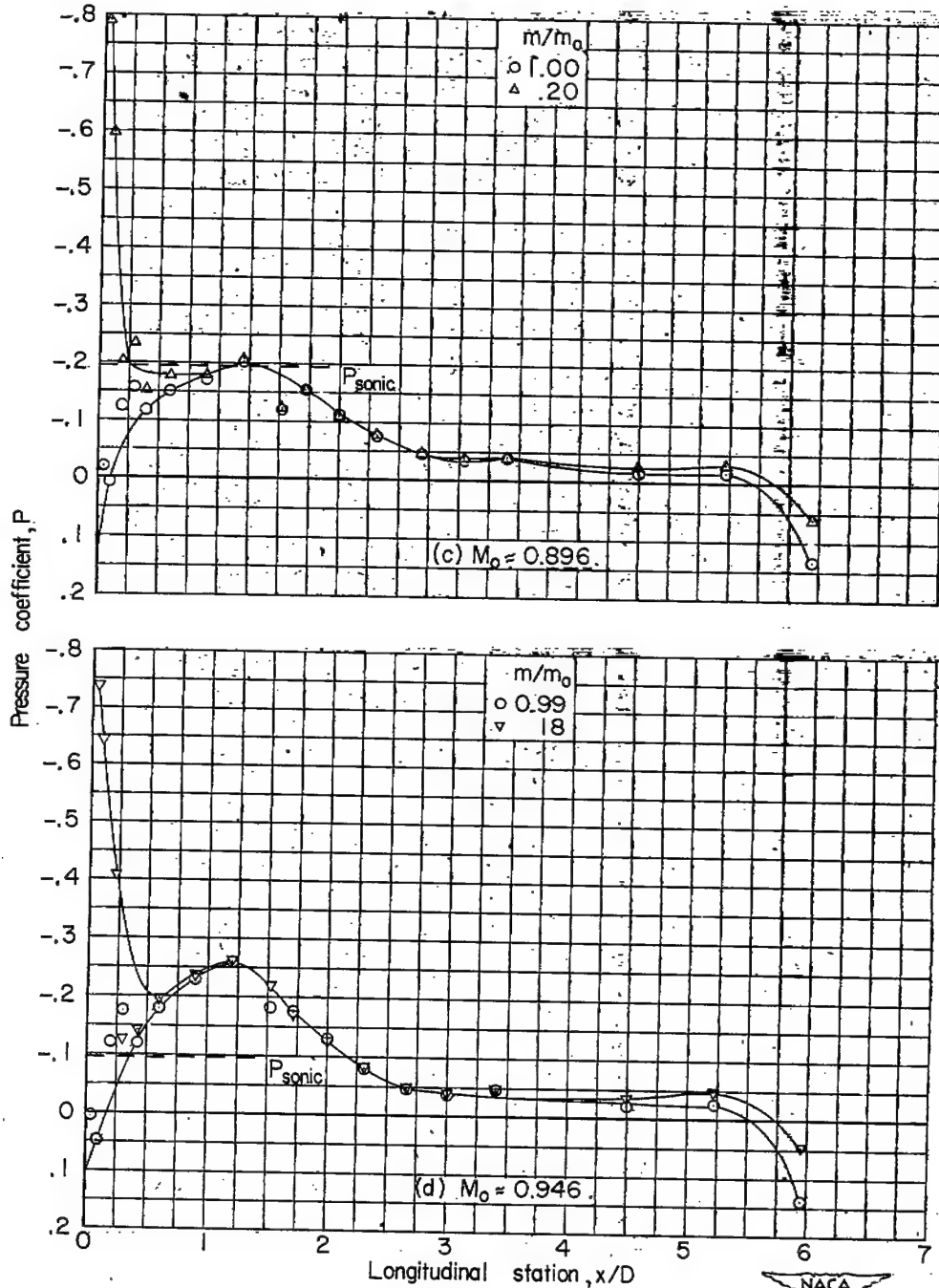


Figure 9.- Pressure distributions on external surface. NACA 1-50-200 nose inlet; $\alpha = 0^\circ$.



36

NACA RM L52J23



NACA



Figure 9.- NACA 1-50-200 nose inlet. Continued.

NACA RM 152J23

37

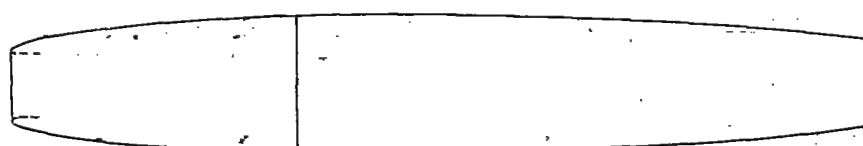
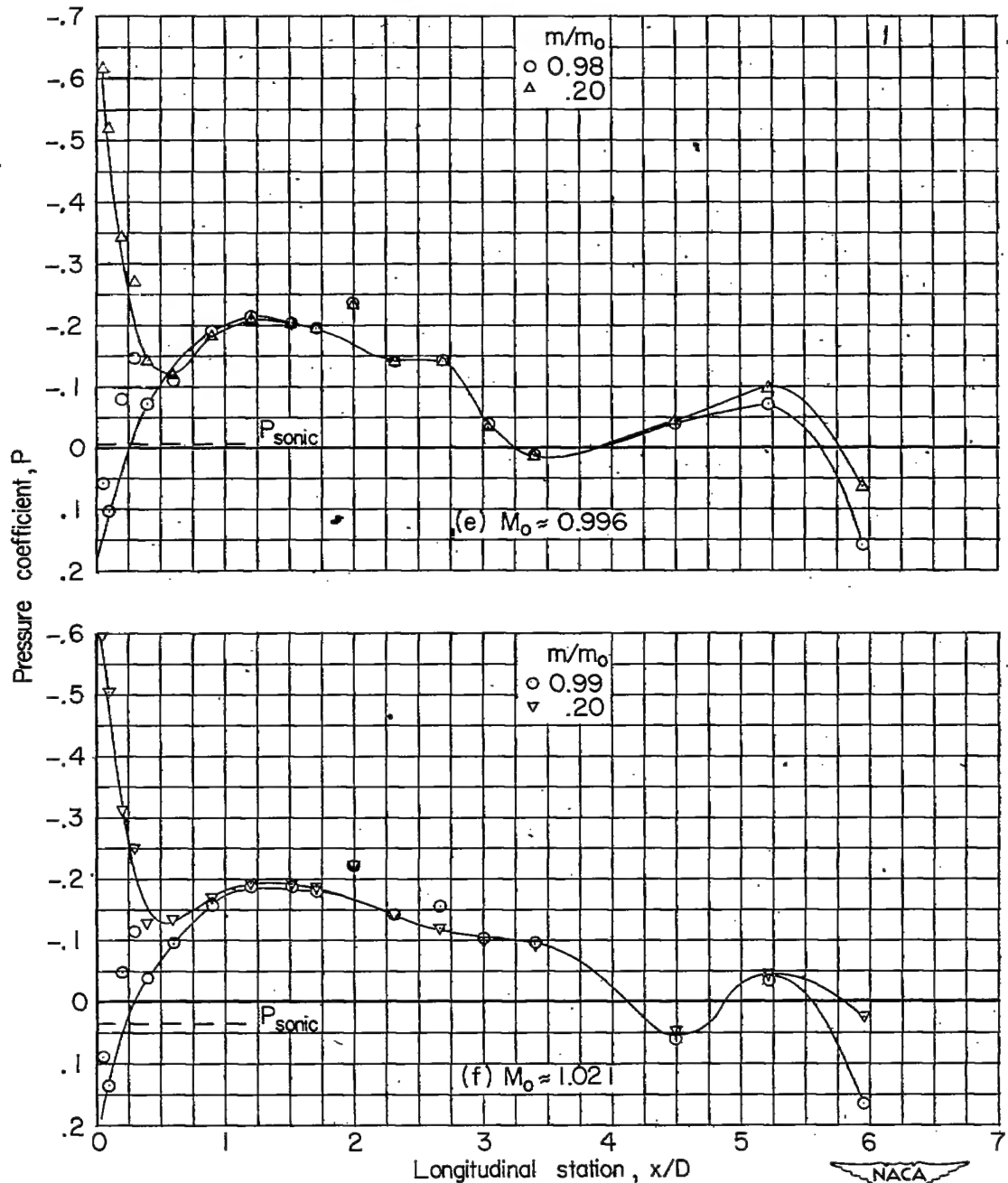


Figure 9.- NACA 1-50-200 nose inlet. Continued.

38

NACA RM L52J23

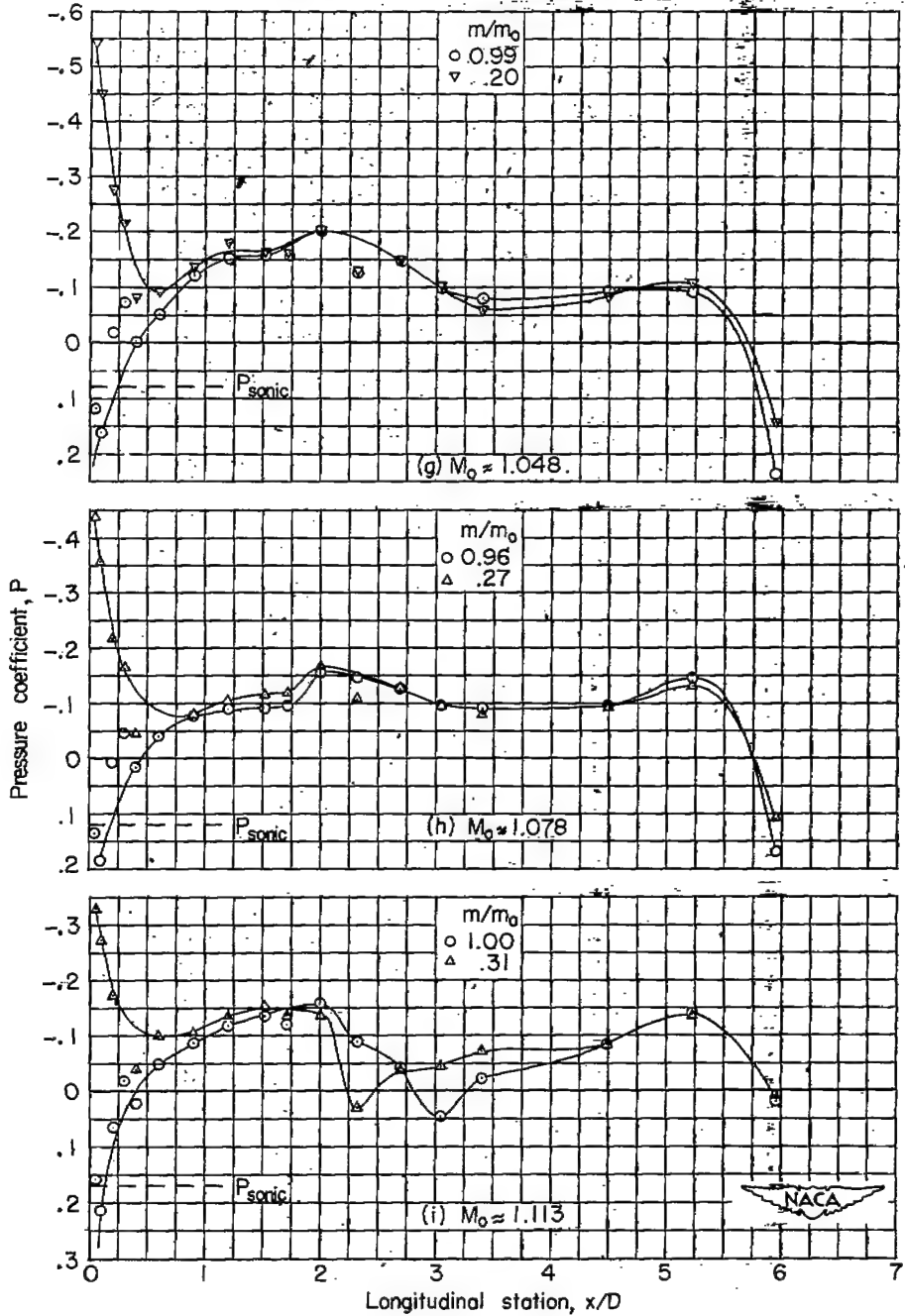


Figure 9.-- NACA 1-50-200 nose inlet. Concluded.

NACA RM L52J23

39

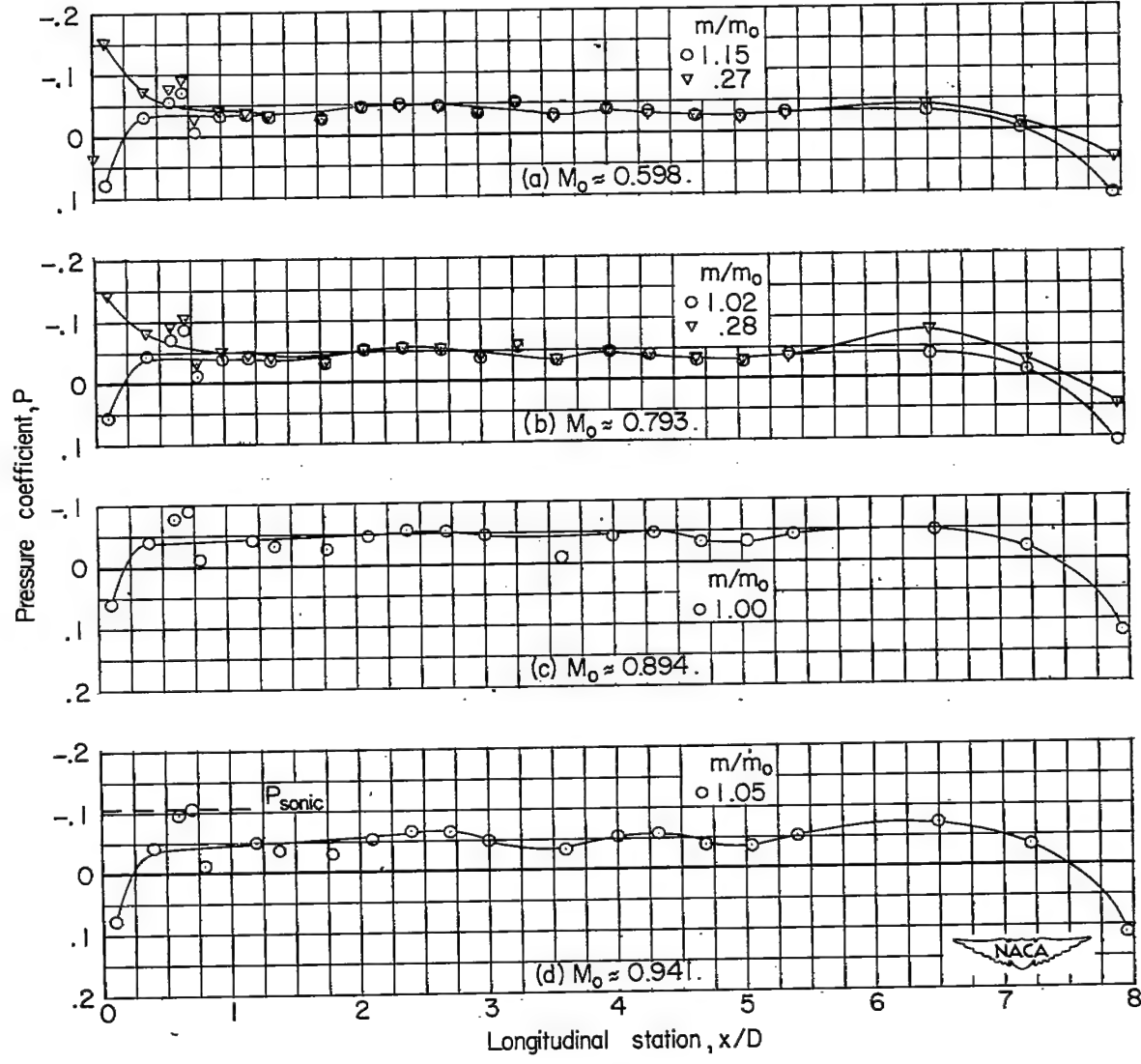
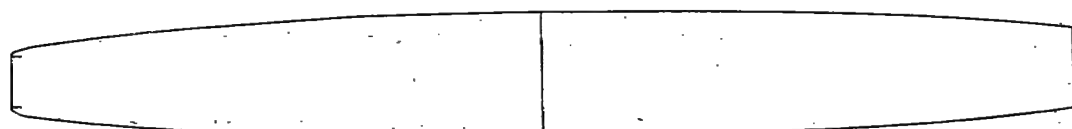


Figure 10.- Pressure distributions on external surface. NACA 1-40-400 nose inlet; $\alpha = 0^\circ$.



40

NACA RM L52J23

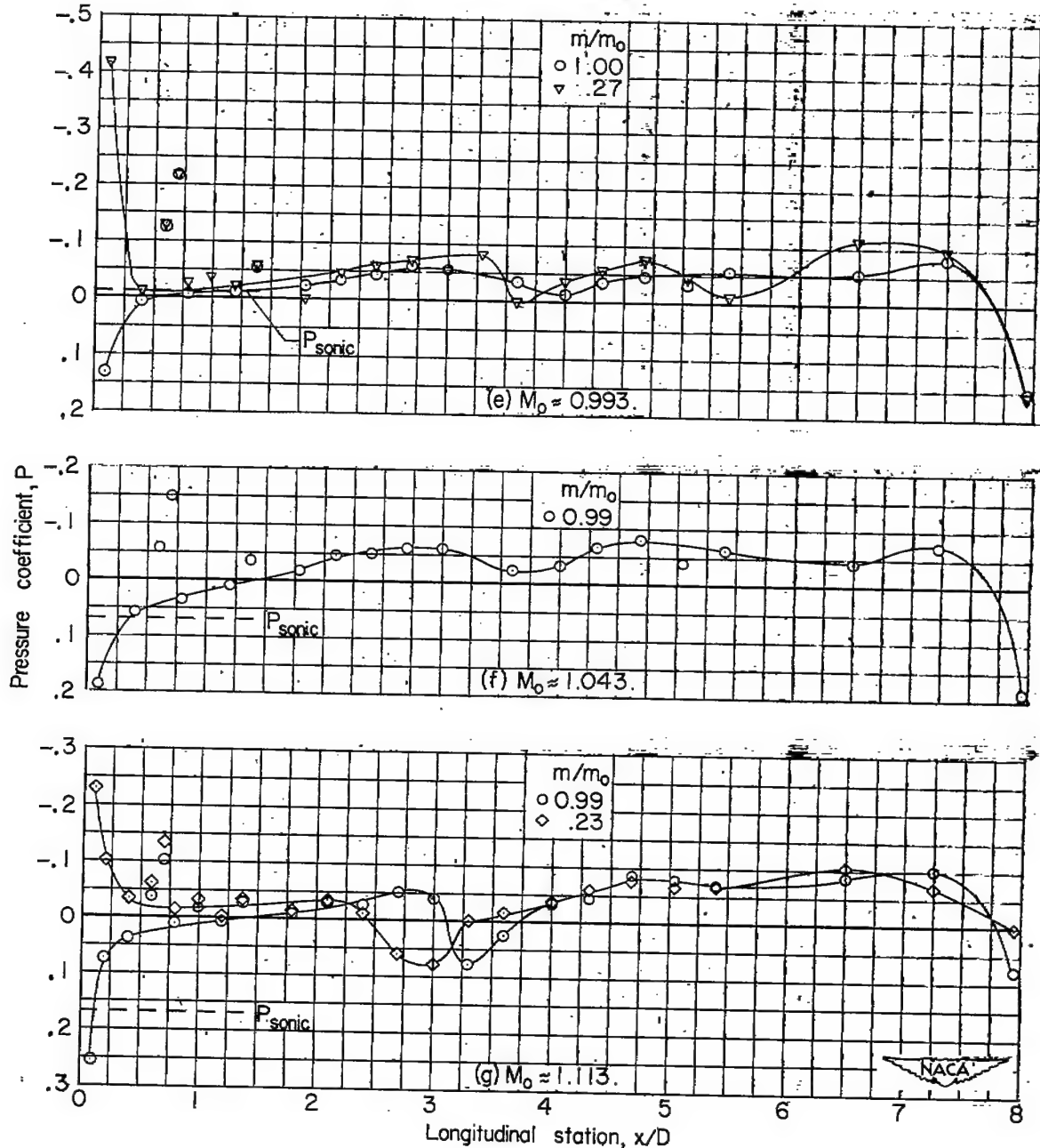


Figure 10.- NACA 1-40-400 nose inlet. Concluded.

6H

NACA RM L52J23

41

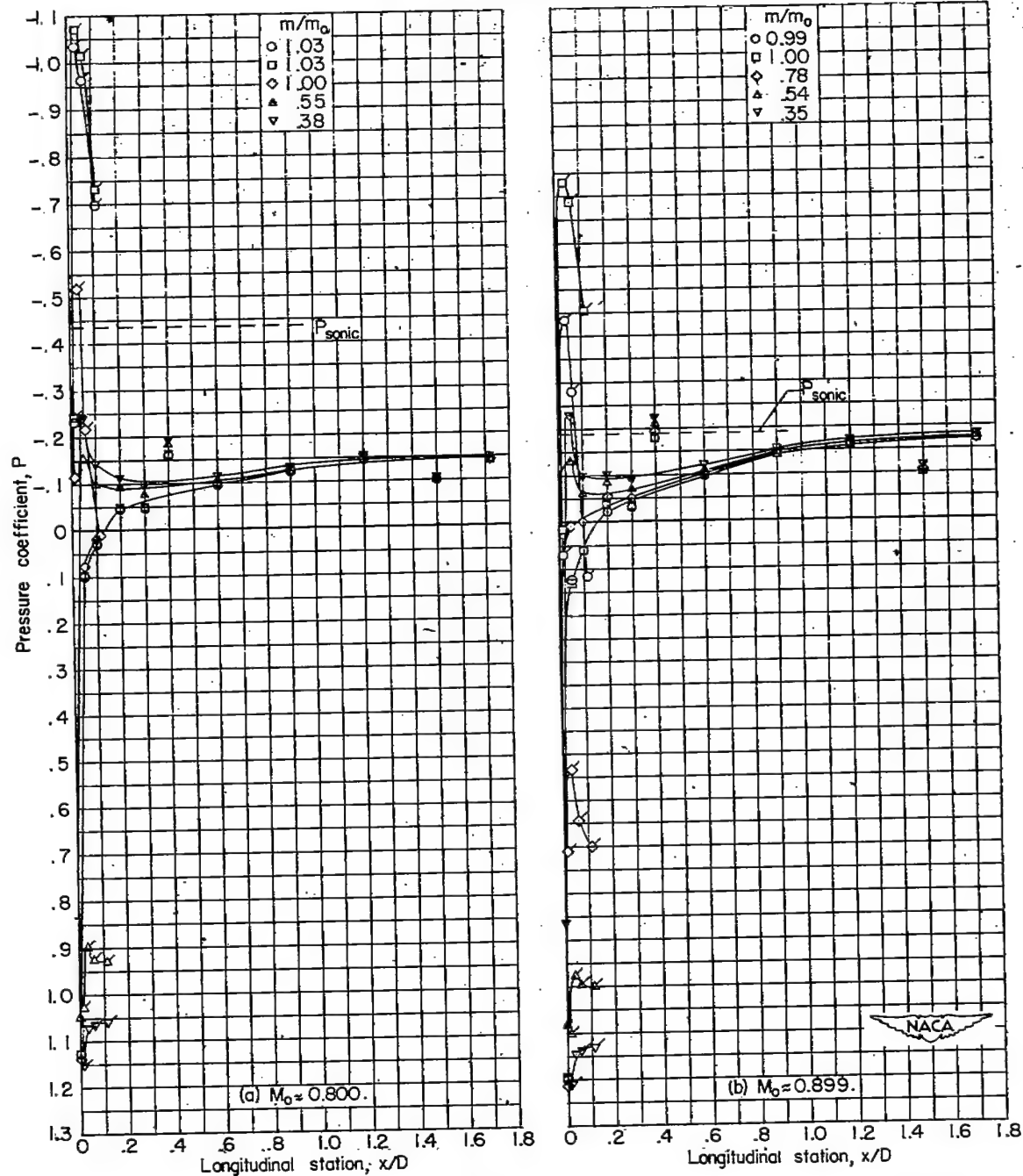


Figure 11.- Pressure distributions on lip of the NACA 1-40-200 nose inlet.
 $\alpha = 0^\circ$. Flagged symbols indicate upper-inner-lip pressures.

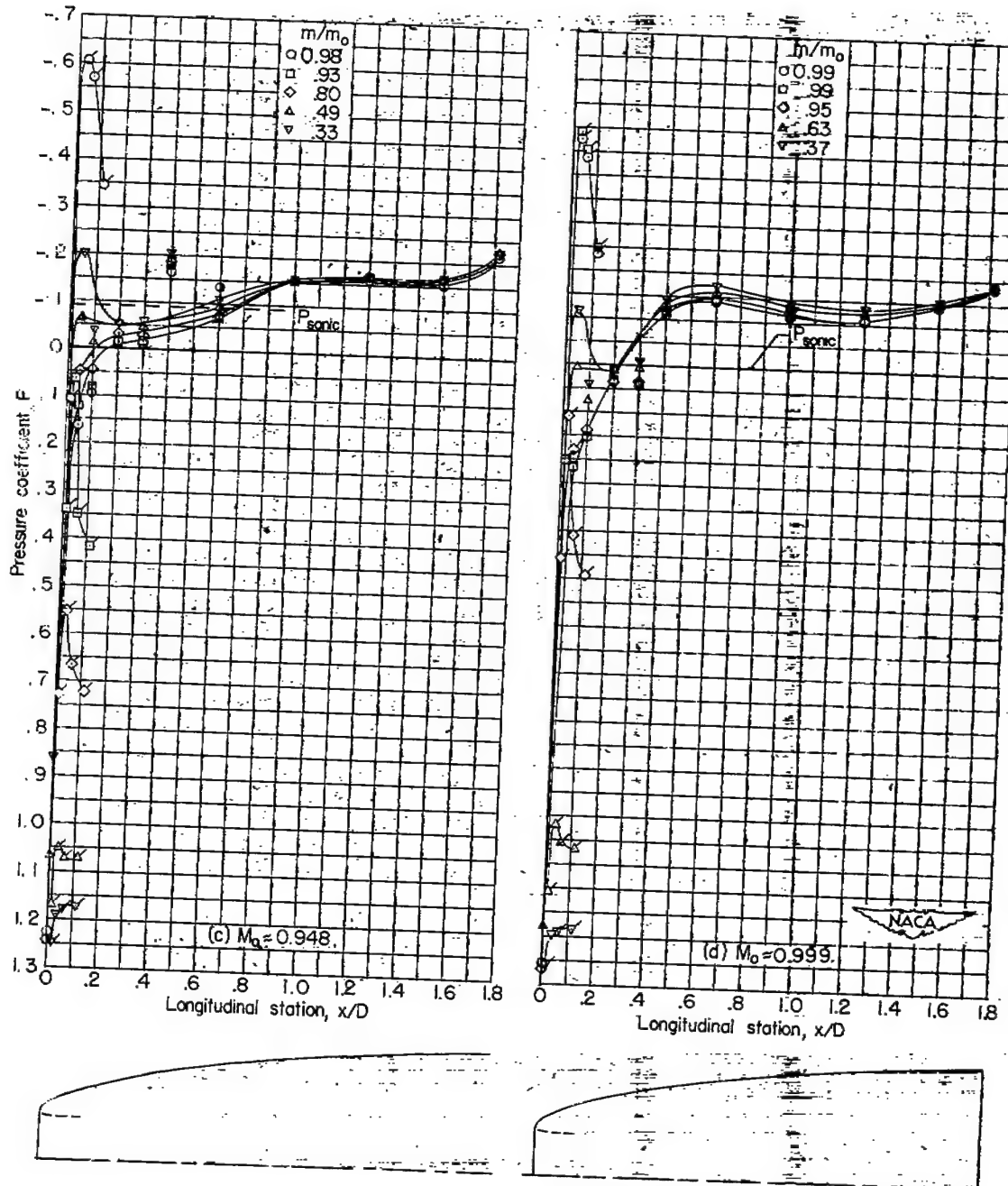


Figure 11.- NACA 1-40-200 nose inlet. Continued.

NACA RM L52J23

43

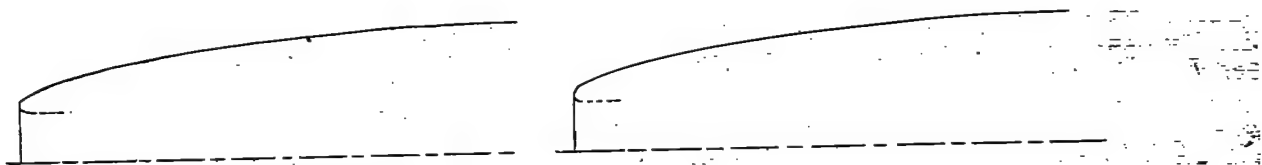
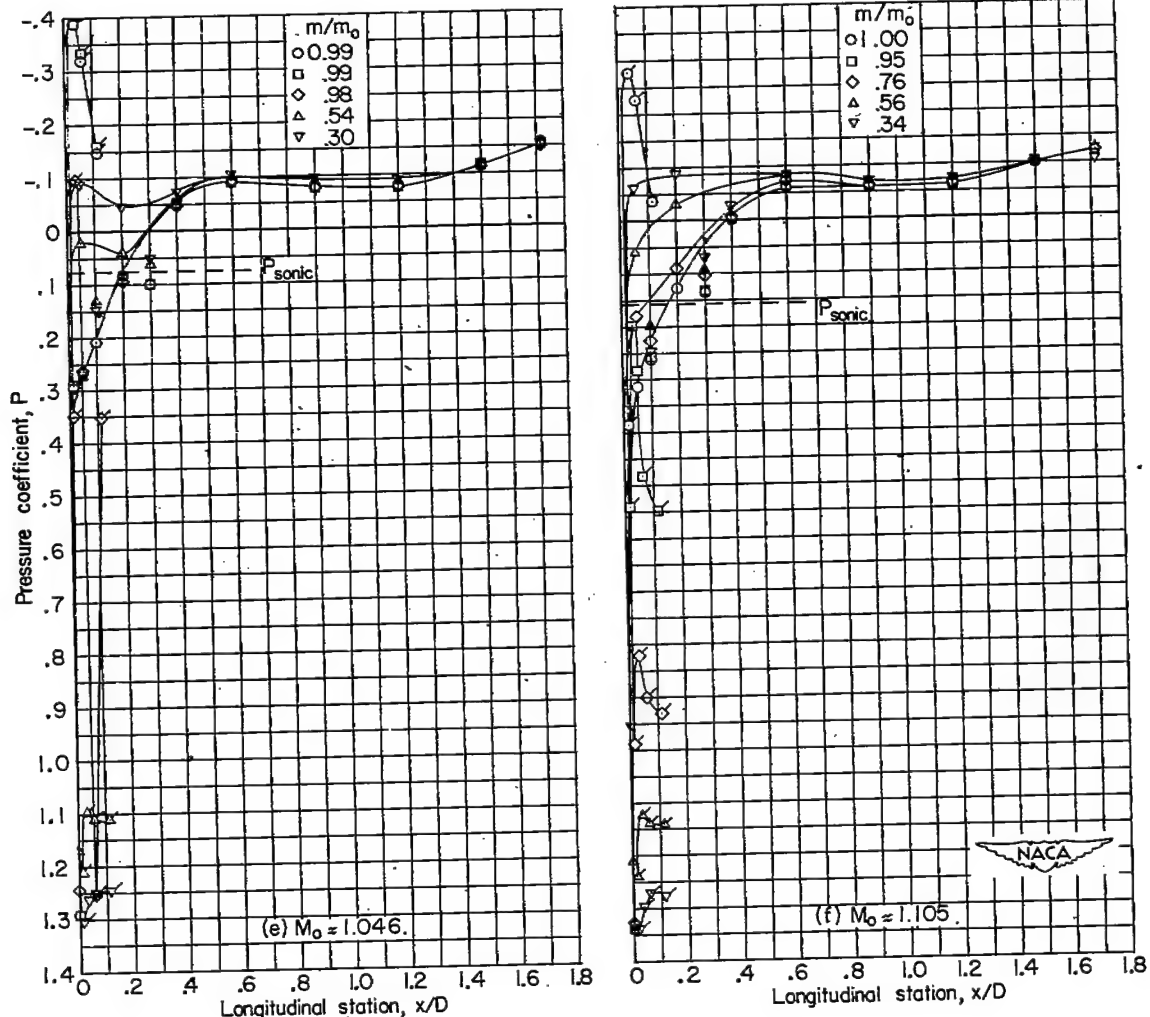


Figure 11.- NACA 1-40-200 nose inlet. Concluded.

44

NACA RM L52J23

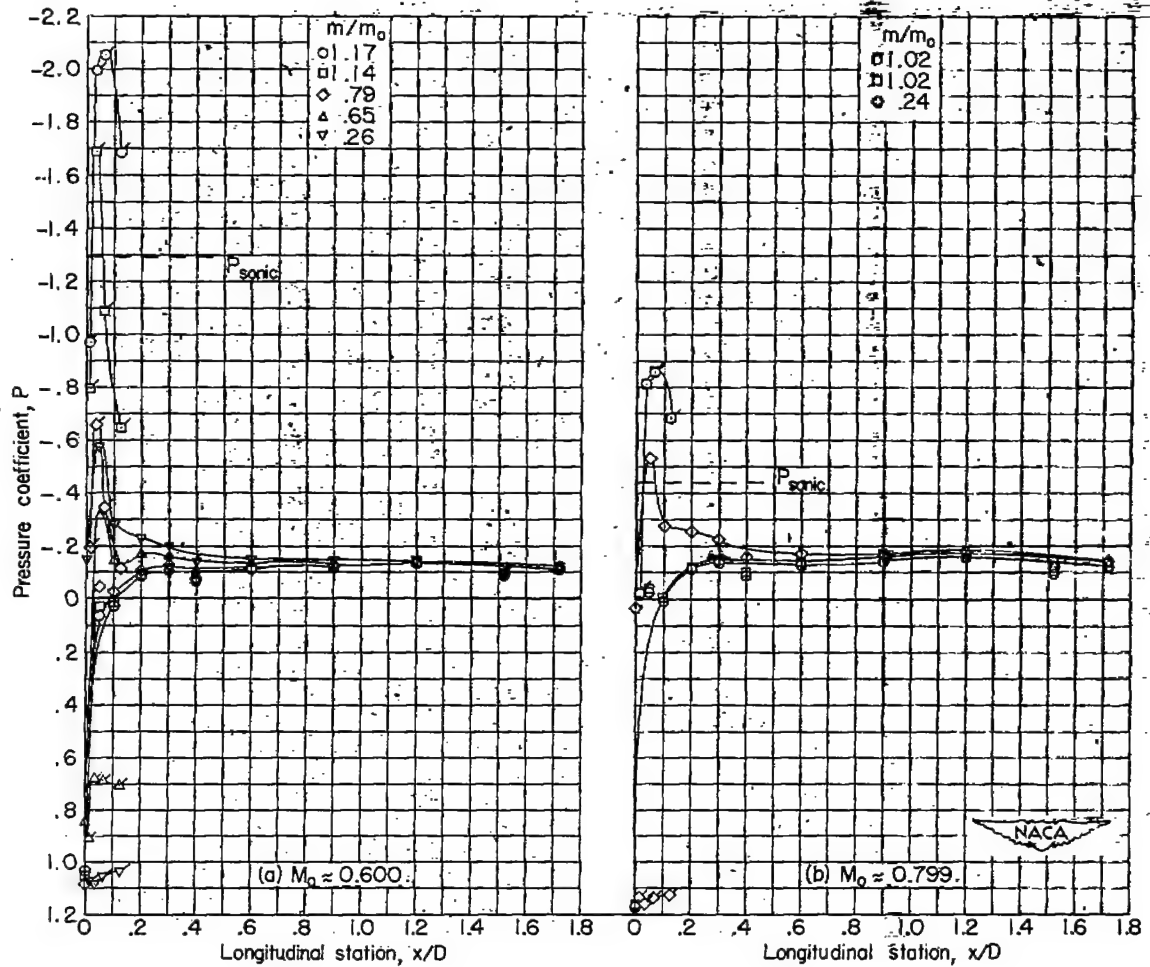


Figure 12.- Pressure distributions on lip of the NACA 1-50-200 nose inlet.
 $\alpha = 0^\circ$. Flagged symbols indicate upper-inner-lip pressures.

NACA RM L52J23

45

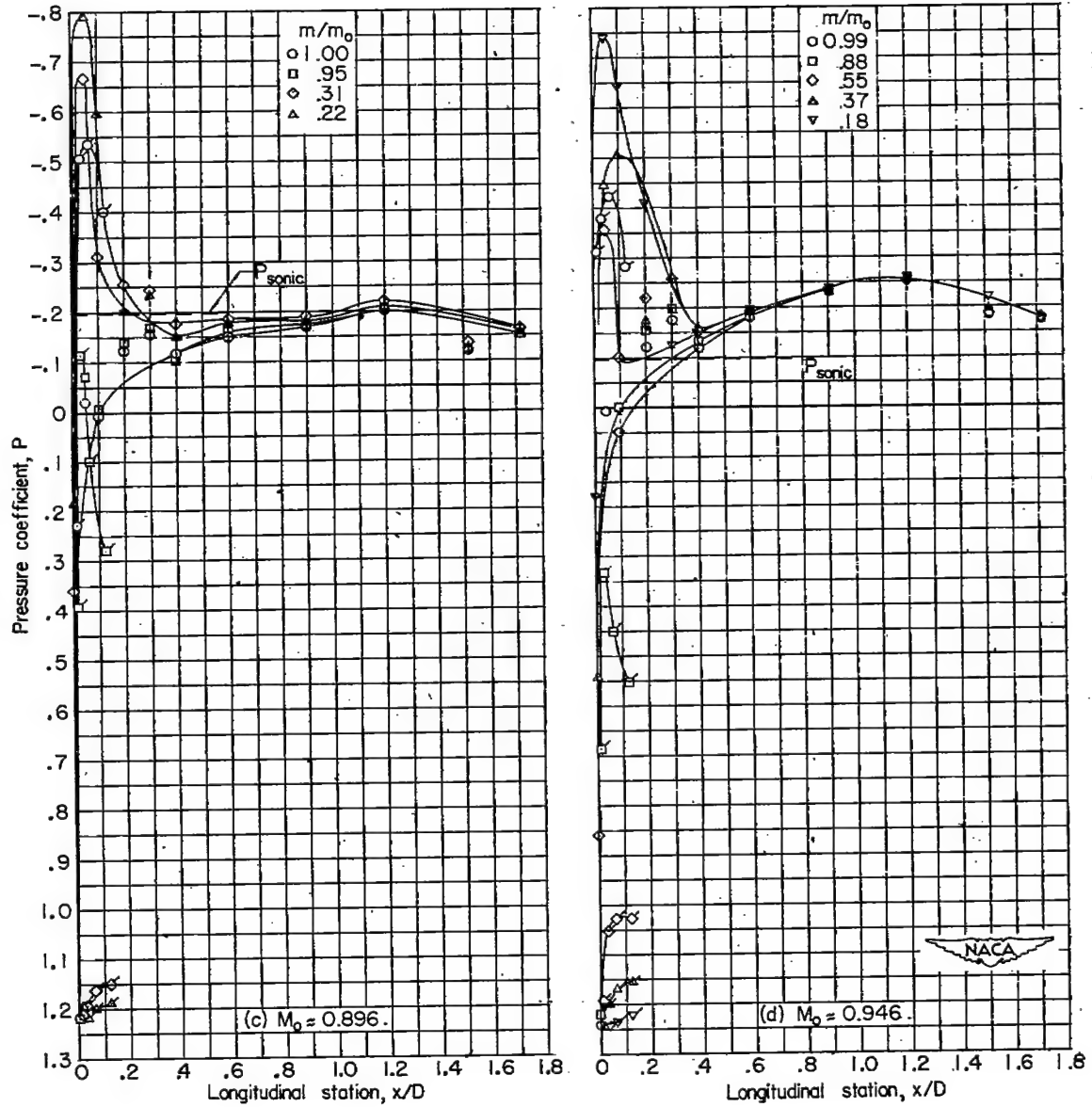


Figure 12.- NACA 1-50-200 nose inlet. Continued.

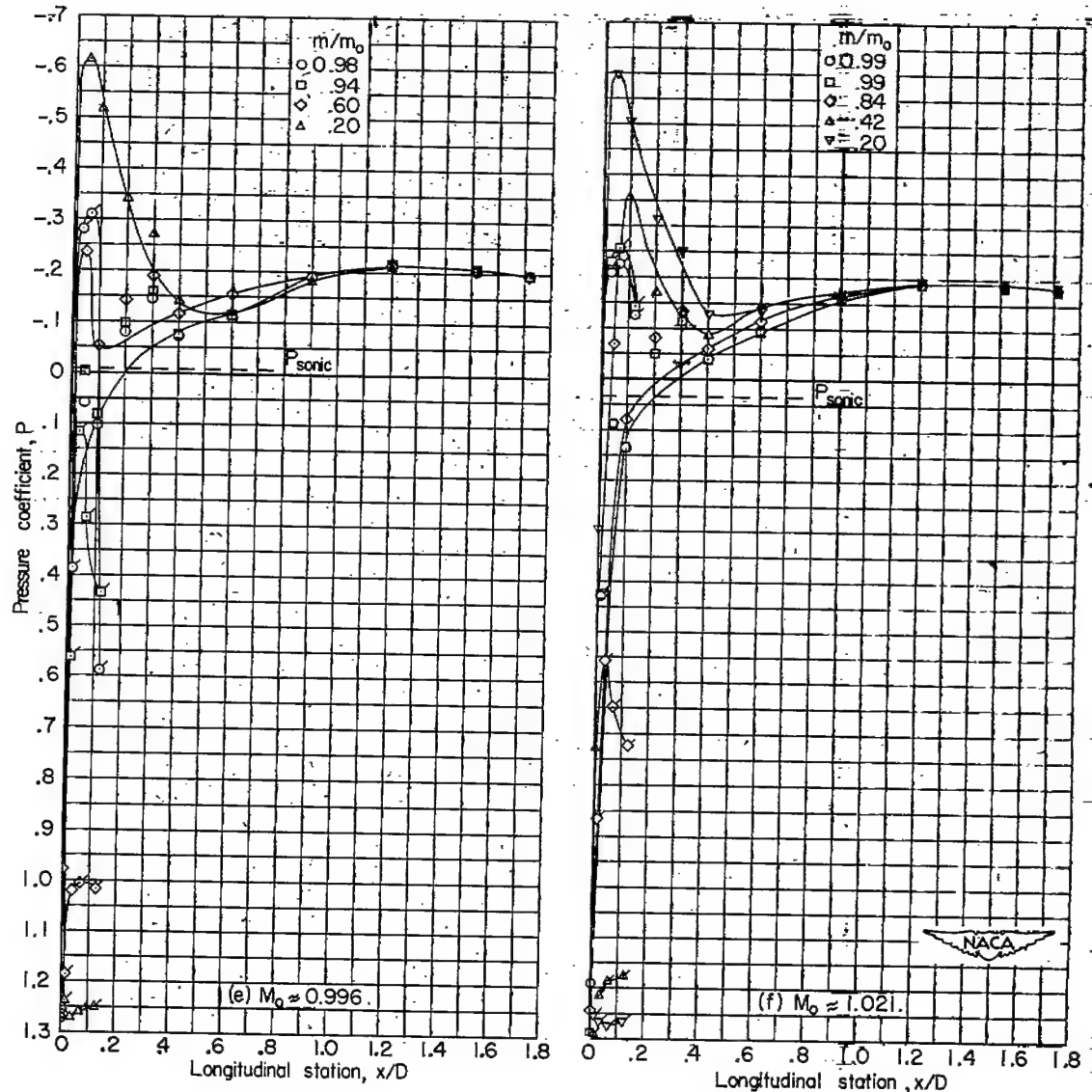


Figure 12.- NACA 1-50-200 nose inlet. Continued.

NACA RM 152J23 -

47

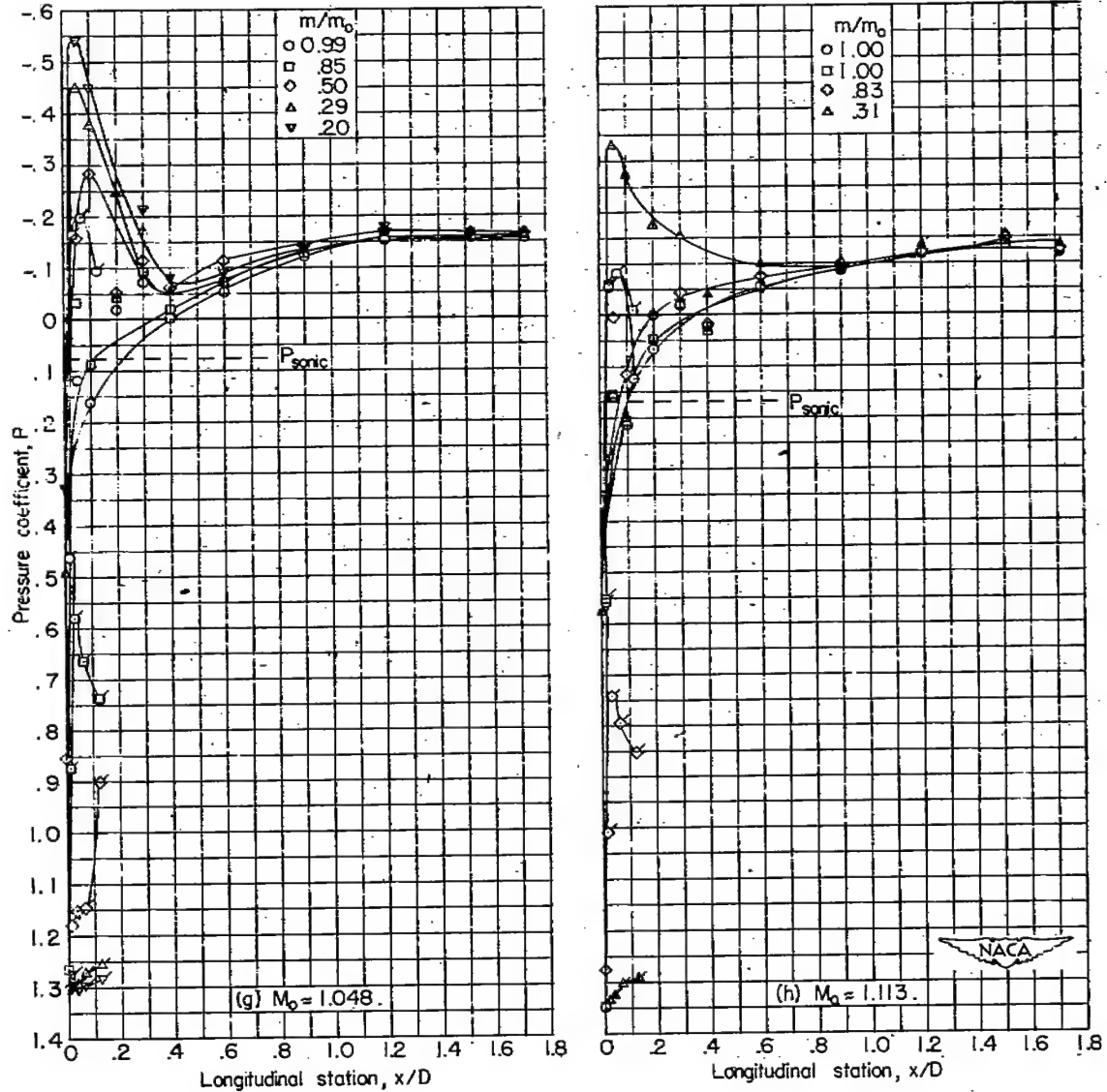


Figure 12.- NACA 1-50-200 nose inlet. Concluded.

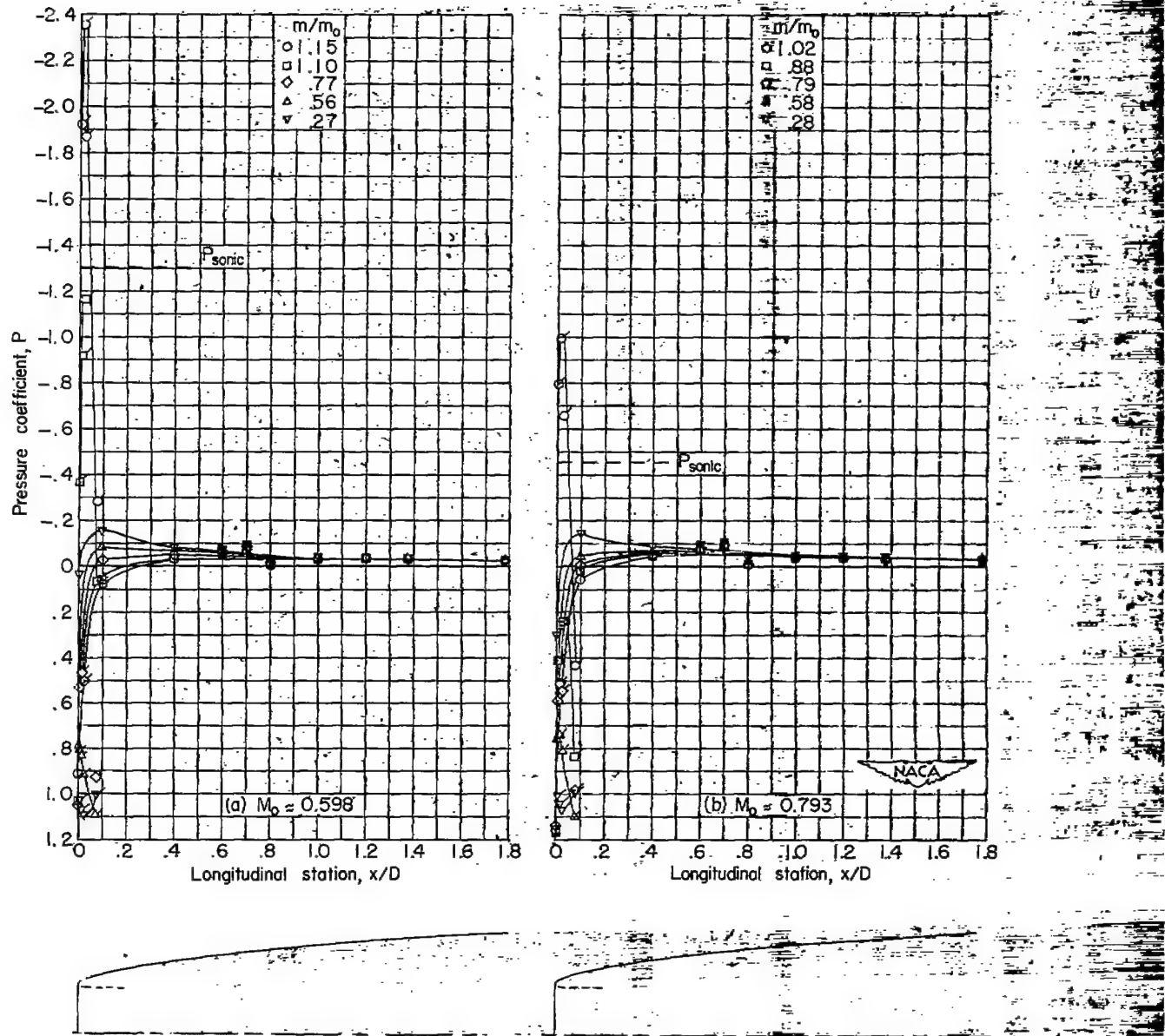


Figure 13.- Pressure distributions on lip of the NACA 1-40-400 nose inlet.
 $\alpha = 0^\circ$. Flagged symbols indicate upper-inner-lip pressures.

7H

NACA RM L52J23

49

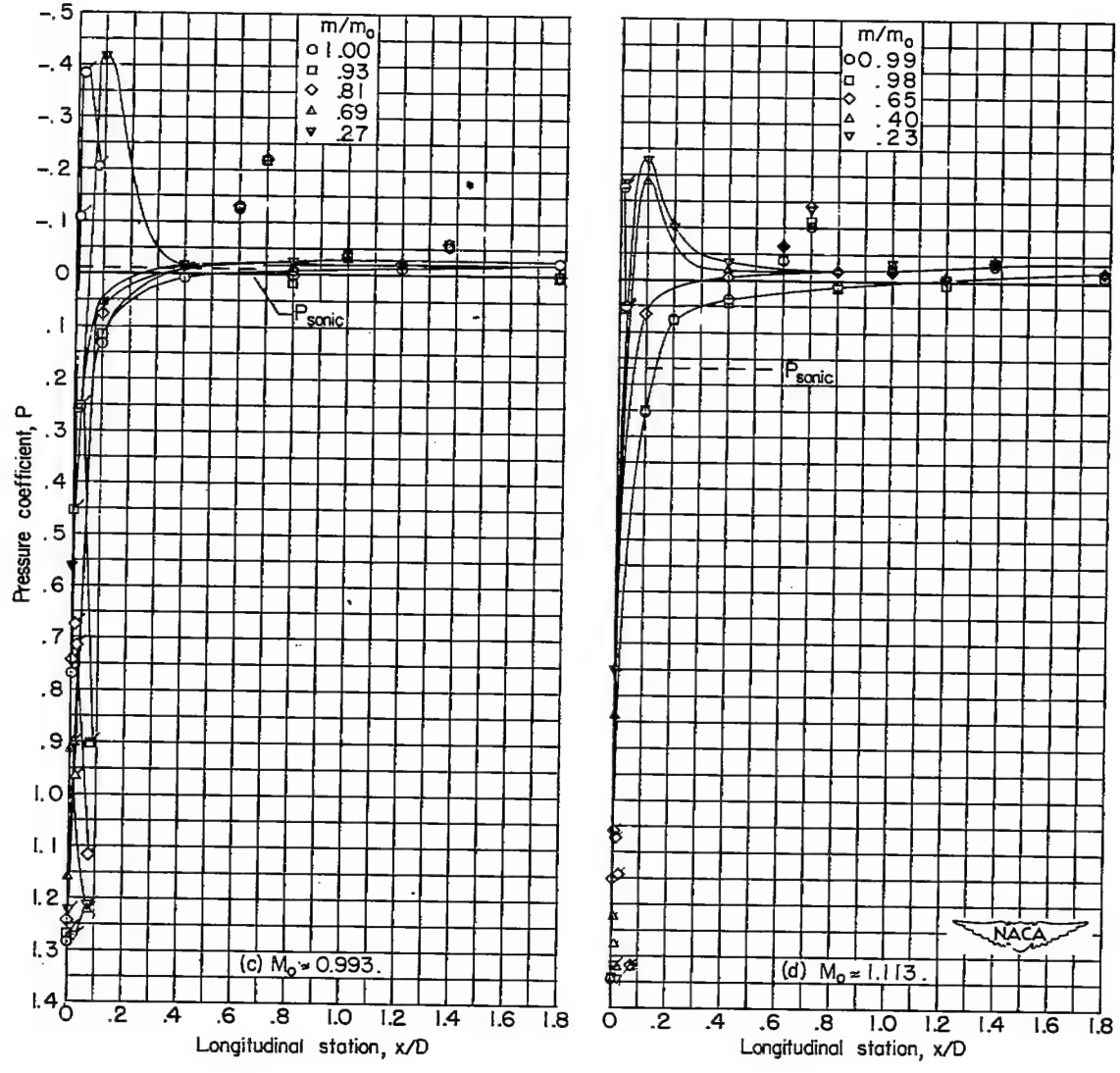


Figure 13.- NACA 1-40-400 nose inlet. Concluded.

CONFIDENTIAL

50

NACA RM L52J23

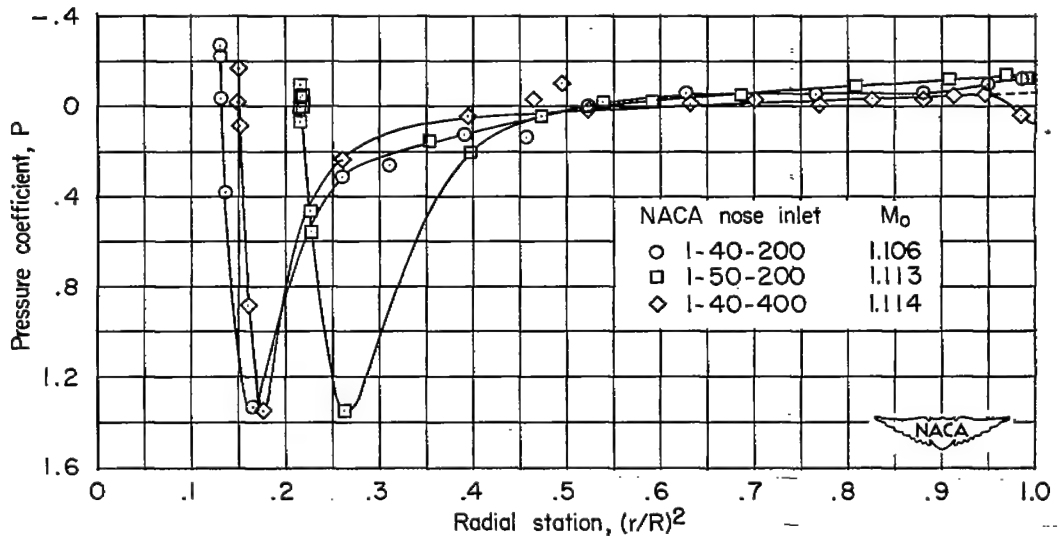
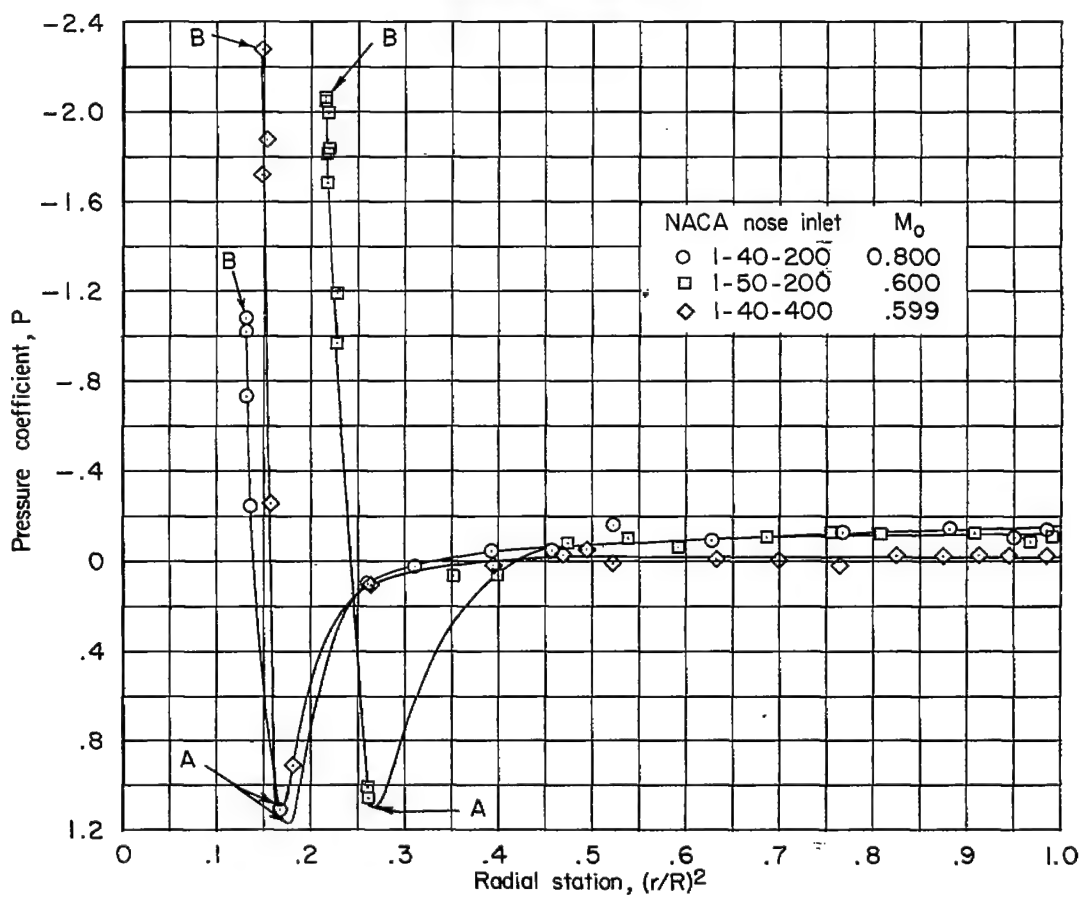
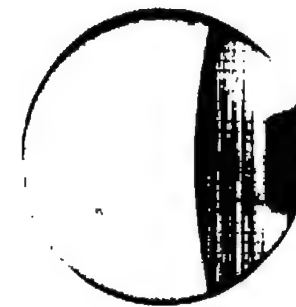
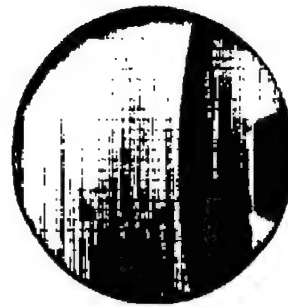
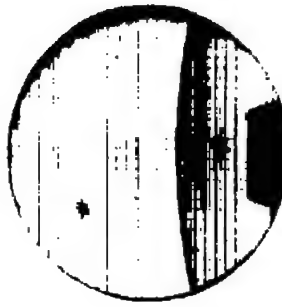
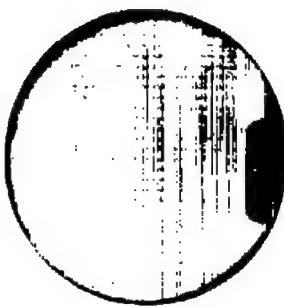
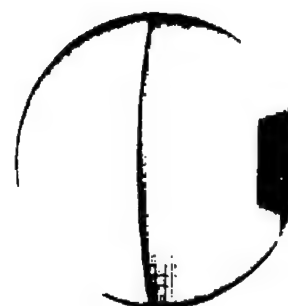
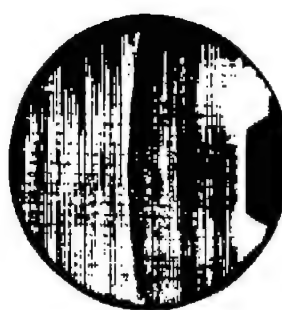


Figure 14.- Sample pressure distributions integrated to obtain forebody-pressure drag. Inlet choked; $\alpha = 0^\circ$.

NACA RM 152J23

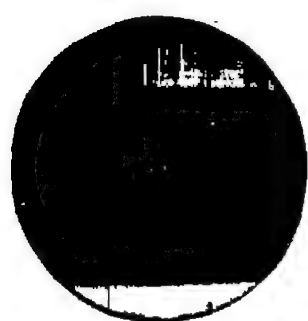


(a) Nose region of the NACA 1-40-400 nose inlet.

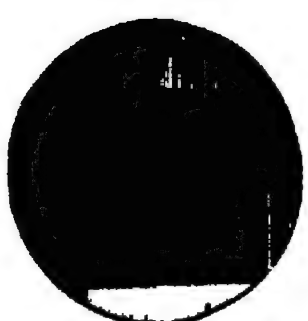


Figure 15.- Schlieren photographs.

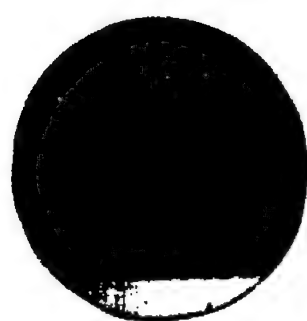
L-76986



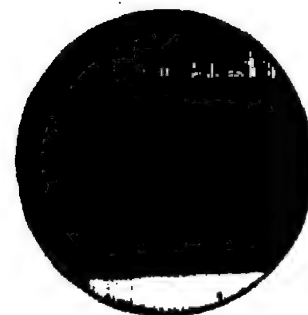
$M_0 = 0.948$
 $m/m_0 = 0.33$



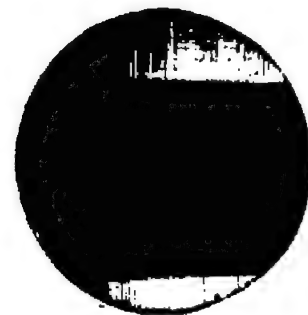
$M_0 = 0.997$
 $m/m_0 = 0.37$



$M_0 = 1.046$
 $m/m_0 = 0.30$



$M_0 = 0.948$
Inlet choked



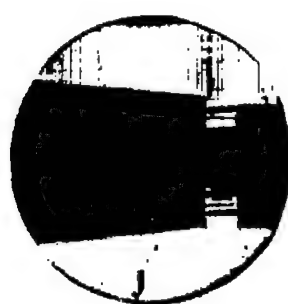
$M_0 = 0.999$
Inlet choked

(b) Afterbody region of the NACA 1-40-200 nose inlet.
Center of photograph located at $x/D = 3.725$.

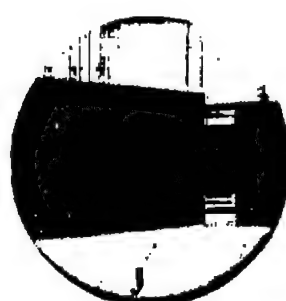
Figure 15.- Continued.

NACA
L-76987

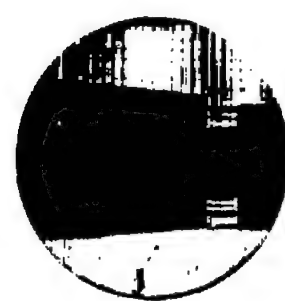
NACA RM 152123



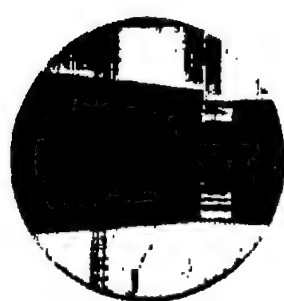
$M_0 = 0.895$



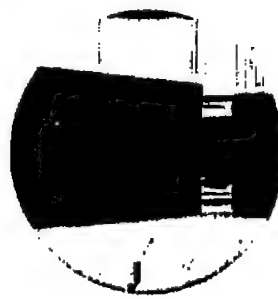
$M_0 = 0.946$



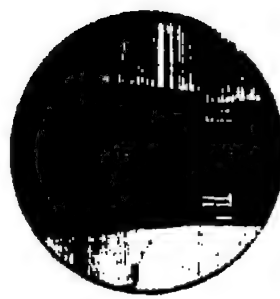
$M_0 = 0.971$



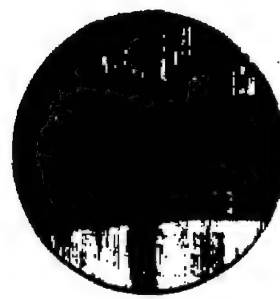
$M_0 = 0.996$



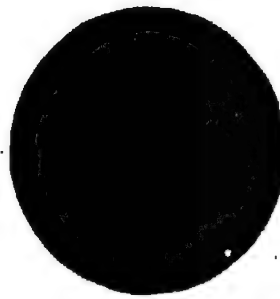
$M_0 = 1.024$



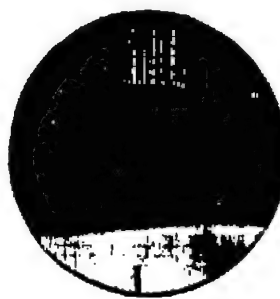
$M_0 = 1.046$



$M_0 = 1.055$



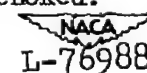
$M_0 = 1.079$



$M_0 = 1.113$

(c) Jet region of the NACA 1-50-200 nose inlet. Inlet choked.

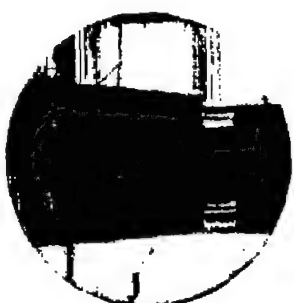
Figure 15.- Continued.

 NACA
L-76988

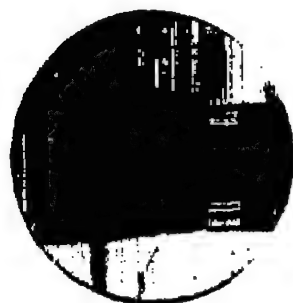
54



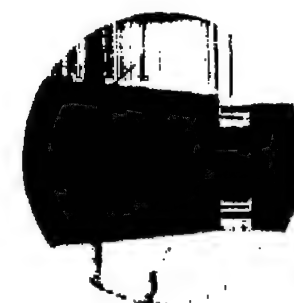
$M_0 = 1.045$
 $m/m_0 = 0.41$



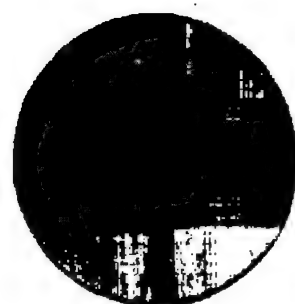
$M_0 = 1.042$
 $m/m_0 = 0.56$



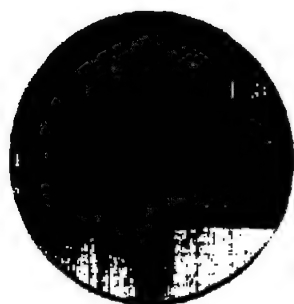
$M_0 = 1.045$
 $m/m_0 = 0.73$



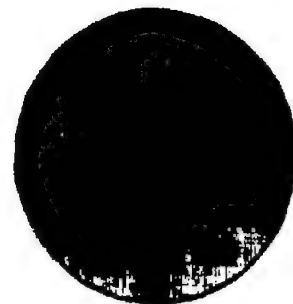
$M_0 = 1.046$
Inlet choked



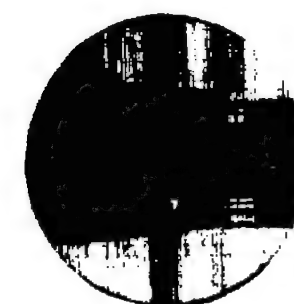
$M_0 = 1.054$
 $m/m_0 = 0.33$



$M_0 = 1.054$
 $m/m_0 = 0.58$



$M_0 = 1.055$
 $m/m_0 = 0.79$



$M_0 = 1.055$
Inlet choked

(d) Jet region of the NACA 1-50-200 nose inlet.

Figure 15.- Concluded.

NACA
L-76989

NACA RM 152J23

NACA RM 152123

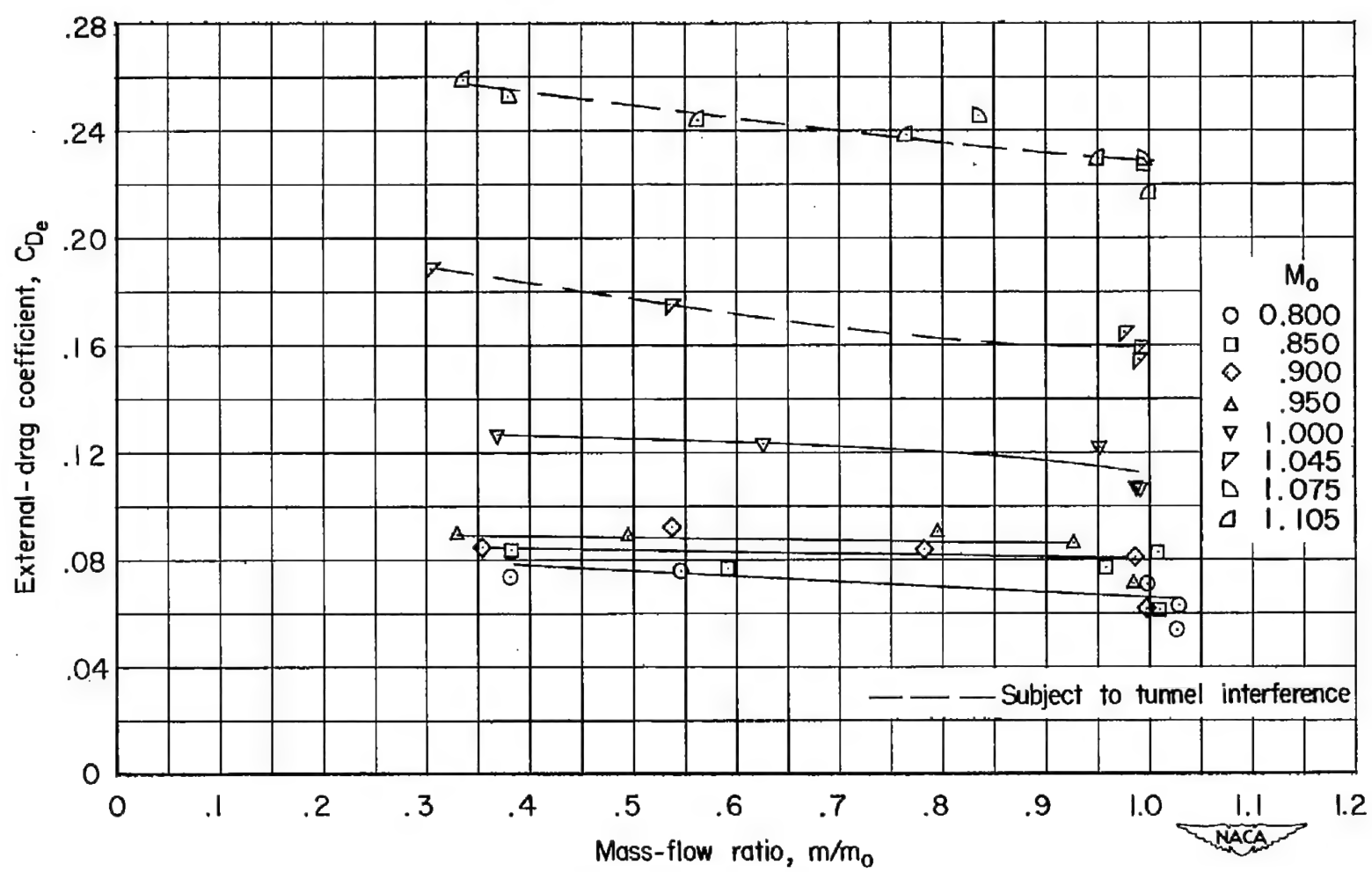


Figure 16.- Variation of external-drag coefficient with mass-flow ratio.
NACA 1-40-200 nose inlet; $\alpha = 0^\circ$.

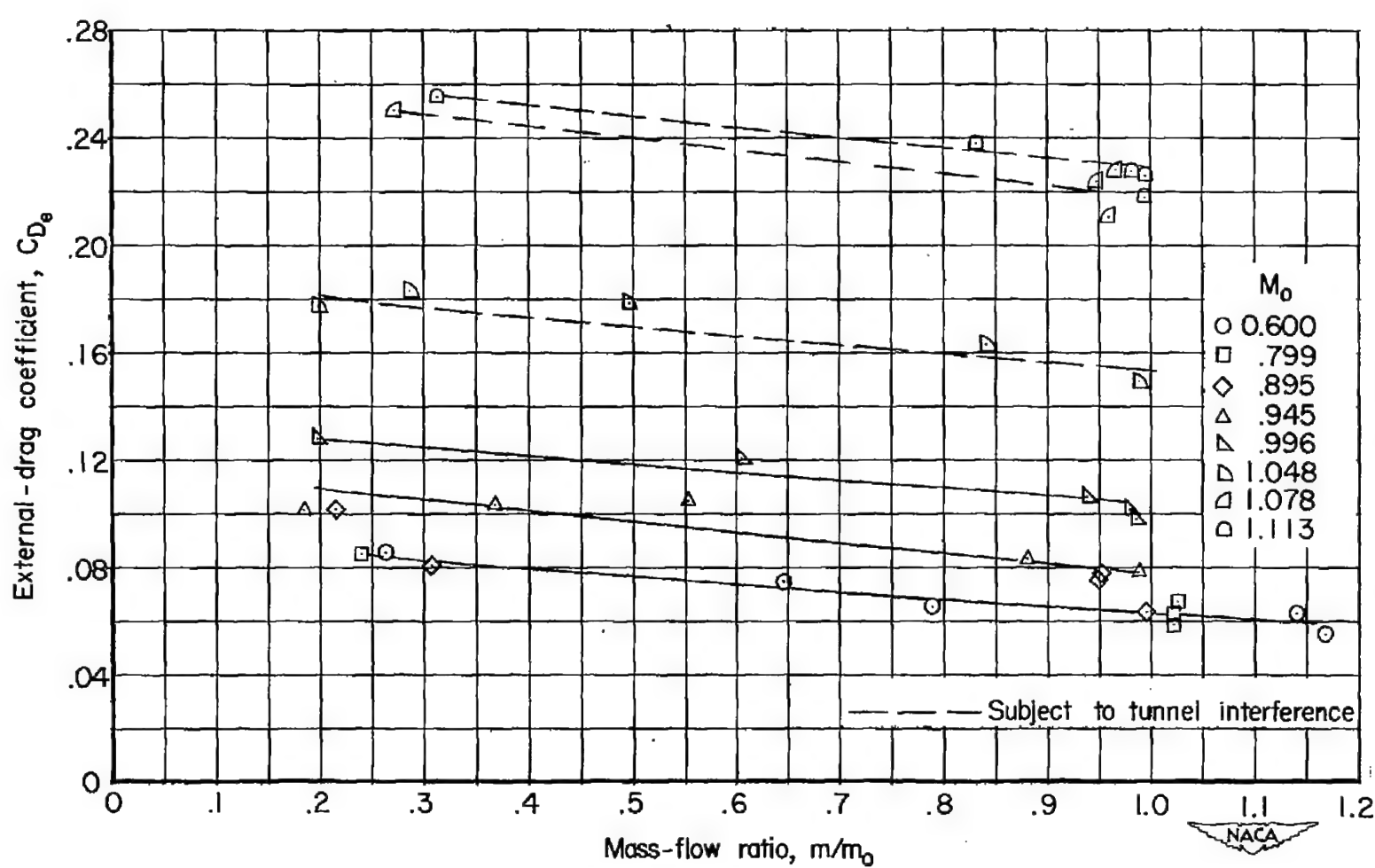


Figure 17.- Variation of external-drag coefficient with mass-flow ratio.
NACA 1-50-200 nose inlet; $\alpha = 0^\circ$.

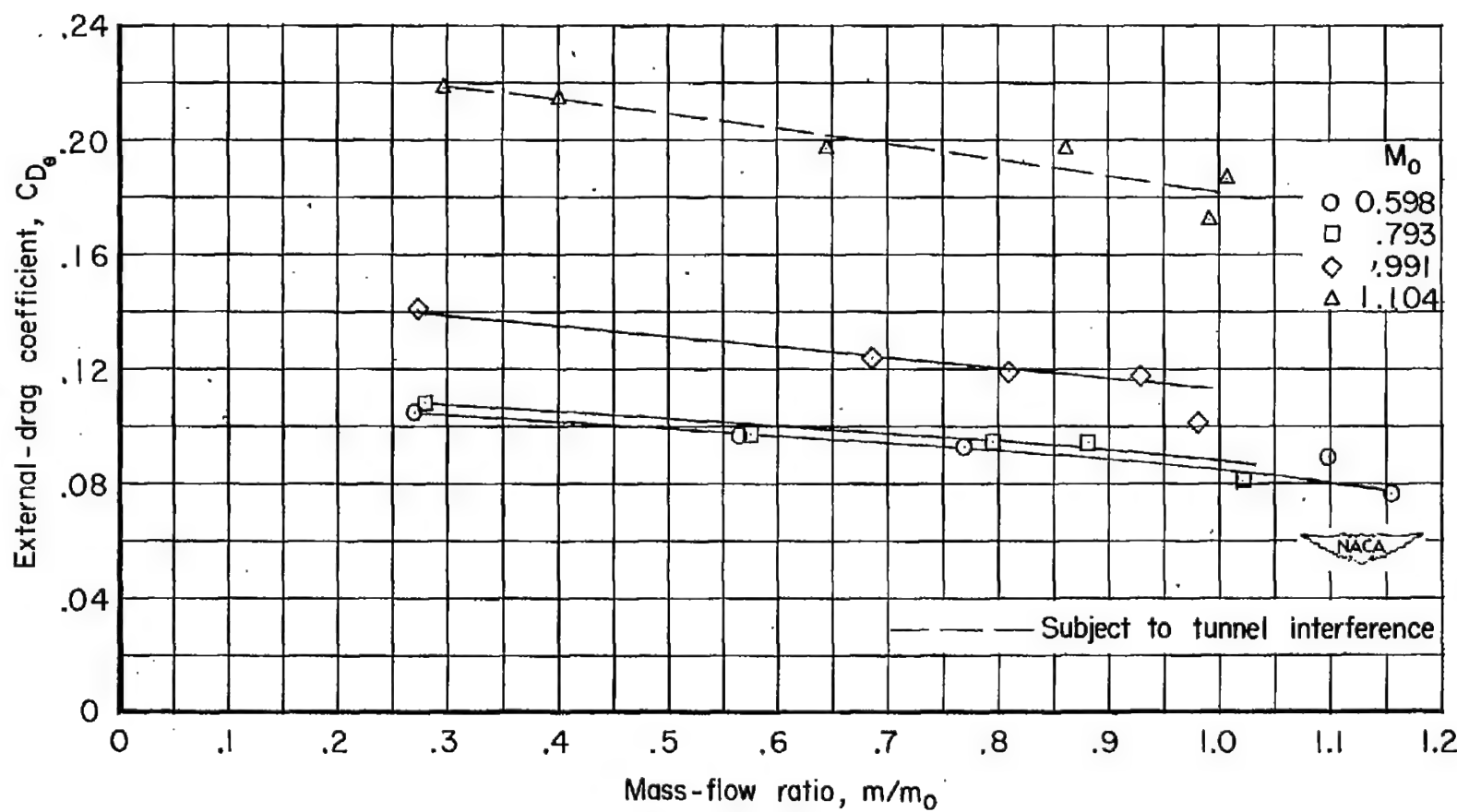


Figure 18.- Variation of external-drag coefficient with mass-flow ratio.
NACA 1-40-400 nose inlet; $\alpha = 0^\circ$.

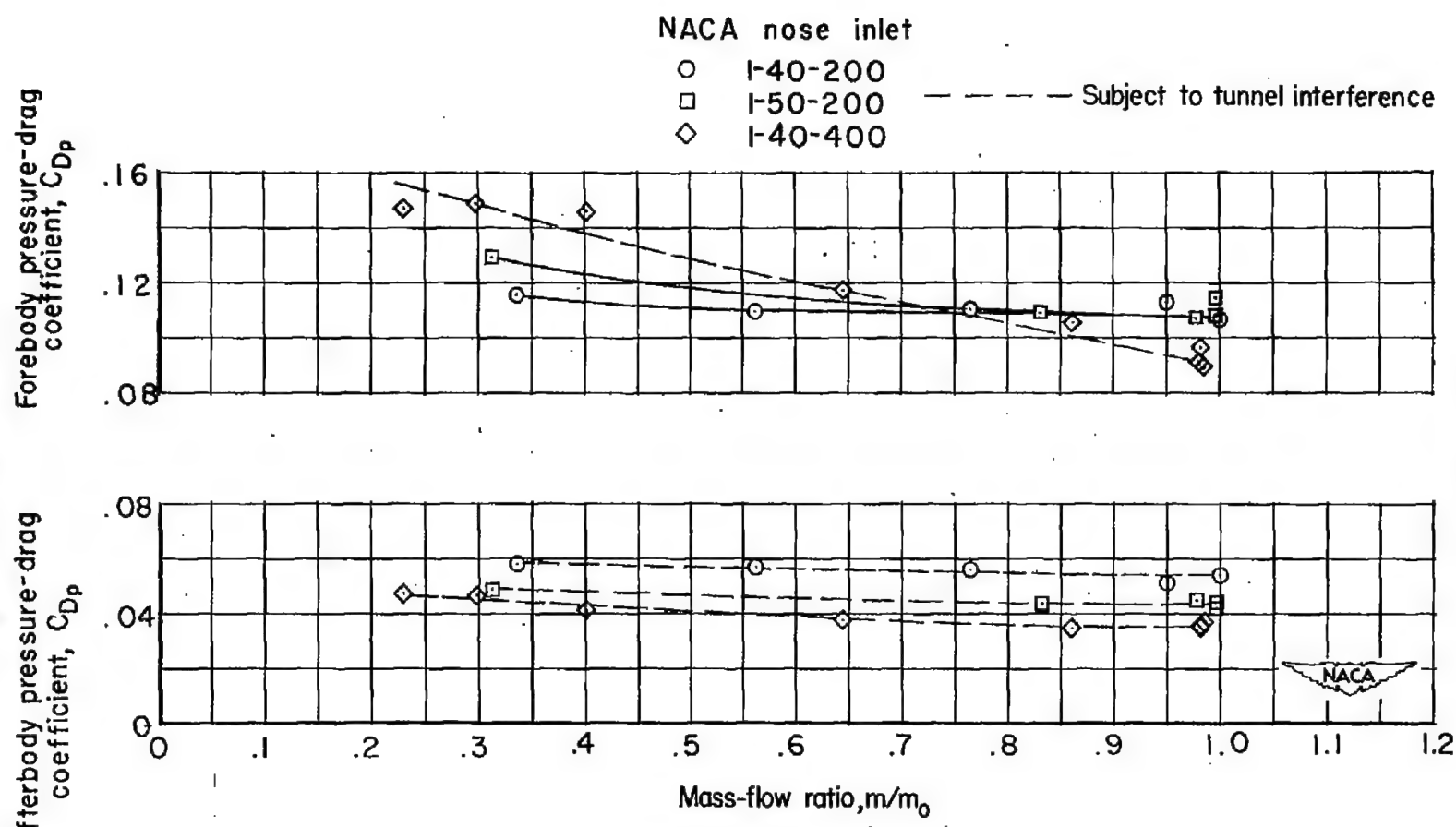


Figure 19.- Variation of forebody and afterbody pressure-drag coefficients with mass-flow ratio. $M_\infty \approx 1.11$; $\alpha = 0^\circ$.

NACA RM 152J23

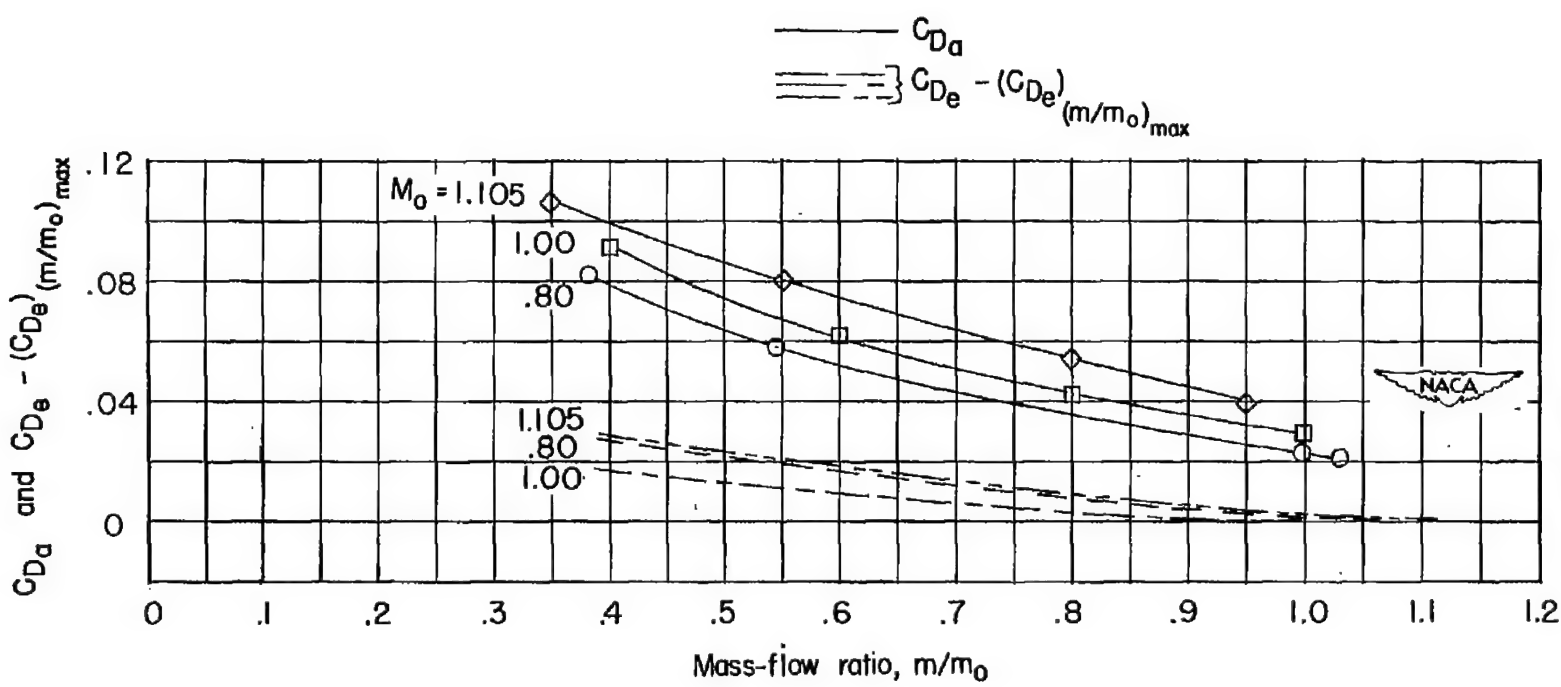


Figure 20.- Comparison of additive-drag coefficient and external-drag-coefficient increment. NACA 1-40-200 nose inlet. $\alpha = 0^\circ$.

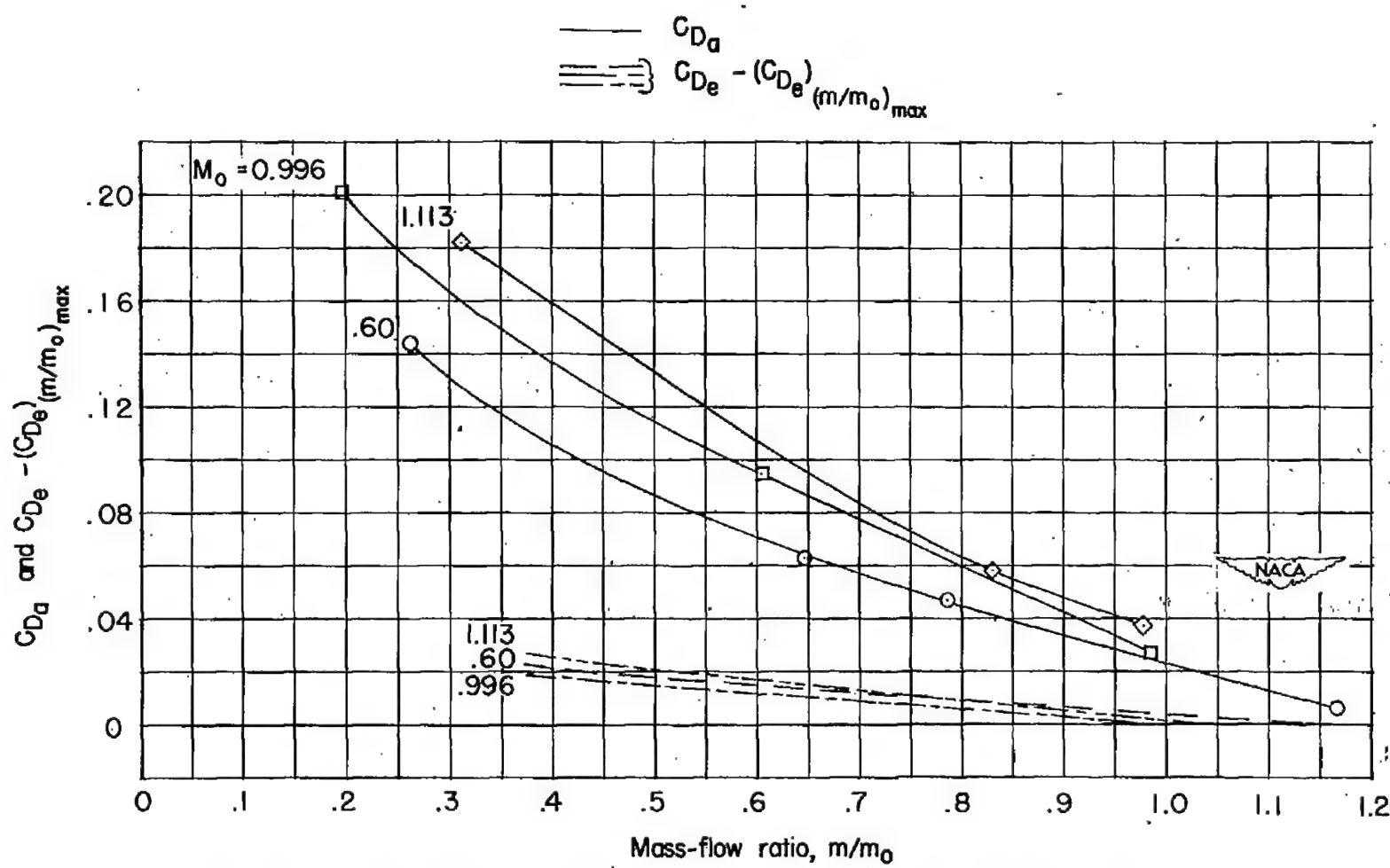


Figure 21.- Comparison of additive-drag coefficient and external-drag-coefficient increment. NACA 1-50-200 nose inlet. $\alpha = 0^\circ$.

NACA RM 152J23

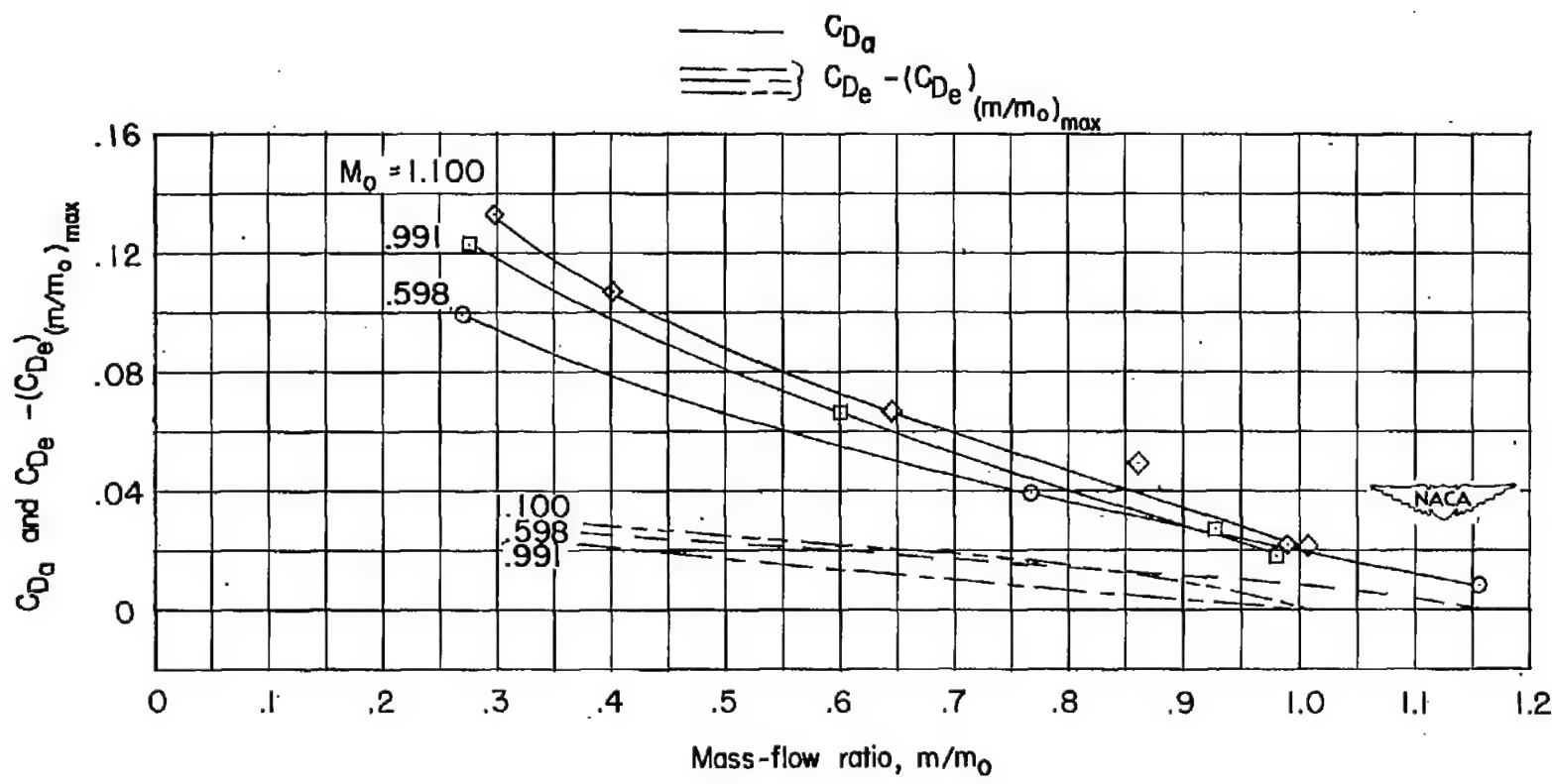


Figure 22.- Comparison of additive-drag coefficient and external-drag-coefficient increment. NACA 1-40-400 nose inlet. $\alpha = 0^\circ$.

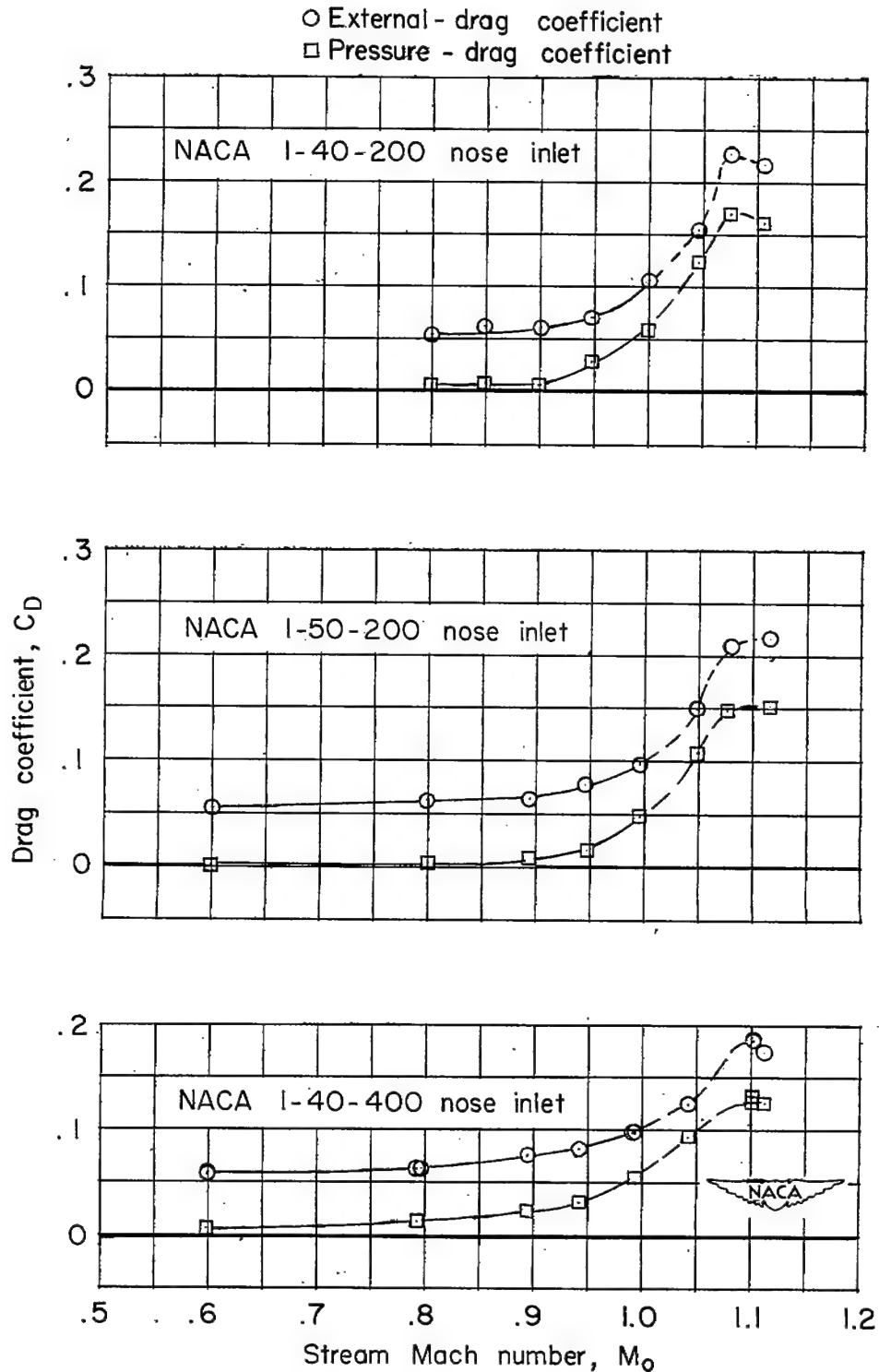


Figure 23.- Comparison of external-drag coefficient and pressure-drag coefficient. Inlet choked; $\alpha = 0^\circ$.

NACA RM 152123

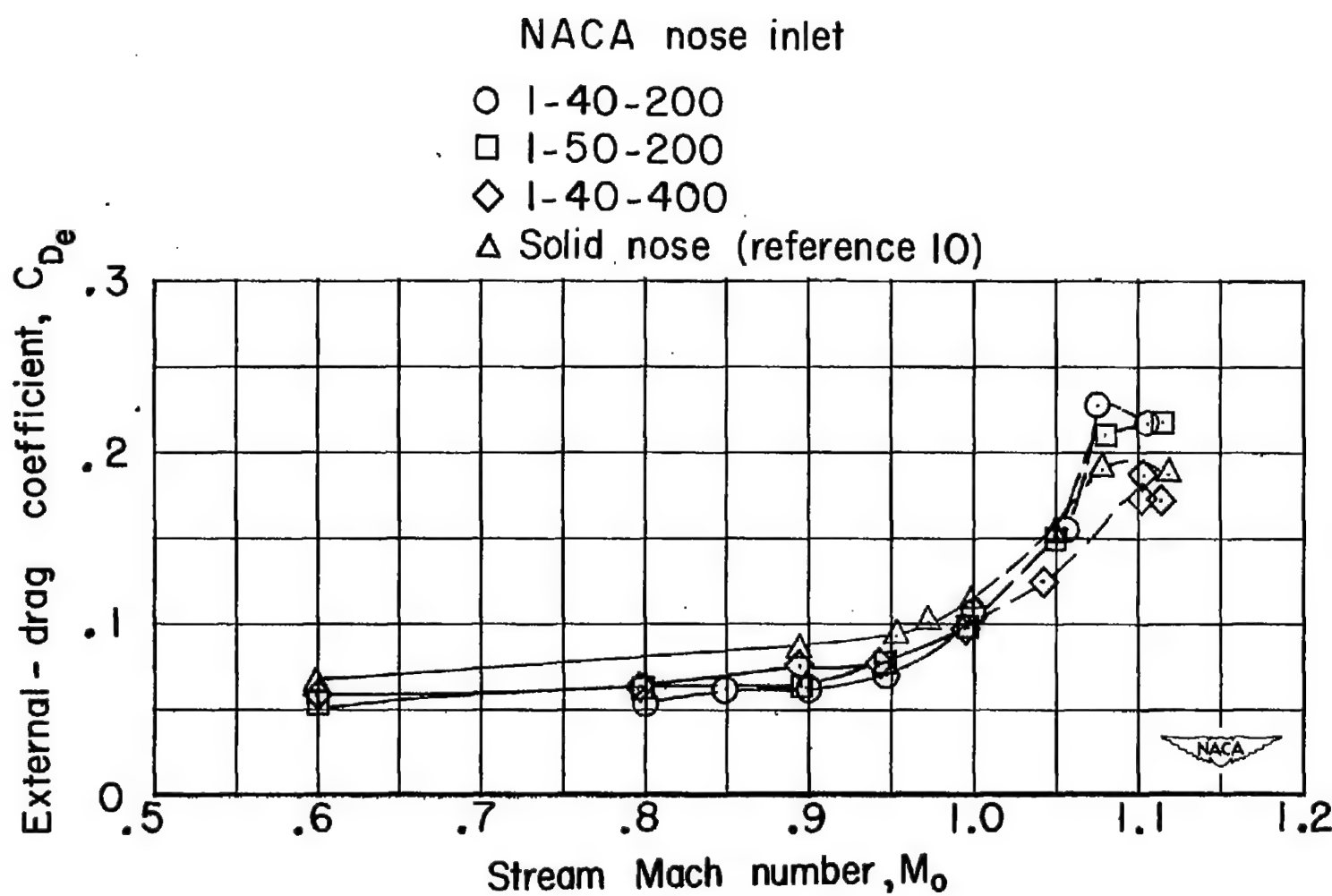


Figure 24.- Variation of external-drag coefficient with stream Mach number.
Inlet choked; $\alpha = 0^\circ$.

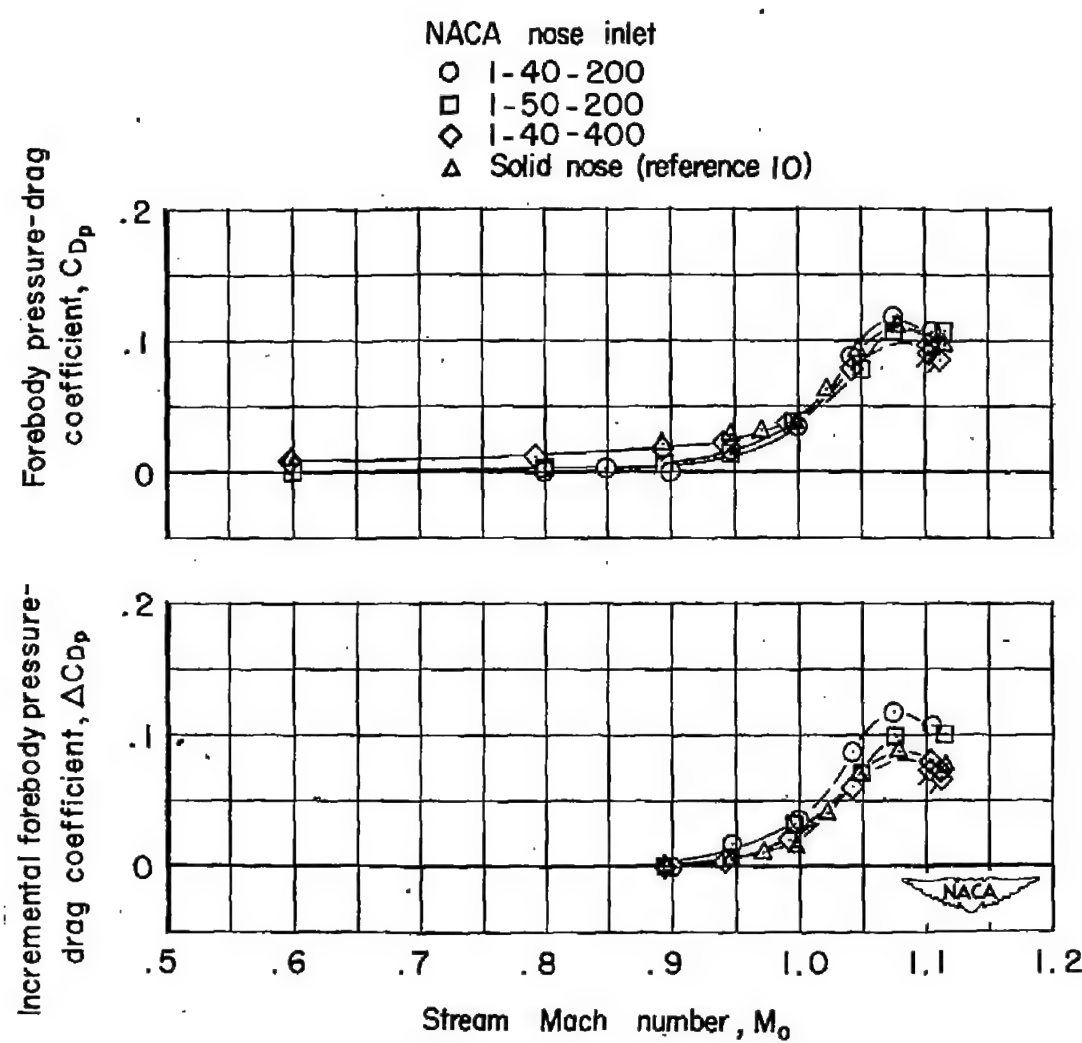


Figure 25.- Forebody pressure-drag comparison. Inlet choked; $\alpha = 0^\circ$.
(Flagged symbols corrected for tunnel interference.)

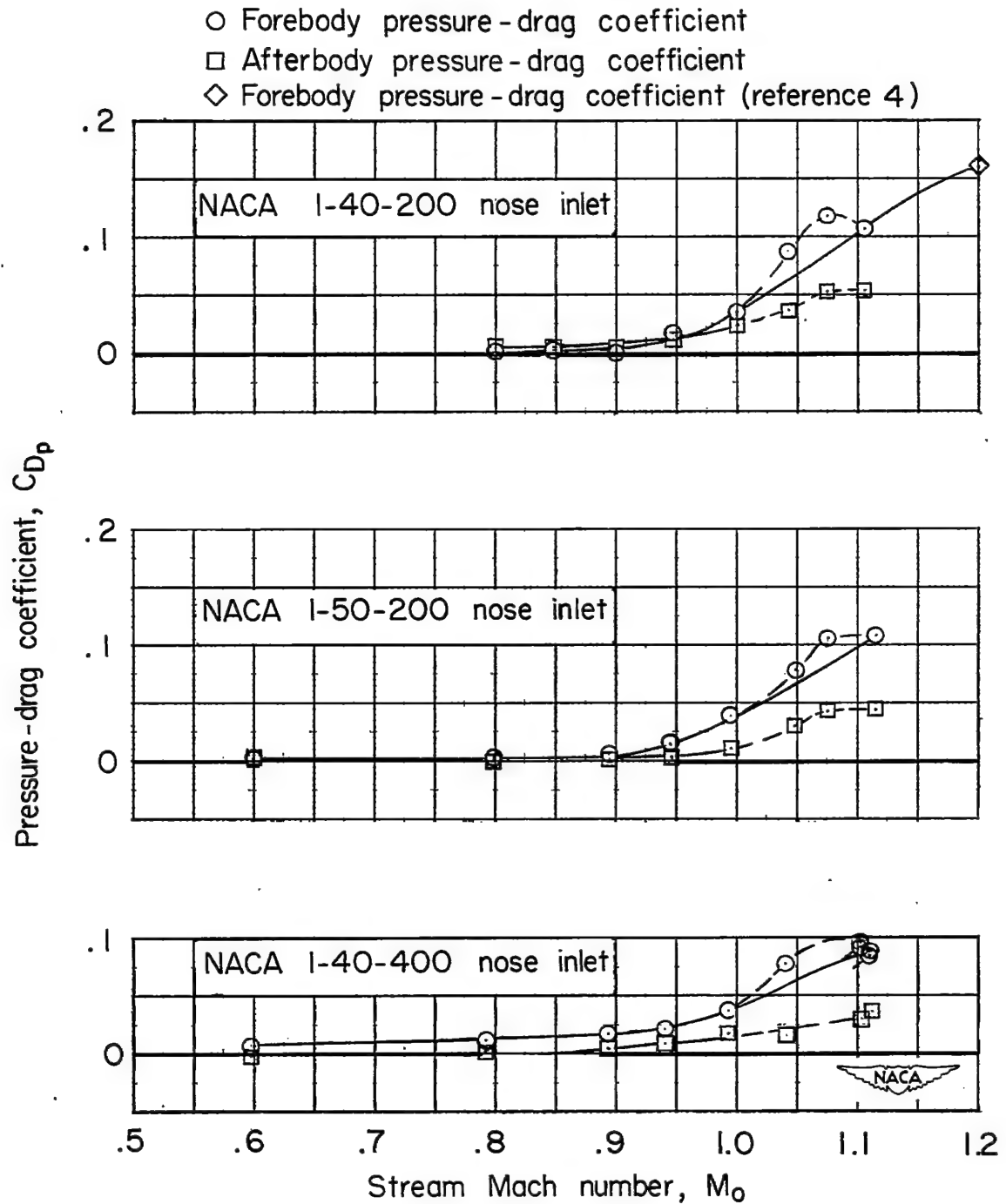
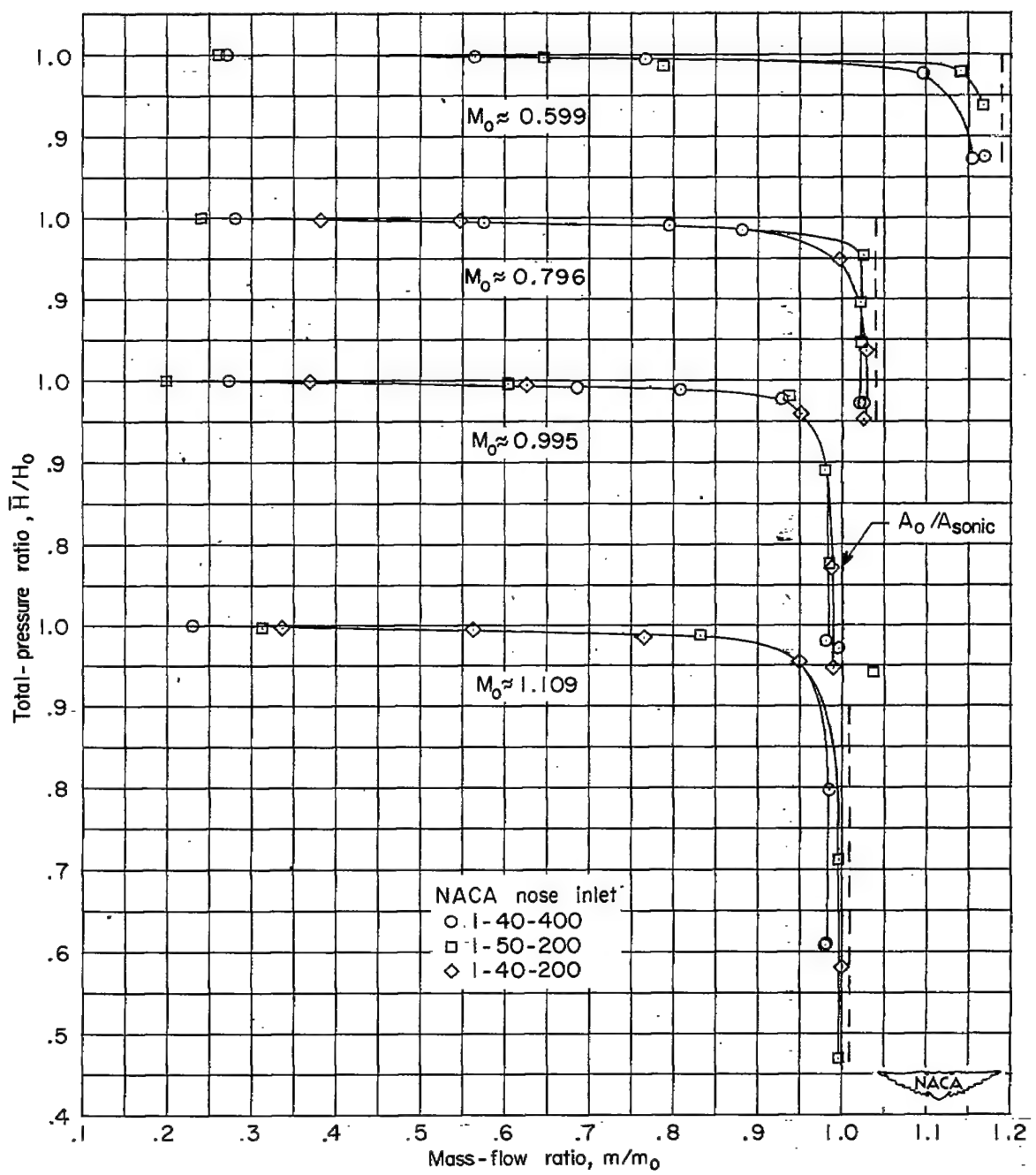


Figure 26.- Variation of forebody and afterbody pressure-drag coefficients with stream Mach number. Inlet choked; $\alpha = 0^\circ$. (Flagged symbols corrected for tunnel interference.)

Figure 27.- Variation of total-pressure ratio with mass-flow ratio. $\alpha = 0^\circ$.

NACA RM 152523

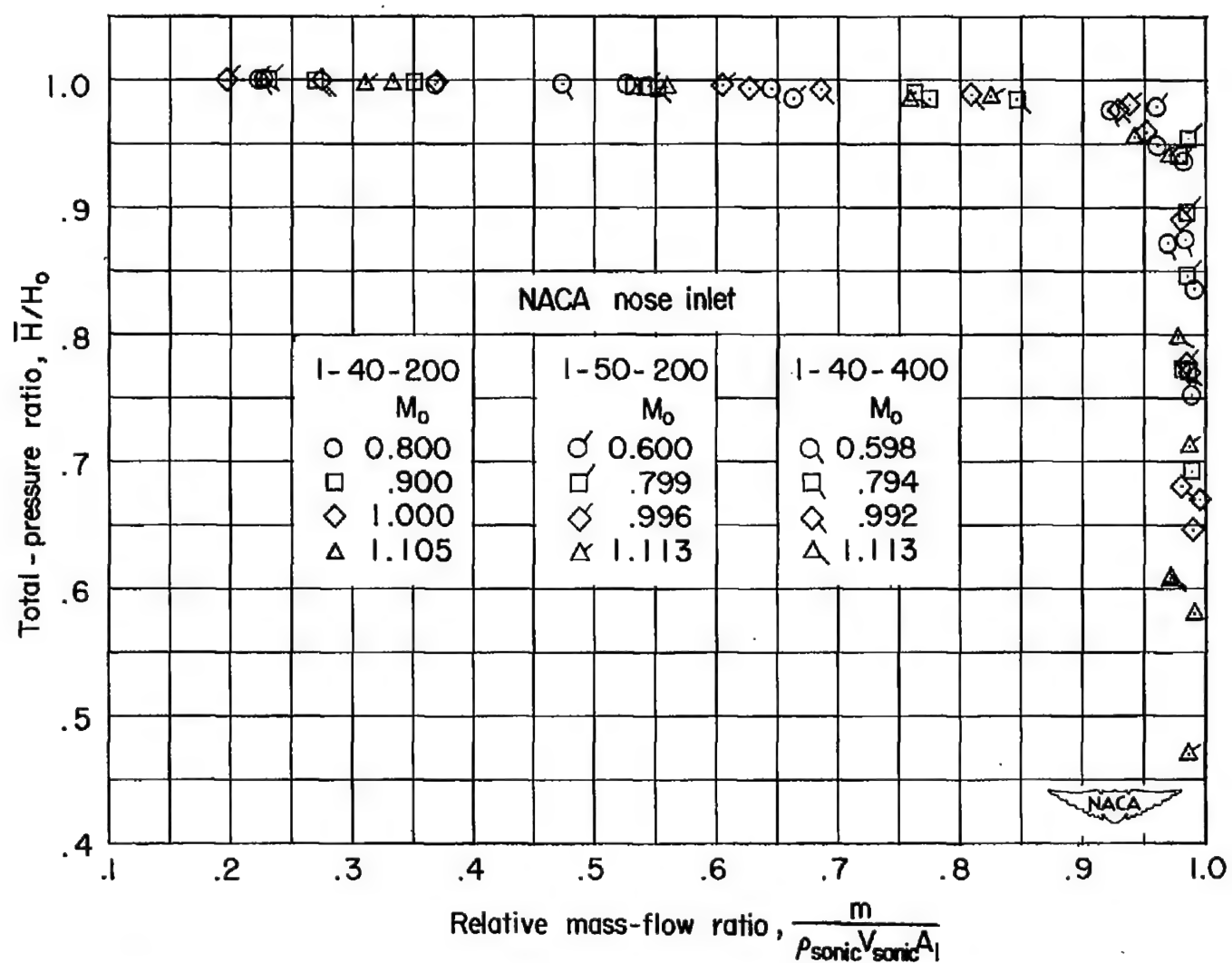


Figure 28.- Variation of total-pressure ratio with relative mass-flow ratio. $\alpha = 0^\circ$.

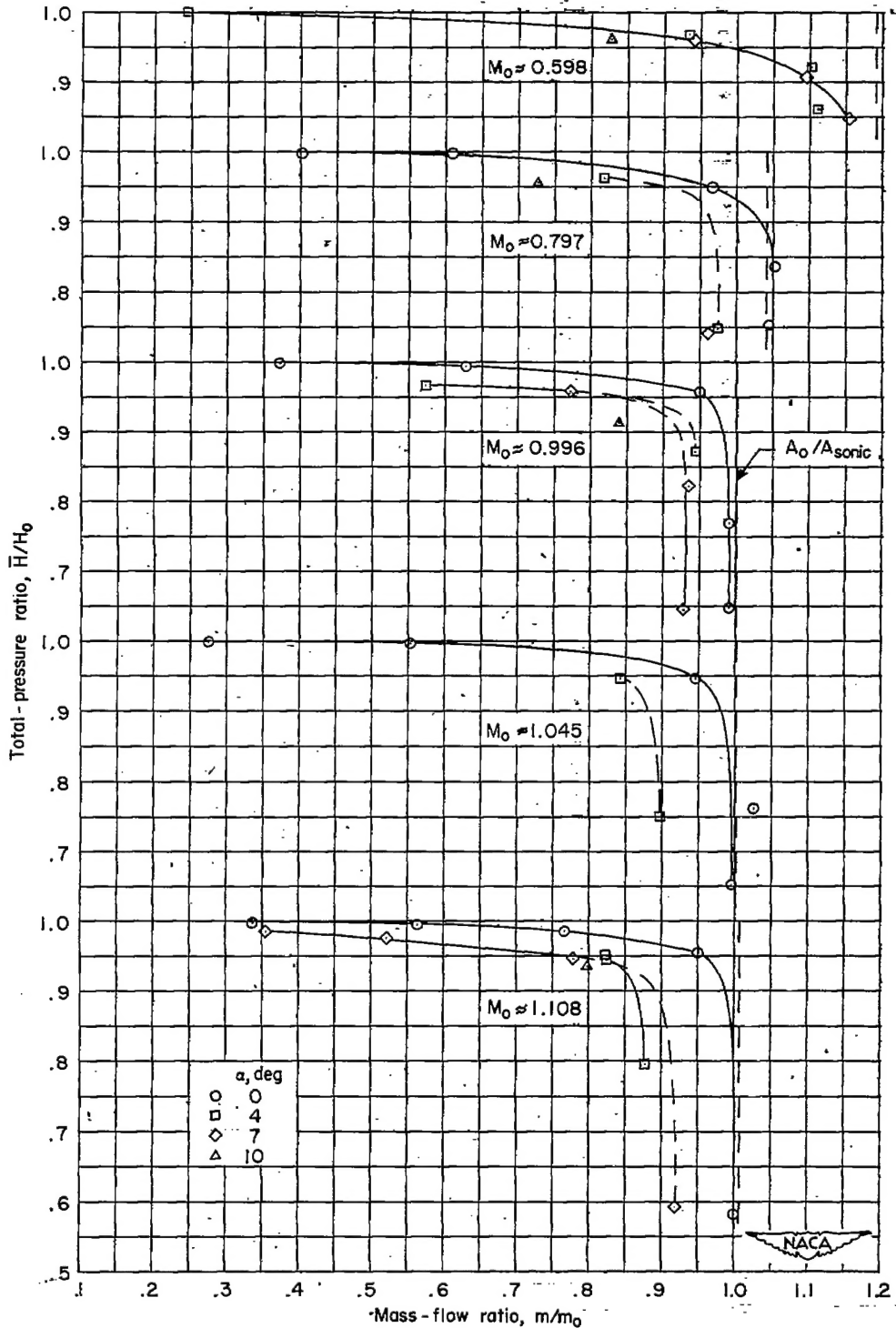


Figure 29.- Variation of total-pressure ratio with mass-flow ratio.
NACA 1-40-200 nose inlet.

NACA RM L52J23

69

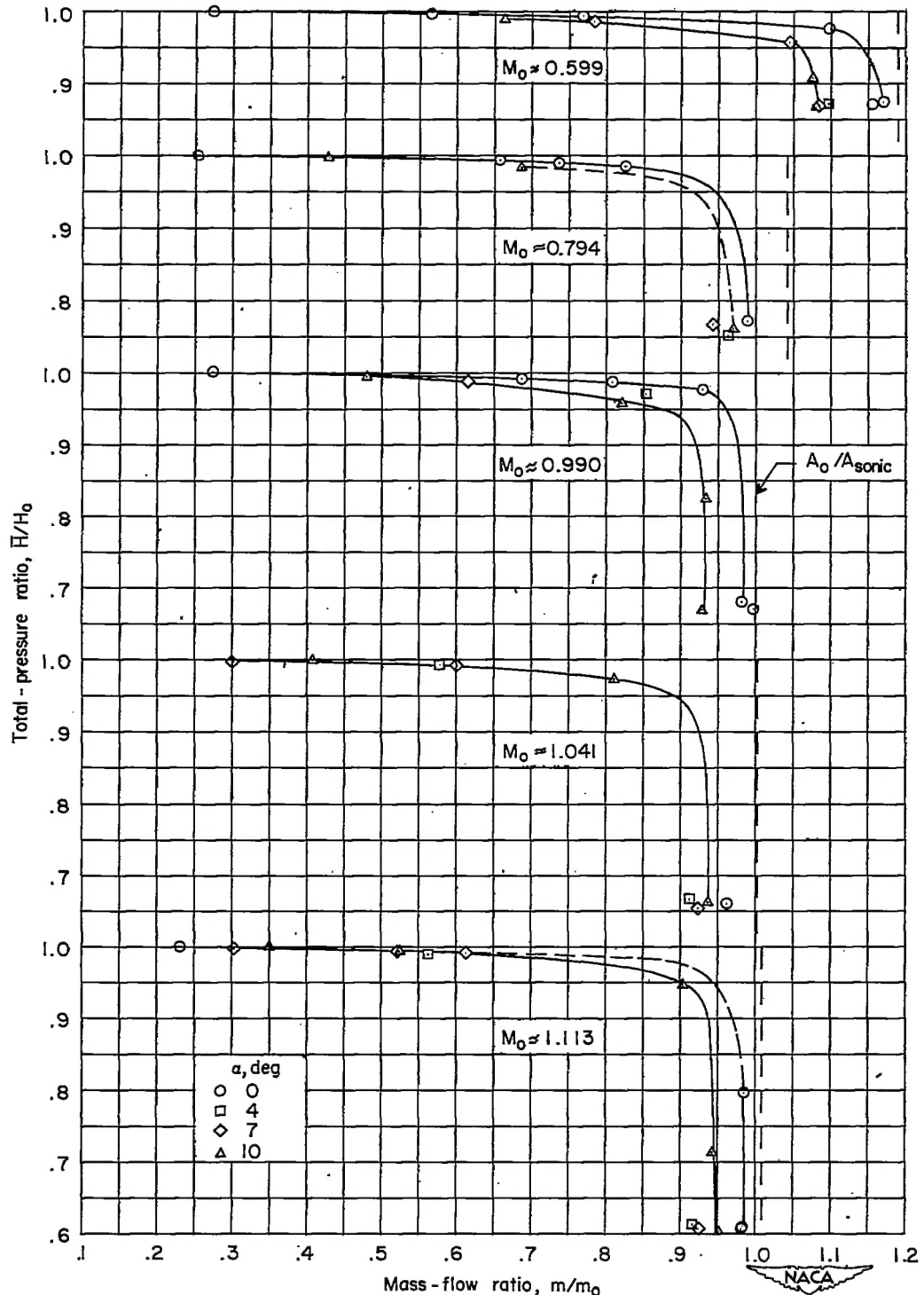


Figure 30.- Variation of total-pressure ratio with mass-flow ratio.
NACA 1-40-400 nose inlet.

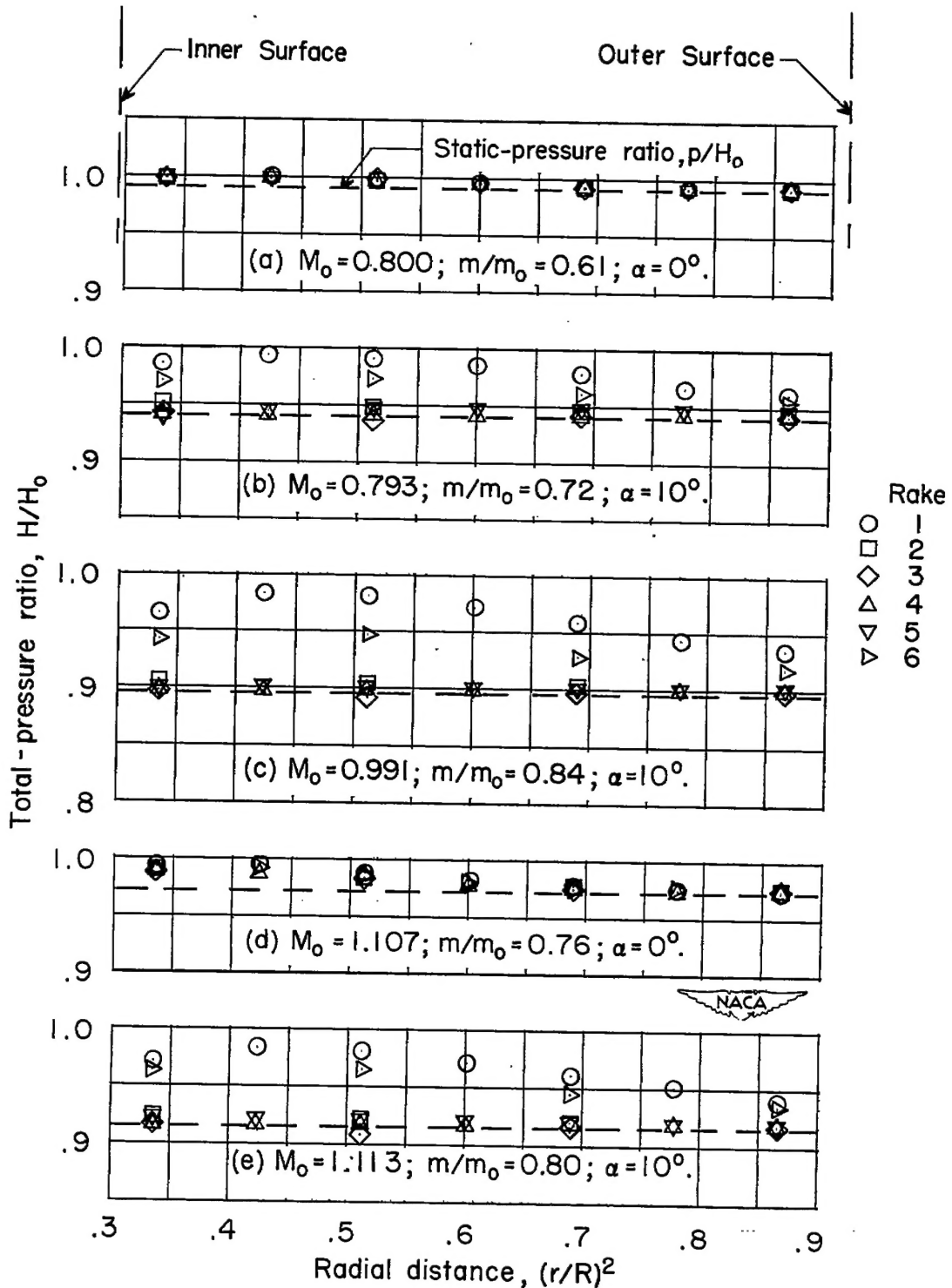


Figure 31.- Radial distribution of total-pressure ratio. NACA 1-40-200 nose inlet.

NACA RM 152J23

71

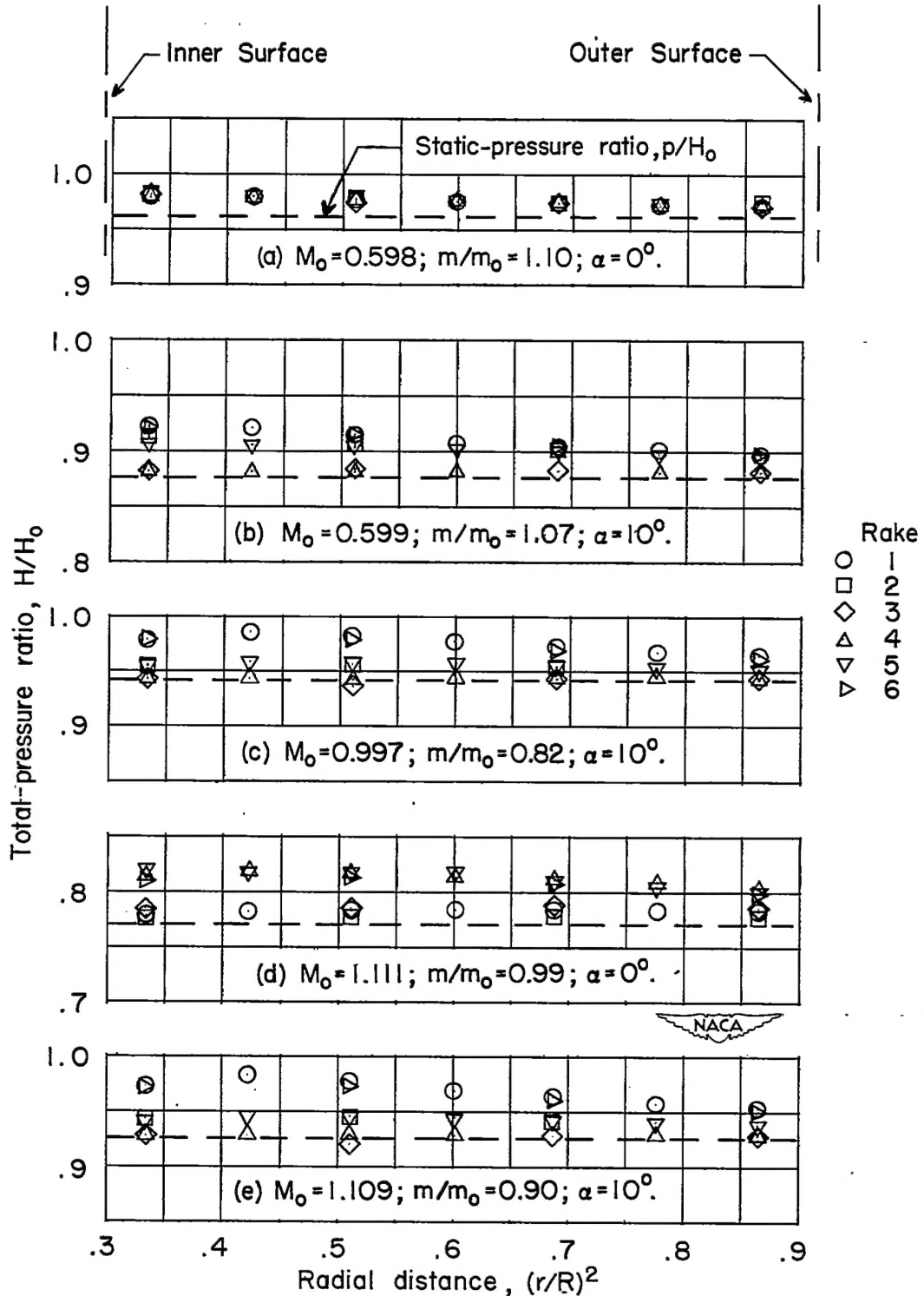


Figure 32.- Radial distribution of total-pressure ratio. NACA 1-40-400 nose inlet.